Nonlinear spectroscopy at the diffraction limit: probing ultrafast dynamics with shaped few-cycle laser pulses

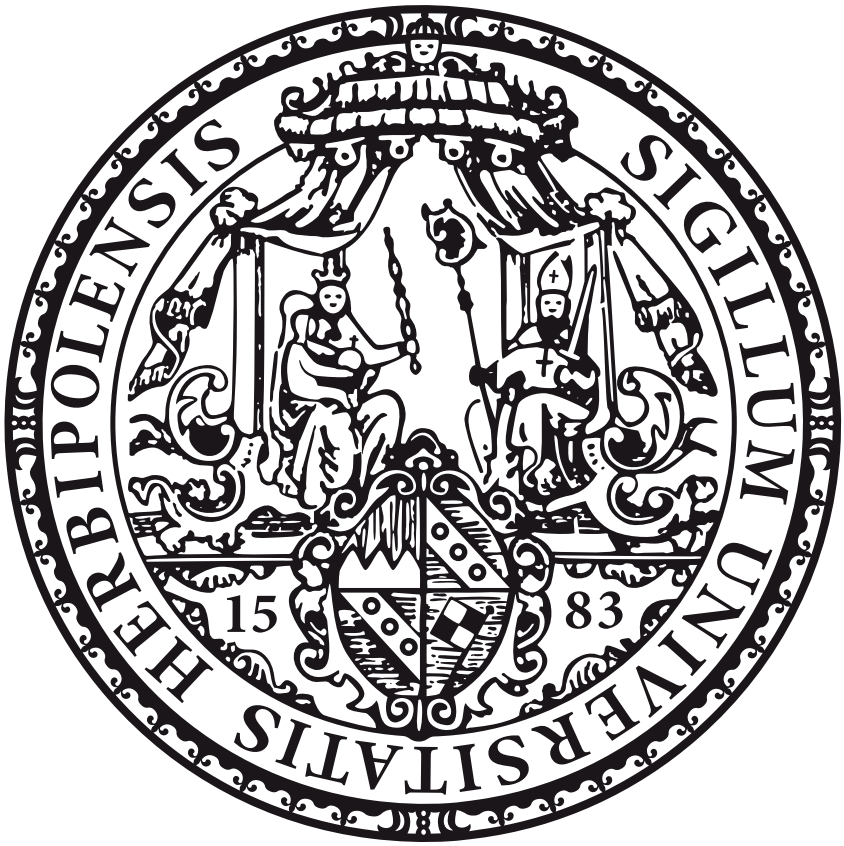

Dissertation zur Erlangung des naturwissenschaftlichen Doktorgrades der Julius-Maximilians-Universität Würzburg

vorgelegt von

Sebastian Reinhold Götz

aus Bayreuth

Würzburg 2018

Eingereicht am: _____
bei der Fakultät für Physik und Astronomie

1. Gutachter: Prof. Dr. T. Brixner
2. Gutachter: _____
3. Gutachter: _____
der Dissertation

Vorsitzende(r)_____

1. Prüfer: Prof. Dr. T. Brixner
2. Prüfer: _____
3. Prüfer: _____
des Promotionskolloquiums

Datum des Promotionskolloquiums: _____

Doktorurkunde ausgehändigt am _____

List of Publications

Parts of this thesis have been published in the following peer-reviewed journal articles:

[1] S. Goetz, D. Li, V. Kolb, J. Pflaum, and T. Brixner.
Coherent two-dimensional fluorescence micro-spectroscopy.
Opt. Express 26, 3915-3925 (2018).

[2] S. Goetz, G. Razinskas, E. Krauss, C. Dreher, M. Wurdack, P. Geisler, M. Pawłowska, B. Hecht, and T. Brixner.
Investigation of the nonlinear refractive index of single-crystalline thin gold films and plasmonic nanostructures.
Appl. Phys. B 122:94 (2016).

[3] M. Pawłowska, S. Goetz, C. Dreher, M. Wurdack, E. Krauss, G. Razinskas, P. Geisler, B. Hecht, and T. Brixner.
Shaping and spatiotemporal characterization of sub-10-fs pulses focused by a high-NA objective.
Opt. Express 22, 31496-31510 (2014).

Further publications not related to this thesis:

[4] C. Rewitz, G. Razinskas, P. Geisler, E. Krauss, S. Goetz, M. Pawłowska, B. Hecht, and T. Brixner.
Coherent Control of Plasmon Propagation in a Nanocircuit.
Phys. Rev. Applied. 1, 014007 (2014).

[5] P. Geisler, G. Razinskas, E. Krauss, X.-F. Wu, C. Rewitz, P. Tuchscherer, S. Goetz, C.-B. Huang, T. Brixner, and B. Hecht.
Multimode Plasmon Excitation and In Situ Analysis in Top-Down Fabricated Nanocircuits.
Phys. Rev. Lett. 111, 183901 (2013).

An overview of adapted passages and the corresponding page numbers can be found in the table below. The sources of adapted figures are additionally indicated at the end of the corresponding figure captions.

Publication		Use	Dissertation
[1][1]	pp. 3–4	text reproduced and modified	pp. 69–70
	pp. 4–6	figures adapted, text reproduced and modified	pp. 70–72
	pp. 6–8	figures adapted, text reproduced and modified	pp. 72–75
	pp. 8–11	figures adapted, text reproduced and modified	pp. 76–79
[2][2]	pp. 1–2	text reproduced and modified	pp. 57–57
	pp. 2–4	figures adapted, text reproduced and modified	pp. 58–61
	pp. 4–5	figures adapted, text reproduced and modified	pp. 61–63
	pp. 5–7	figures adapted, text reproduced and modified	pp. 63–65
	pp. 7–9	figures adapted, text reproduced and modified	pp. 65–68
[3][3]	pp. 4–6	figure adapted, new text	pp. 8–9
	pp. 6–8	figure adapted, new text	pp. 23–30
	pp. 8–15	figures adapted, new text	pp. 30–40

[1]Reproduced and adapted with permission from Optics Express **26**, 3915 (2018).

[2]Reproduced and adapted with permission from Applied Physics B **122**, 94 (2016).

[3]Reproduced and adapted with permission from Optics Express **22**, 31496 (2014).

Contents

1 Introduction

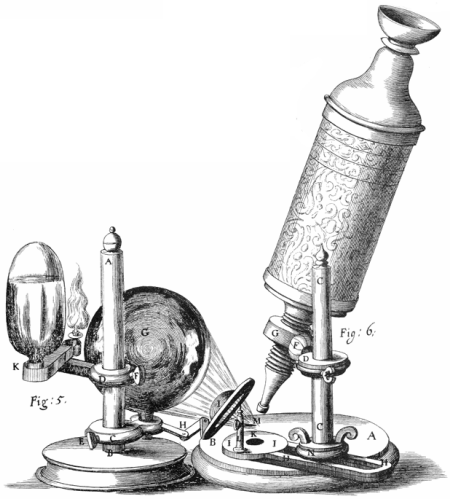

Figure 1.1 | Hooks' microscope [6]. Illustration under public domain

How can the inner workings of microscopic systems be unraveled? In general, simply by careful observation. Curiosity drives our desire to learn more about our surroundings every day. Beyond the world of objects familiar to us through direct observation lie vast spaces of the unknown. Some people dedicate their life to investigate the night sky and extend their knowledge about the birth of vast galaxies billions of years ago and billions of light-years away. In contrast, the question asked here lies at the other end of the scales: the observation of objects too small and changing too fast to be observed by the bare eye, which triggered a quest to enhance human vision. Dating back to $721 - 705$ B.C., a plano-convex piece of rock crystal was believed to be a magnifying lens of sorts [7].

The development of what is called a microscope today picked up pace at the end of the 16th century in Holland, when Hans Jensen developed a compound microscope consisting of two lenses, in the era when Galileo and Kepler studied the movements of celestial objects with newly developed telescopes. One of the earliest books about microscopy, "Micrographia" [6], was published by Robert Hooke of the Royal Society of London in 1665. In his book, he describes the used apparatus (seen in Fig. 1.1) along with drawings of his observations, e.g., of plants and insects.

At the same time, other microscope designs were developed on continental Europe, e.g., by the Italians Giuseppe Campani and Eustachio Divini and by Antony van Leeuwenhoek [7, 8]. The latter, a Dutch draper, built single lens microscopes with an impressive resolution reaching 1.4 μm, allowing for observation of bacteria.

Christiaan Huygens postulated the wave theory of light in the same century, a principle that should not stay without consequences for microscopy. And so it was Ernst Abbe

who put an end to the euphoria of an arbitrary improvement of the spatial resolution. He discovered that the waves of light cannot be ultimately confined, but instead only resolve a spatial scale greater than roughly half of their wavelength [9]. Approaching this diffraction limit is therefore the goal when maximizing spatial resolution, as shall be done in the work presented in this thesis.

Besides the challenge of improving the spatial resolution, the initial question was raising the desire to push towards a second limit: to observe processes with the highest possible temporal resolution. Eadweard Muybridge was asked to investigate a process too fast to be observed directly by the human eye. When confronted with the question whether or not the four legs of a galloping horse were ever completely off the ground in 1878, he could affirm the question by taking a series of 24 photographs shot in quick succession.

The temporal resolution of such an experiment depends on the origin of the process gating the observation, i.e., the exposure. For mechanical shutters, it is the inertia of the moving parts. For electrical shutters, it is the modulation frequency of the electric currents. If an observation is gated by light, the limitation is the duration of the flash. When conducting experiments to investigate chemical reactions, Porter and Coworkers used flash discharge tubes to create bursts of lights short enough to allow for a temporal resolution of 50 μs. By using a pair of flashes with variable time delay, the temporal evolution of chemical reactions could be mapped by the second pulse after the initial excitation. The technique is known as flash photolysis [10], but the method of scanning a pair of delayed light pulses evolved into the so-called pump-probe spectroscopy.

With the advent of lasers [11], new sources of intense, coherent light became available in the 1960s [12]. Two-photon absorption, which was theoretically described already in 1931 [13], could now be experimentally demonstrated [14]. By the coherent superposition of broadband laser spectra, light bursts lasting merely a single oscillation of the electromagnetic field are in reach, representing only a few femtoseconds in the visible region. With the help of such ultrashort laser pulses available since the 1980s, e.g., dye lasers [15] and Ti:Sapphire oscillators [16], researchers around the world have started to investigate molecular motions in real time. This endeavor was further facilitated by the advent of laser pulse-shaping technology [17, 18]. Ahmed H. Zewail was awarded the Nobel Prize in 1999 for developing the field of laser femtochemistry [19, 20].

Nonlinear microscopy [21] brings femtosecond spectroscopy to a sub-micron scale, facilitating the concept of confocal microscopy to further reduce the probed sample volume [22]. Molecular dynamics are observed by nonlinear spectroscopy over wide spectral ranges in the gas, liquid, and solid phase. In the solid phase, great efforts are taken to improve the spatial resolution in addition to the temporal resolution to reduce the observed volume from macroscopic samples to microscopic scales, down to the limit of single molecules. On the nanoscale, photonic and plasmonic structures can be designed and experimentally tested. Metamaterials introduce surfaces with tailored optical properties that previously were thought to be impossible [23].

To investigate such phenomena, sophisticated apparatuses are developed that simultaneously allow for optical analysis approaching the physical limits on the length and timescale. The work presented in this thesis aims to combine these two worlds, using ultrafast laser pulses to investigate microscopic systems at the diffraction limit. After a brief introduction of recent developments towards this aim, the concept of the ex-

perimental setup is presented in Chapter 2. The used light source, optical components and detectors are reviewed. A description of methods for achieving and characterizing spatial and temporal confinement follows. The phase- and amplitude calibration process for the used LCD-based pulse shaper is presented prior to an evaluation of potentially occurring artifacts. Corrections of these artifacts are proposed and executed, as they reduce deviations between actual and desired pulse shapes.

After the description of the experimental setup in Chapter 2, its capabilities are demonstrated by two applications in Chapter 3 and Chapter 4. The successful design of functional nanostructures largely depends on the precise knowledge of the material's properties. Therefore, Chapter 3 aims at the determination of the nonlinear refractive index of gold, a metal widely used for plasmonic nanostructures. Two methods are described, the z-scan and phase change between two eigenmodes in a plasmonic nano-interferometer, supported by FDTD simulations.

As a second application, the novel method of coherent two-dimensional (2D) fluorescence micro-spectroscopy is presented. It allows for determination of ultrafast dynamics on surfaces and their lateral variation with diffraction-limited spatial resolution. The method is demonstrated on heterogeneous thin-films of fluorinated zinc phthalocyanine. The achieved results are summarized together with an outlook on further developments and applications in Chapter 5.

2 An experimental setup for ultrafast spectroscopy

2.1 Developments in ultrafast microscopy

As described in the previous chapter, nonlinear spectroscopy was established in laboratories with the advent of powerful light sources. The achievable peak powers were increasing steadily after the invention of the laser by the introduction of pulsed emission, e.g., by Q-switching [24] and mode locking [25]. Even higher powers were delivered by femtosecond laser pulses, by pulsed dye lasers [15] popular in the 1980s. They were gradually replaced by the more convenient Ti:Sapphire lasers in the following decades [16, 26–29]. In combination with confocal microscopes [22], the potent light sources allowed for nonlinear microscopy [21]. Probing of highly confined sample volumes was made possible by facilitation of a variety of processes, including two-photon absorption [21], third harmonic generation [30], and coherent anti-Stokes Raman scattering [31, 32]. Fluorescence-emission-based microscopy facilitated by nonlinear excitation has become a wide-spread tool, especially for investigation of biological systems, e.g., for in vivo studies of neuronal activity with two-photon excited fluorescence microscopy [33–36].

To access temporal information from systems with microscopic spatial resolution, spectroscopy methods like pump-probe spectroscopy [10, 19, 20, 37] or multi-dimensional spectroscopy [38–43] had to be adapted to be available at small spatial and temporal scales at optical wavelengths. When using short focusing distances, i.e., with microscope objectives, a collinear geometry becomes more practical than other approaches [44, 45]. A temporally separated phase-stable pulse train is essential, e.g., for observation of wavepacket dynamics [20, 46, 47] and coherent control [48–51]. It can be generated by stabilized interferometric geometries and alternatively by pulse shapers. The latter were commonly used for femtosecond spectroscopy [17, 18, 52–54], microscopy [54–57], and two-dimensional spectroscopy [58–61]. Pump-probe microscopy [62], when brought to the femtosecond timescale [63], also benefited from the use of pulse shaping [64]. The simultaneously observed number of chromophores was reduced down to the limit of single-molecule spectroscopy [65–68], with time-resolved experiments at ambient temperatures realized just in the last decade [69–73].

A combination of microscopy and two-dimensional spectroscopy was demonstrated in the IR [74–77], but has not been extended to the near infrared and the visible spectral range yet. The implementation of two-dimensional microscopy including the visible range demands a highly optimized experimental setup. The following section defines the requirements that have to be met to implement ultrafast nonlinear spectroscopy at the diffraction limit in addition to further functionality, e.g., spatial selectivity of excitation and emission needed for the investigation of near-field propagation.

2.2 Building blocks of a laboratory for ultrafast microscopy

As described in Section 2.1, the ascent of lasers as a coherent light source of high brilliance opened the door towards new applications in manufacturing, sensing and spectroscopy. With generation of few-cycle or even single-cycle optical fields, it became possible to probe dynamics with femtosecond resolution. While it has been shown that this temporal precision can be paired with sub-micron spatial resolution, it requires careful consideration in the design of the experimental setup. Optical pulses need to be precisely controlled from the light source along the propagation over reflecting and through transmitting optics before they are delivered to and collected from the sample towards specialized detectors.

The components of the experimental setup used for the work presented in this thesis were adapted to meet the requirements for the desired functionality, which is the investigation of surfaces with spatial resolution at the diffraction limit with few-cycle femtosecond laser pulses. The experimental setup, shown in an overview in Fig. 2.1, allows for three-dimensional mapping of the spatial sample structure and collection of incoherent as well as coherent signals with spatial selectivity. In addition to signals from the excited sample volume, this includes the collection of light emitted from the vicinity of the excitation position, e.g., as a result of propagation or diffusion. To achieve femtosecond temporal resolution, the sample can be excited with carefully prepared laser pulses or laser-pulse trains. In addition, the temporal structure of coherent emissions from the sample can be retrieved by interferometric characterization.

Since complex measurement sequences and the reproducibility of results depend on long-term stability against mechanical fluctuations and drifts, the latter have to be suppressed. The temperature, the humidity and the air flow in the vicinity of the experiment are regulated and mechanical vibrations are damped. All optical components have to be carefully selected to feature a low temperature coefficient and supreme surface flatness besides their primary functionality. Thereby, phase stability from the light source to the sample is ensured and pulse front distortions are avoided. The spectral and temporal shape of the laser pulses is controlled by a spatial light modulator to allow for temporal laser pulse compression and characterization. In addition, complex pulse shapes can be generated, e.g., spectral amplitude filters or temporally delayed pulse trains.

An optical microscope facilitates spatial confinement of the exciting fields, confocal detection allows for spatial selectivity of the emission. The microscope objective consists of a complex system of lenses to allow for high spatial confinement of the light while avoiding aberrations due to the high spectral bandwidth. Preserving the desired pulse shape in the focus is far from trivial. Sophisticated procedures for spatial and temporal optimization of the laser focus are therefore carried out. Sensitive detection is crucial for minimizing light-induced degradation of the sample. Apart from using an objective with high numerical aperture, detectors with high quantum yield capable of counting single photons are used to counteract this degradation. In addition, spectrally resolved detection is facilitated by a low-noise spectrometer. The experimental setup used in this work is subject to an iterative development process, since all components have to

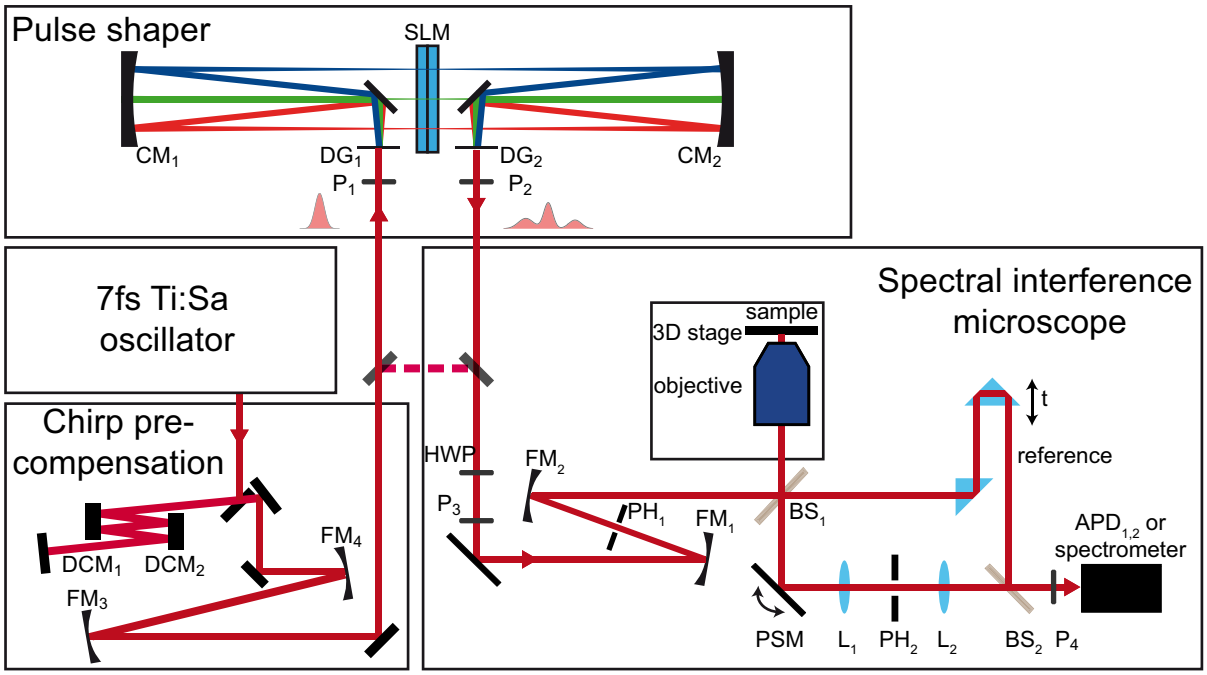

Figure 2.1 | Experimental setup used for the majority of the experiments presented in this work. The laser pulses emitted from the oscillator are chirp-pre-compensated by a pair of double-chirped mirrors ($DCM_{1,2}$) and the pulse shaper. In the pulse shaper, spatial separation of the spectral components and focusing onto the spatial light modulator (SLM) is facilitated by diffraction gratings ($DG_{1,2}$) and cylindrical mirrors ($CM_{1,2}$). Adaption of the beam diameter with telescopes consisting of spherical focusing mirrors is done in front of the microscope ($FM_{1,2}$) and the pulse shaper ($FM_{3,4}$). The sample is mounted onto a 3D translation stage to position it relative to the focus of a NA = 1.4 immersion-oil microscope objective. The light from the sample plane is collected by the same objective and a single diffraction-limited area selected by confocal detection. The latter consists of a piezo scanning mirror (PSM) in combination with a lens-based telescope ($L_{1,2}$) having a pinhole (PH_2) in the image plane. The light is then detected either by a spectrometer or an avalanche photodiode (APD). In addition, a reference path bypassing the objective is realized by splitting from and recombining with light from the signal path through beamsplitters ($BS_{1,2}$). Linear polarizers (P_{1-4}) are used to conserve the polarization state along the beam path as well as for amplitude pulse shaping (P_2) and emission polarization selection (P_4). Variable attenuation is achieved by a half-waveplate (HWP) in combination with P_3. Figure adapted and modified from Ref. [3].

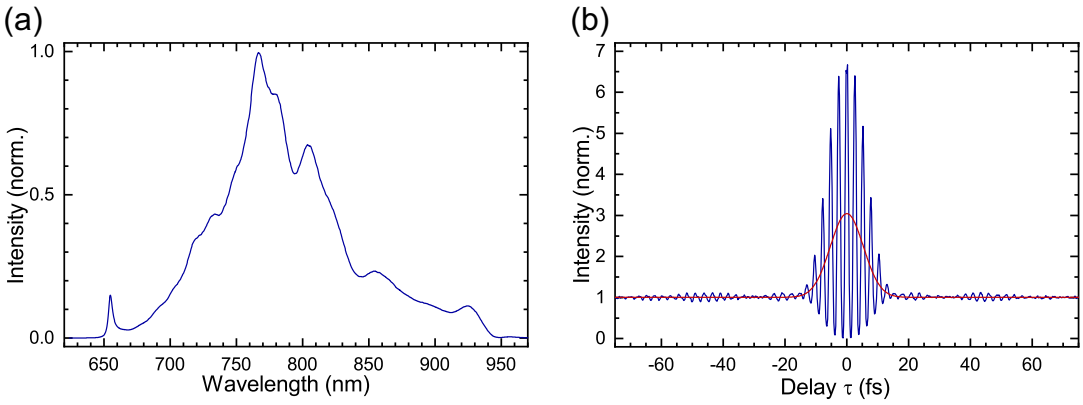

Figure 2.2 | (a) The normalized spectrum of the Ti:Sapphire oscillator used in this work, with a spectral range of 300 nm. (b) Pulse-shaper-assisted interferometric collinear quadratic autocorrelation of a compressed laser pulse normalized to the background level (blue curve). By Fourier filtering the non-oscillating component was obtained (red curve). The pulse duration was derived to be 9.1 fs from a Gaussian fit to the filtered curve.

be reevaluated if one of them is replaced. The development therefore includes tools for evaluating the functionality of individual components as well as their interplay. Monitoring the functionality and the stability during the actual measurements is crucial for validating the obtained results. Building a powerful experimental setup which is complex enough to fulfill all requirements, but simple enough to be reliable and controllable, is a balancing act that is described in the remainder of this chapter.

2.3 The laser source

Optically pumped Ti:Sapphire oscillators have proven to be a reliable source for femtosecond laser pulses in the last decades. To allow for pulsed operation, in contrast to continuous wave operation, dispersion that is picked up by the light in one round-trip inside the oscillator by transmission through the crystal, other dispersive media and the air has to be compensated. Early designs rely on geometrical path differences introduced through a prism compressor. As described below in Section 2.9, they mainly compress second order spectral dispersion. With the advent of chirped mirrors, higher order of the spectral dispersion can now also be compensated by mirror designs specific for the dispersive components used. Therefore, the dispersion compensation can be achieved over a much broader spectral range. Ti:Sapphire Oscillators with bandwidths spanning over a full octave have become commercially available, capable of creating laser pulses down to 4 fs, consisting of little more than a single oscillation of the electro-magnetic field.

In this work, spectral bandwidths of around 50 nm full width at half maximum (FWHM) and pulse lengths on the order of 30 fs (FWHM) were achieved with a home-built oscillator [78–80]. A prism compressor was used to compensate the second order of the spectral phase. When upgraded to an oscillator with reflective optics solely consisting of dielectric components (Pulse One PE, VENTEON Laser Technologies GmbH) in combination with chirped mirror pulse compression up to the fourth order, the capa-

bilities both in the spectral as well as in the time domain were significantly increased. As can be seen from a typical spectrum plotted in Fig. 2.2(a), it is capable of emitting light reaching from 650 nm to 950 nm wavelength, with a mode-locked output power of 560 mW at 80 MHz repetition rate. Using a pulse shaper to create a pair of temporally delayed collinear pulse copies and scanning the delay τ, a quadratic autocorrelation was measured that can be seen as the blue curve in Fig. 2.2(b) detected by a two-photon photodiode (TPPD). By Fourier transformation, the non-oscillating part of the trace can be separated from the oscillating contributions in the spectral domain. The non-oscillating component [red curve in Fig. 2.2(b)] is back-transformed and a Gaussian fit is applied. Thereby, a pulse duration of 9.1 fs is derived.

The high spectral bandwidth ranging from the visible (Vis) to the near-infrared (NIR) region covers plasmonic resonances of silver and gold and facilitates broadband excitation of chromophore systems, as will be demonstrated in the following chapters. Before that, the remaining components of the experimental setup used in this work are presented, along with a general review of alternative components.

2.4 Optics

Delivering sub-10 fs pulses even though a microscopy objective lens is used and remaining in control of the spatial and temporal pulse shape is a challenge that involves careful consideration over all the optics involved. For all transmissive optics, the substrate should be chosen to be as thin as possible to avoid unnecessary dispersion while maintaining sufficient flatness, preferably $\lambda/10$. In addition, one has to keep in mind that pulse copies created from multiple reflections from the substrate interfaces can disturb the spectral and temporal pulse shape, which can effectively be avoided by broadband anti-reflection coatings on the substrate surfaces not coated for other functionality, e.g. spectral filtering.

2.4.1 Mirrors

Metallic mirror coatings offer a high reflectivity and, as long as a precisely polished substrate with low thermal coefficients is provided, a uniform and flat surface appearance. They are protected against chemical degradation and mechanical damage by a thin dielectric cover layer. Both the metal and the dielectric have to be chosen according to the spectral region, e.g. aluminum protected by a MgF_2 layer for UV/Vis applications. For the Vis/NIR region used here, silver mirror coatings with a protective SiO_2 layer have been chosen, offering a uniform reflectivity exceeding 97 %. One has to be aware that the dielectric coating could potentially affect the spectral phase of the reflected light. Therefore, the impact on ultrafast applications should be specified by the manufacturer or in the experiment itself.

For a higher price, some recently available high-reflective dielectric mirrors or metallic mirrors covered by high-reflectivity dielectric coatings can even reach a reflectivity well above 99 %. Especially for the purely dielectric variants, the accepted bandwidth is still a limiting factor, despite the advances in their manufacturing. The upper limit on the feasible amount of sub-wavelength dielectric layers results in a tradeoff between reflec-

tivity, bandwidth and in the case of chirped mirrors additionally the induced spectral phase (see Section 2.9).

In this work, mostly silver-coated mirrors were used. Apart from the exceptions of chirped mirrors inside the oscillator and the external compressor, only the spherical mirrors FM_{1-4} (see Fig. 2.1) have an additional dielectric coating offering increased reflectivity. For experiments where second harmonic generation (SHG) is of concern, silver coatings do not offer enough bandwidth at the blue edge of the spectrum, i.e. the reflectivity drops drastically below wavelengths of 450 nm. Therefore, aluminum coatings or broadband high-reflection (HR) dielectric coatings are a better choice and facilitated in these applications.

2.4.2 Filters

Here, optical filters were used for three reasons: power attenuation, spectral separation of signals and modification of the spectral pulse shape. Since most of these components are not initially developed for ultrafast applications, criteria like damage threshold, surface flatness and substrate thickness may render problems and are often not directly specified by the supplier. Fortunately, the increasing importance and development in this field lead to products specifically designed for short-pulse applications, but the impact of such optics on temporal and spectral pulse shape nevertheless has to be individually tested in the experimental setup it is used in.

Neutral-density filters ideally provide constant attenuation over a wide spectral range, which is either achieved by reflection or absorption. Absorptive filters suffer from lower damage thresholds and are therefore usually not used for initial attenuation of the laser beam. On the other hand, reflective attenuators potentially suffer from wavelength-dependent attenuation-variations, especially when attenuating multiple orders of magnitude from a single filter. It is therefore advantageous to use multiple filters (at the cost of additional dispersion). In the experimental setup, a combination of four neutral-density filters was used for most applications. This was used even for high powers in order to keep dispersion constant to leave the pulse compression at a constant setting. Spectral filters are designed to have a steep edge and high contrast ratios between blocked and transmitted spectral regions. As described in Chapter 4 and seen in Fig. 4.1, a long-pass filter (AHF-76-832, AHF Analysetechnik AG) was used in the detection path when measuring fluorescence to block the laser spectrum. An additional Schott KG5 color glass filter had the purpose to smooth the harsh spectral edge of the laser spectrum created by other components. Spectral selection is not only facilitated by edge filters, but can also be achieved with the pulse shaper with much higher flexibility, as described in Section 2.8.

2.4.3 Beamsplitters

In this work, dielectric plate beamsplitters on thin substrates were used throughout the setup. Most beamsplitters are only designed to deliver a constant and broadband splitting ratio for one incident polarization or are specifically designed for polarization separation, so care has to be taken when light with other than linear s- or p-polarization states is used, e.g. polarization-shaped pulses or fluorescence collection. Some manu-

facturers offer (approximately) unpolarizing plate beamsplitters, yet cube beamsplitters offer a smoother splitting ratio for both s- and p-polarization, at the cost of high dispersion. When both polarization independence and dispersion are parameters to be kept ideal with high priority, thin-film metal beamsplitters are an option. However, one has to be aware that the latter suffer from significant absorption, i.e., 30 % absorption is a realistic value for a 50/50 beamsplitter. Furthermore, mounting the thin foil has to be done with great care to avoid damage while still containing uniform tension across the surface to avoid spatial beam distortions, especially of the reflected beam.

For applications like fluorescence detection, dichroic beamsplitters offer unsurpassed performance by avoiding attenuations of potentially weak signals emitted from the sample while additionally supporting spectral filtering. For consideration of the spectral behavior of such coatings, the arguments discussed for optical filters (Section 2.4.2) apply. As further discussed in chapter 4, for fluorescence micro-spectroscopy measurements, the 50/50 beamsplitter (designed for p-polarization) inside the microscope was exchanged by a dichroic beam splitter (DBS, AHF Analysentechnik, F48-810).

2.4.4 Polarizers

For polarization separation and filtering, Glan-Taylor prisms offer an excellent extinction ratio (on the order of $1{:}10^6$) over a wide spectral range, but like cube beamspitters, the high amount of glass is a drawback, especially for few- or single-cycle laser pulses. Thin-film polarizers are capable of comparable extinction ratios and are therefore exclusively used in this work. Two versions of thin-film filters have become available. On the one hand, a nanoparticle layer with a thickness of about 200 μm can be used, reducing the dispersion caused to the minimum. On the other hand, the same films are available on substrates, potentially increasing the surface flatness of the polarizer (P). When only a small clear aperture is needed, P without substrate can in most cases be used after investigating the impact of the individual optic on the spatial profile of the transmitted beam, preferably after a few meters of propagation. For larger beam profiles or to minimize the impact on the beam profile, beamsplitters with substrates are a good choice. In this experimental setup, both versions of nanoparticle thin-film polarizers are used, labeled P_{1-4} in Fig. 2.1.

2.4.5 Waveplates

Conventional single-material waveplates are designed to offer a specific retardation for a single wavelength, and should therefore only be used in a narrow spectral region around this wavelength. Achromatic waveplates make use of the spectral dependence of multiple birefringent materials to offer constant retardation within a certain tolerance (often on the order of 5 %) over a broad spectral region. Custom-designed retardation plates are specifically optimized for the individual spectral region of the used light source and allow for even lower deviations. The half-wave plate used here is specified to have a tolerance of less than $\pm$ 2 % in the spectral region from 630 nm to 980 nm (B. Halle Nachfl. GmbH), which makes it possible to use it as a precise continuous variable attenuator if used in combination with P_3. The optimized waveplate allows for attenuation up to optical density (OD) 1.5 before the attenuated spectrum is perceptibly altered due to the

residual chromatic retardation dependence. For all measurements, neutral density filters were therefore used in addition to achieve higher overall attenuation (up to OD 9) while never exceeding the mentioned upper level of variable attenuation by the waveplate-polarizer combination.

2.4.6 Focusing optics

In the detection path, the temporal pulse profile usually is of minor importance as long as the optic has a high transmission and an achromatic response. Achromatic lens doublets or triplets with broadband anti-reflection coating are preferred here, because they are easy to use and perform very well. In the excitation path in front of the sample, however, refractive focusing optics are not an option because the additional dispersion can hardly be fully compensated. In addition, the amount of glass the light travels through is different depending on the distance from the optical axis [81] which cannot be removed by common pulse compression methods. These deviations lead to focus-position-dependent pulse duration and pulse phase. Therefore, measurements which are averaged over positions within the focus have reduced temporal resolution. When probing structures that are not significantly smaller than the laser focus, the experiment is affected by the spatial deviations of phase and amplitude of the electric field. For these reasons, reflective focusing optics are used wherever possible in the beam path between oscillator and sample. Spherical aberration in low-incident-angle spherical mirrors could theoretically be avoided by off-axis parabolic mirrors. In reality, this advantage is diminished by the surface imperfections due to the rotational grinding process involved in their manufacturing. This leads to anisotropic scattering and reflection of the incoming light. These losses in beam profile quality and power on most available off-axis parabolic mirrors have let to the decision of using spherical mirrors instead. To minimize spherical aberration and astigmatism, mirrors with small curvatures and therefore long focal lengths are used to make arrangements with small incident angles relative to the mirror surface normals possible. However, since the focus size is inversely proportional to the focal length of an optical component, minimizing it is not achievable with simultaneously avoiding optical aberrations. Instead, one can rely on specialized objectives to attain a tightly focused laser beam.

2.5 Microscope objectives

Depending on the application, curved-mirror-based reflective microscope objectives or refractive objectives, consisting of highly aberration-corrected arrangements of different transmissive materials, can be the ideal choice for probing ultrafast processes at the microscale, potentially even down to the nanoscale. After a short introduction into the description and the limits of spatial resolution, both kinds of microscope objectives shall be discussed and compared to each other.

2.5.1 Spatial resolution

A widely used definition of the resolution of an optical system was already stated by Abbe in 1873 [9]. According to this definition, two dipoles in the sample plane ($z = 0$)

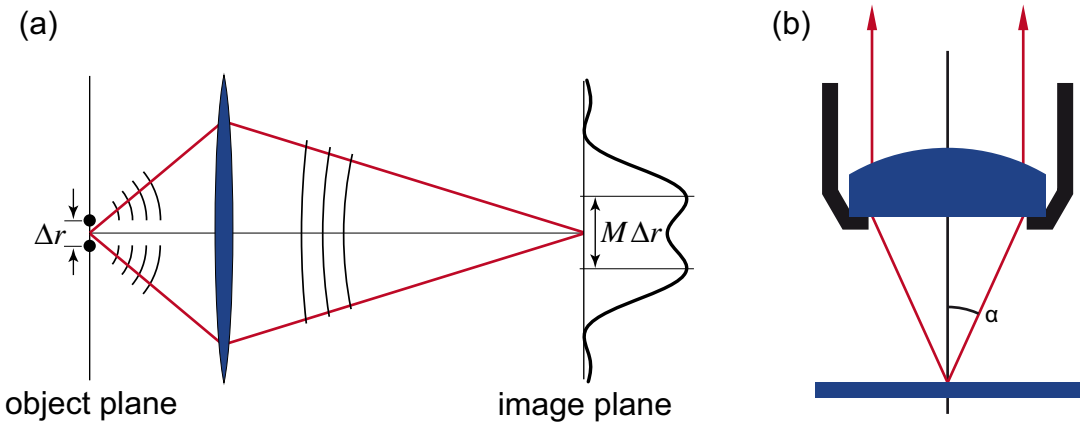

Figure 2.3 | (a) Resolution limit for imaging systems. Light from two sources in the object plane with lateral distance Δr can be resolved if their overlapping point-spread functions mapped onto the image plane show distictive maxima. Due to the magnification M of the optical system, the separation in the image plane is M Δr. Figure adapted and modified from Ref. [82]. (b) The achievable resolution of an optical system increases with α, defined as the maximum half-angle of the entering cone of light. Figure adapted and modified from Ref. [83].

have to be separated by a distance Δr where the maximum of one dipole's point-spread function coincides with the first minimum of the others in order to be distinguishable [compare to Fig. 2.3(a)]. This results in a minimal distance

$$\Delta r_{\mathrm{Min}} = 0.6098\lambda/\mathrm{NA}, \tag{2.1}$$

where

$$\mathrm{NA} = n\,\sin(\alpha) \tag{2.2}$$

defines the numerical aperture of the optical system embedded into a medium with refractive index n [82]. As seen in Fig. 2.3(b), α is defined as the maximum half-angle of the cone of light entering the optical system. This general resolution limit may be further reduced by a-priori knowledge about the system, e.g. a specific alignment of the two dipoles. Further resolution improvement is achieved when also detecting evanescent waves, i.e. utilizing near-field optics. The latter does, however, require further adaptions to the experimental setup and may set limits to the sample topography. Therefore, when using a light source with given spectral output and relying solely on far-field detection, the remaining parameter that determines the reachable spatial resolution is the NA of the microscope objective lens. For reflective as well as refractive objectives surrounded by air (or vacuum), the limit is NA < 1 for a single objective. This maximum value can be understood as the collection of all light from one half-space of the focal point. The resolution can further be increased by the use of multiple objectives, e.g., as facilitated in 4π microscopy [84]. Refractive objective lenses can be designed to operate close to the maximal achievable resolution by choosing low working distances, resulting in NA $= 0.95$ designs being available from many manufacturers. In contrast, the reflective objectives from major companies are limited to a NA around 0.5, limiting the reachable spatial resolution. Whether this limitation is prevailed by the advantages of negligible dispersion and minimized optical aberrations depends on the observed system.

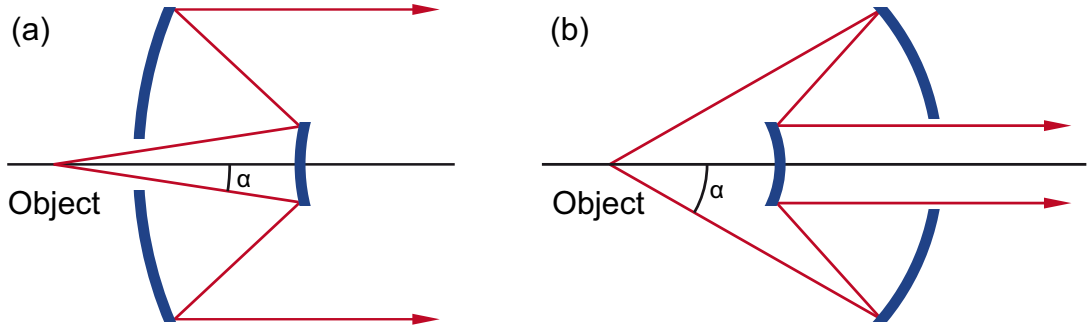

Figure 2.4 | (a) The (inverse) Cassegrain objective consists of a small primary convex mirror and a secondary concave mirror. (b) Schwarzschild objectives facilitate a primary concave mirror in addition to a smaller secondary convex mirror. Figure adapted and modified from Ref. [85].

2.5.2 Reflective microscope objectives

A straight-forward approach when using a high spectral range is to use multiple reflective optics to avoid both chromatic dispersion as well as off-axis reflections. In a simple two-spherical-mirror design seen in Fig. 2.4(a), the light from an object in the focal plane hits the primary convex mirror and is afterwards reflected and collimated by a bigger secondary concave mirror [86]. However, spherical aberration can additionally be eliminated by using a classical Cassegrain objective with hyperbolic primary and parabolic secondary mirror. The coma remains for this reversed Cassegrain design, but can be reduced by slight adjustments in the mirror curvatures. Further improvements were made through the development of the Schwarzschild microscope-objective design sketched in Fig. 2.4(b). In its reversed telephoto type, the light from the focal plane is first reflected from a concave mirror to a secondary smaller convex mirror. Despite the fact that both mirrors are spherical, the focusing is automatically free of coma, astigmatism and spherical aberration if they are aligned correctly [86].

2.5.3 Refractive microscope objectives

Many applications benefit from refractive microscope objectives offering a better resolution when the disadvantages, e.g. concerning broadband or ultrafast laser pulses, can be sufficiently compensated. To quantify the advantages in spatial resolution, according to Equ. 2.1, the diffraction limit scales inversely with the NA. The amount of collected light scales quadratically with the NA assuming an isotropic emission, e.g., an objective with NA 1.4 collects 8 times as much light as one with NA 0.5. It was mentioned that optics embedded in air cannot overcome the limit of unity NA, but other media can. Due to the advantages when investigating biological samples, water is a common choice as immersion medium, offering objectives with NA in the range up to 1.25 due to its refractive index of $n = 1.33$ in the visible range [87]. Different immersion oils offer even higher resolution, most common with $n = 1.52$. With high-refractive-index oil ($n = 1.66$), objectives with NA = 1.57 are available. Correcting aberrations over a broad spectrum over the full aperture requires complex lens systems. Achromats, which are capable of correcting spherical aberration for a single wavelength and chromatic aberration for

two wavelengths are usually not sufficient for high demanding imaging applications. A common choice are therefore Plan Apochromats, which correct spherical aberration for at least three wavelengths, chromatic aberrations for four wavelengths and remove the field curvature that would otherwise distort the focal plane.

In the experimental demonstrations done as part of this thesis, a highly corrected microscope objective (Plan Apo, 100x, NA 1.4, Nikon) was therefore used to obtain a high resolution simultaneously in space and time, as shown below in section 2.10. The design of this and other highly corrected objectives does however usually not include optimization of the temporal profile evolution through the complex lens system, i.e. due to optical path deviations as function of distance from the optical axis. This dependency could be calculated, e.g. by ray-tracing, but only when the exact composition of lens shapes and materials is known. This is usually not specified by manufacturers since it is subject to trade secrets. As a result, such calculations or measurements are usually not done or published. However, when designed for phase-sensitive methods like phase-contrast microscopy, the optics have to maintain the phase dependency over the whole aperture. This also ensures conservation of the temporal pulse profile to a certain degree [88]. For molecular spectroscopy like described in Chapter 4, the low NA marks no principle limitation. However, it reduces the yield of the detected emission and thereby the effective quantum yield of the detection. Compensating the lower yield by increased acquisition time may be no option due to sample degradation.

In the case of plasmonic nanowires like the nano-interferometers used in Chapter 3, even stronger dependence on the NA of the objective can be observed. Far-field coupling of the plasmonic modes has a strong angular dependence, especially when not enhanced by antenna-structures. As an example, most of the light emitted from a simply terminated wire radiates off into the half-space of the high-refractive-index-material (i.e. the substrate) at low angles relative to the nanowire and thereby the plasmon-propagation-direction [2, 79]. A microscope objective collecting light with a low NA, in a small cone perpendicular to the nanowire axis, would be a poor choice for this experiment, especially when not placed behind the substrate. Furthermore, direct scattering of excitation position of the nanointerferometer-antennas is only spatially separated from the emission position by 4 μm. With emissions being much weaker (in this case ca. 1:10^4), resolution limitations of low-NA objectives makes spatial separation challenging.

In general, gathering of additional information on the temporal and spatial profile of the laser focus in the individual experimental configuration is of great importance to ensure the validity of results obtained from ultrafast measurements. Even more fundamentally, the success of efficient pulse compression in space and time depends on the capabilities of the used microscope objective. This can be confirmed by characterization of the temporal pulse shape directly in the focus, as shown below in Section 2.9.6. Further investigations are conducted with the help of a sub-wavelength-sized nano-probe in Section 2.10.

2.6 Detectors

To quantify and characterize the light emitted from a light source, components of the experimental setup or samples under investigation, specialized light detectors are used. They are categorized into integrating devices that consist of a single active pixel and into multi-pixel arrays, e.g. used for resolving spatial image information or spectrally resolved information.

2.6.1 Spectrally integrated detection

Compact and versatile integrating detectors are semiconductor photodiodes, tailored for the application at hand by choosing a suitable size of the active area and the spectral working range. The bandgap size of the semiconductor dictates the spectral response, which makes e.g. GaP a good choice for near ultraviolet (UV) down to 150 nm wavelength, Si for the full visible spectrum into both UV and NIR ranges and InGaAs for the NIR spectral region up to approximately 1700 nm wavelength. The gain can be increased by transistor-based amplification when performing experiments with low photon counts. For high-speed amplification, the rise and fall times of the diode response has to be considered as well as the maximum bandwidth of the amplification circuit, e.g., reaching maximal resolution of the order of 1 GHz for Si photodiodes. For low-light applications, avalanche photodetectors potentially offer a better signal-to-noise ratio because of their lower dark noise. Avalanche photodiodes (APDs) in counting mode and photomultiplier tubes (PMTs) are good choices for single-photon counting. APDs are preferred for broadband applications and in the visible and NIR range, whereas most PMTs operate best in the visible to UV range.

2.6.2 Spectrally resolved detection

When the detector is required to spectrally resolve the incoming light, it is usually spatially separated by a diffractive element, i.e. a prism, a reflective grating or a transmission grating. The latter offers the advantage of flexibility by adapting the angular spread of the spectral components by adjusting the grating constant. Similar adaption can only be achieved by changing the distance between diffractive element and detector in the case of a prism (for a given prism material), which might not be feasible for detector assemblies with low overall dimensions.

The spatially dispersed spectrum can then be measured with a single integrating detector of all types mentioned above by either rotating the diffractive element or moving the detector. This is done, e.g., in commercial UV/VIS/NIR spectrometers like the Jasco V-670 used in the scope of this work. Multiple light sources, detectors and gratings are included and exchanged in dependence of the current position in the large spectral range to ensure persistent high sensitivity. A method often used in IR spectroscopy is a Fourier-transform spectrometer where a pair of pulses is created, e.g., in an interferometer. The absorption or transmission of the sample is detected in dependence of the interpulse delay by a single, spectrally integrating detector. By Fourier transformation of the trace, the absorption/transmission spectrum is retrieved [89].

A multifold speed-up of the data acquisition can be achieved by simultaneous detection of all spectral components, achieved by using an array of detection pixels. For a small amount of pixels, linear arrays of the described detectors can be used. Gaps between neighboring pixels can be compensated by micro-lens-arrays in front of the detector pixels. Cost-effectiveness and physical dimension of the detector assembly favors integrated multi-pixel arrays, especially for larger amounts of pixels.

Both charge-coupled devices (CCDs) and complementary metal-oxide-semiconductors (CMOS) benefit from the high interest in fast and low-noise cameras with a high quantum yield in a wide range of industrial and scientific fields. Pixel sizes of a few micron side length with millions of pixels in two-dimensional arrays make it possible to measure broad spectra at high resolution while additionally allowing measurement of multiple spectra at once by illuminating multiple regions along the second array dimensions with different beams, e.g. reference spectra or polarization-separated signals dispersed by an additional polarizing beamsplitter in front of the diffractive element.

For low-light applications, cameras with bigger pixels are used to reduce the noise floor. Especially for high integration times above 1 s, integrated devices at room temperature suffer from increased dark noise levels. Therefore, actively thermo-electric cooled sensors are offered by major manufacturers to allow for spectrally resolved measurements of low photon counts, where high integration times are needed.

A powerful tool to decrease noise levels is the use of lock-in detection. A chopping wheel in the laser beam is used to switch the light on and off at a certain frequency, an amplifier is synchronized with the frequency of the chopping wheel to block any contributions of the measured signal that are not modulated with the switching frequency. It is advised to avoid setting the lock-in frequency to common noise frequencies and their harmonics. The most prominent source for frequency-specific noise is the frequency of the power grid, i.e. 50 Hz or 60 Hz, depending on the region.

In this work, pulse compression with the help of the PRISM algorithm [90] was done by filtering the signal from a photodiode with a lock-in amplifier and chopper wheel operating at 365 Hz, thereby separating the signal from power grid noise at the frequencies 50 Hz, 100 Hz, and higher harmonics.

Apart from lock-in amplification, the influences of the power grid can effectively be suppressed by making sure all relevant electrical components are grounded properly.

2.6.3 Linearity of the detector

For all used detectors, the linearity of the intensity response has to be characterized, corrected if needed and operation in a linear or linearized response region has to be ensured. The measurement of the linearity can be performed by exchanging ND filters of known attenuation. Another and more versatile option for characterization is to utilize a half-wave plate in combination with a linear polarizer, as described in Section 2.4.5. Figure 2.5 shows the linearity measurement of APD 1 that is part of the microscope setup (compare Fig. 2.1). The measurement consists of a series of five individual power scans conducted by rotating a custom-manufactured broadband half-wave plate (B. Halle Nachfl. GmbH). Each color of the dots in Fig. 2.5 marks an individual scan of the power from maximum transmission down to 3 % for laser pulses with a center wavelength of 850 nm and a bandwidth of 10 nm. This spectral region was chosen because it is also

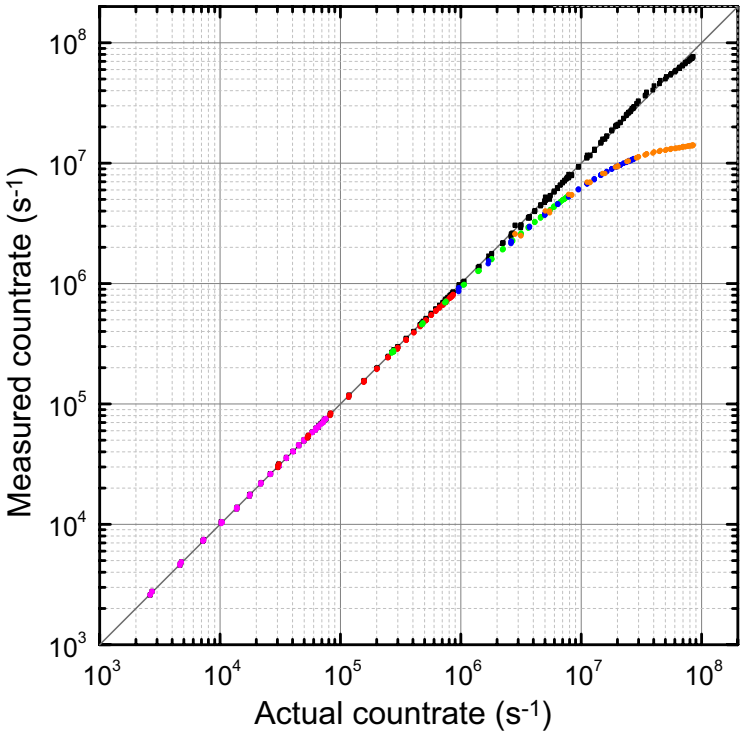

Figure 2.5 | A linearity measurement of APD 1. Five individual power scans, (dots, each plotted in a different color), were taken by rotating a half-wave plate in front of a polarizer. Additional constant attenuation by ND filters was used to extend the dynamic range of 1.5 orders of magnitude from a single scan to more than 4 orders of magnitude. The sub-linear response of the diode dominant for high count rates originates from the death time of the diode after a photon is detected. All measured data was globally fitted according to Equ. 2.3, yielding a dead time of 58 ns. The inverse formula applied as correction to the data results in the linearized diode response plotted as black squares.

covered by fluorescence emission from the metal-organic dye F_{16}ZnPc investigated in Chapter 4. The limited bandwidth of the spectral region minimizes the influence of the spectral dependency of the half-wave plate. The scans were conducted with different ND filters in the light path in front of the waveplate to cover more than four orders of magnitude of incident laser power.

As evident from significant deviations from the linear dependency above count rates on the order of 10^6 s^{-1}, the APD response runs into a regime of saturation. After a photon is detected, the diode is depleted from charge carriers, preventing it from detecting another photon until replenished. This dead time affects the linearity of the detector at intensities where the impact of two photons within this period becomes statistically relevant. A dead-time correction can be used to model the impact of the dead time onto the linearity,

$$n_{\mathrm{corr}} = \frac{n_{\mathrm{meas}}}{1 - n_{\mathrm{meas}} \cdot \tau_0}, \tag{2.3}$$

where n_{meas} denotes the measured count rate, n_{corr} the corrected count rate and τ_0 the dead time of the detector. The formula has been fitted globally to the five measured

APD count rate scans, yielding a dead time of 58 ns. The inverse function is then used to correct the raw data, as depicted by the black squares in Fig. 2.5. The corrected response retains its linearity to the full measured range, thereby extending the effective dynamic range of the APD by two orders of magnitude.

In the case of detectors capable of spectral resolution, the frequency dependence of the quantum yield can also be observed and corrected. This requires a light source with known broadband intensity distribution, i.e., a black body radiator where the spectrum is given by Planck's law [91]. Alternatively, manufacturers of white-light lamps often provide characterization curves of their products' output spectra measured with calibrated detectors. Likewise, some detectors are already supplied with a calibration curve and guaranteed to deliver a spectrally flat response within certain spectral range and accuracy.

2.7 The confocal microscope setup

The microscope assembly used in the scope of this thesis can be seen in Fig. 2.1 and has been elaborately described in the past [80]. All optics on the designated breadboard were selected for maximum stability at a low beam height of 50 mm. As a result, beam stability is increased, both on the timescale of seconds required for a single data point acquisition as well as the long-time stability over a spectroscopic pulse scan taking a whole day. To adjust the beam diameter to fill the back-aperture of the microscope objective, the beam first passes through a Keplerian mirror telescope ($FM_{1,2}$ in Fig. 2.1). A 100-μm pinhole in the focus of the telescope ensures reproducible incoupling on a day-to-day basis and additionally cleans up the spatial beam profile. By optimizing the microscope incoupling using an iris diaphragm in front of the microscope breadboard and the pinhole, reproducible beam pointing into the microscope objective is achieved on a daily basis, assuming the optical assembly on the microscope breadboard remains unchanged.

As beamsplitter BS_1, a broadband 50 % beamsplitter is used for most experiments. It is swapped for a dichroic beamsplitter (DBS) (F48-810, AHF Analysentechnik) in the case of fluorescence measurements presented in Chapter 4 to increase the quantum yield of the detection path. The beam transmitted by BS_1 is used as reference beam, the reflected beam is coupled into the back aperture of the microscope objective. The sample is usually located on a microscope cover slide and positioned with a 3D piezo-translation-stage (P-517.3CL, PI, Germany). Light collected by the same objective is transmitted through BS_1 to a telescope with a pinhole in the focus for confocal measurements (compare [80]). By utilization of confocal detection, the spatial resolution is increased [82]. Moreover, by rotating the piezo tip-tilt mirror (S-334.2SL, PI, Germany) located between BS_1 and the telescope, the xy-location inside the sample plane that is mapped onto the detection pinhole can be chosen independently from the excitation position. This feature has already been used for propagation measurements of surface plasmon polaritons in the past [4, 79, 80, 92, 93] and was also used in measurements on plasmonic nanointerferometers in Chapter 3.

The beam initially transmitted by BS_1 is used as reference path for spectral interference measurements [94]. The path contains a total-internal-reflection prism (N-BK7,

Schott) to introduce dispersion to match the amount of glass in the signal path, mainly the twice passed microscope objective [95]. The two beams are then recombined by a second beamsplitter (BS_2). With the help of P_4 (see Fig. 2.1), the detected polarization direction is chosen, e.g. to optimize the intensity of the desired signal relative to other emissions from the sample plane. In general, a crossed polarizer scheme can be used to attenuate the directly reflected excitation. The light is detected either by APD_1, APD_2 or the two-dimensional (2D) spectrometer, depending on whether high sensitivity or spectrally resolved detection is the highest priority.

Modifications of the temporal pulse profile can be conducted by a variety of methods. A selection of them will be presented now, starting with one of the most general and versatile, the pulse shaper.

2.8 Pulse shapers

Pulse shapers have proven suitable for a wide variety of applications controlling ultrafast laser pulses for experiments with high spatial resolution, including selective nonlinear microscopy [55, 96], coherent control and coherent two-dimensional spectroscopy of plasmonic nanostructures [4, 97–100] and observation of energy transfer in single light-harvesting complexes [71]. However, depending on the application at hand, different types and designs of pulse shapers may prove advantageous. In this sections, the most common types used in experiments facilitating ultrafast pulses shall briefly be reviewed. For a more detailed description of optical pulse shaping, the reader is referred to more elaborate reviews [54, 101, 102].

The considered pulse shapers differ in the functional element: In an acousto-optic modulator (AOM), the refractive-index differences inside a birefringent crystal are exploited while in a spatial light modulator (SLM), the anisotropy of the refractive index of liquid crystals is utilized. When considering the sole purpose of phase compensation, the use of a single device/layer is sufficient to induce wavelength-dependent phase modulation. In general, additional modification of the full vector-field, i.e., phase, amplitude, and polarization has been realized in both approaches of pulse-shaper design [103–108].

2.8.1 Acousto-optic modulators

AOMs, when used in the type of an acousto-optic programmable dispersive filter, have the advantage of being compact devices in which no optical components need to be adjusted during regular operation. Instead, an individually chirped acoustic wave is generated and travels through a birefringent crystal, as shown in Fig. 2.6. An optical pulse incident in parallel direction is modulated by the acoustic field acting as a grating with adjustable period pattern. Due to its much lower phase velocity, the acoustic wave can be assumed as static in comparison to the electro-magnetic wave. Amplitude and phase profile from the static acoustic wave pattern are imprinted onto the laser pulse on a shot-to-shot basis since every laser pulse is alternated by an individual acoustic wave. When placing two AOM shaping devices in the two arms of an interferometer with polarizing beamsplitters, the polarization state of the recombined beam can be controlled in addition to the amplitude and the phase. The drawback of the AOM

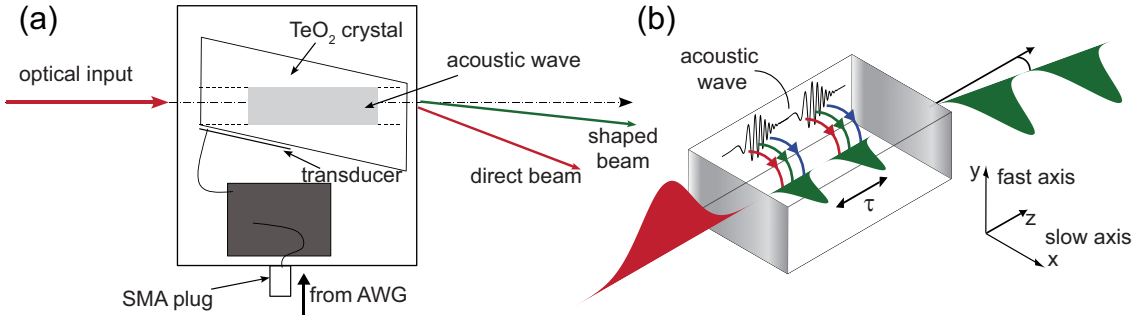

Figure 2.6 | Working principle of an acousto-optic programmable dispersive filter. (a) A waveform is created in the acoustic wave generator (AWG) and coupled into a birefringent crystal (TeO_2 in this case). Laser pulses that are coupled into the crystals are modulated by the influence of the acoustic wave. The shaped pulse does subsequently exit the crystal under a slight angle. (b) Light modulation inside the crystal. The acoustic wave creates a complex pattern of local longitudinal variations of the refractive index. Spectral fractions of the incident laser light are diffracted from the initial fast axis of the crystal to the slow axis at positions with matching acoustic wave frequencies along the propagation direction. In the plotted example, a pair of compressed double pulses is shaped from a single incident chirped pulse. Figure adapted and modified from Refs. [108, 109].

principle is the limitation of the repetition rate since it takes time for the acoustic wave to travel through the crystal. Common designs with crystal lengths of a few centimeters are thereby limited to a few kHz repetition rate. When placing the birefringent crystal inside the Fourier plane of a $4f$ configuration, the spatial separation of the spectral components allows for modulation along a much shorter propagation length. With a crystal thickness of 5 mm, operation at 100 kHz has been demonstrated [110]. However, this diminishes the advantage of the compact design. Still, the repetition rate does not allow for shaping of every pulse from a laser system with 80 MHz repetition rate like the one used in this work.

2.8.2 Liquid-crystal displays

In LCD-based pulse shapers, liquid crystals are usually arranged in a linear array and positioned between two transparent electrode layers that can be addressed individually for each pixel, tilting the crystals into the direction of the electric field. Thereby, the refractive index of the layer is changed, introducing a programmable phase shift to the light transmitting the layer normal to the surface (see Fig. 2.7). Changes in the orientation of the liquid crystals are delayed after to the application of a control voltage, typically on the order of 100 ms. In contrast to AOM-based pulse shapers, the static phase mask can be used at high repetition rates or even continuously after that initial switching. To do that, the LCD array is placed in the Fourier plane of a $4f$ prism/grating configuration, equal to the high-repetition-rate AOM described above. The design for the original $4f$-based pulse shaper was presented in 1983 [111]. It is built in the single-pass-design, where the light is guided through the symmetrical $4f$ geometry once. In this single pass, the spectral components of the incident pulse are spatially dispersed by a grating or prism and consecutively individually focused onto the linear LCD array in

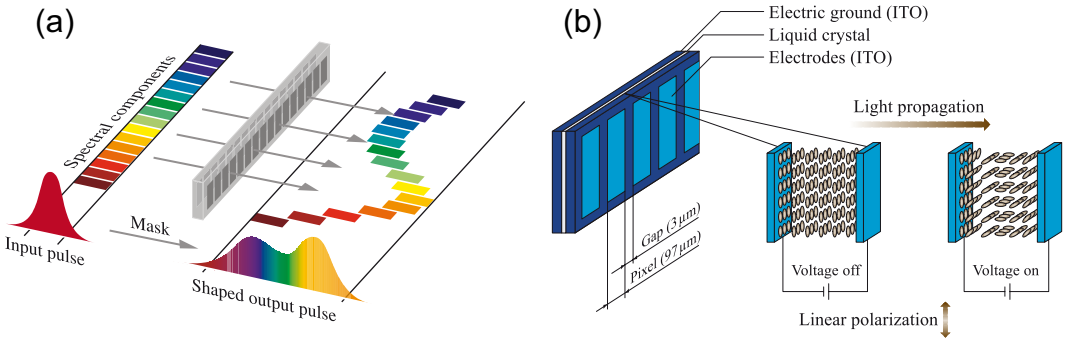

Figure 2.7 | Working principle of a LCD-based pulse shaper. (a) The spectral components of the incoming light are spatially separated and individually focused onto a linear array of LCD pixels. By adjusting the phase imprinted onto the transmitted light, spectral components can, e.g., be individually delayed. (b) A film of liquid crystals is embedded between two layers consisting of a linear array of transparent indium tin oxide (ITO) electrodes. When a voltage is applied between the electrodes, the liquid crystals align along the direction of the field. Thereby, a dispersion change is induced along the direction of the light propagation due to the birefringence of the crystals. Figure adapted and modified from Ref. [101].

the Fourier plane. Focusing is commonly (but not obligatory) done only in one spatial dimension by a cylindrical lens or mirror to average over inhomogeneities in the liquid crystal layer and to increase the damage threshold. The beams are then recombined by a mirrored arrangement of the first half of the $4f$ setup. Alternative approaches utilize a double-pass design, where the beampath is folded back either directly after the LCD layers in the Fourier plane or after the second grating, i.e., the full $4f$ geometry is passed twice. The advantage of passing the LCD layers twice is that the amount of introduced phase and thereby the temporal shaping window is doubled. The impact of different geometries onto pulse-shaper artifacts will be discussed below in Section 2.12.

As already presented by Weiner and coworkers in 1990 [112], a single LCD layer is sufficient for phase modulation. If a second layer is added and the liquid crystal axis is chosen to be $\pm 45°$ relative to the polarization of the incident light, phase shift differences in the two layers additionally introduce a controllable polarization shift. By placing a linear polarizer after the LCD, which is usually done either directly after the second LCD layer or after the second grating, the polarization modulation is converted into an amplitude modulation [53, 102, 113]. By variation of the $4f$ design, including a thin-film polarizing beamsplitter to map the two perpendicular polarizations onto different parts of the LCD array, full vectorfield control has been achieved [103–107].

Due to their slow response time, LCD-based pulse shapers are not suited for shot-to-shot operation with pulsed light sources operating at or above repetition rates in the kHz regime. On the other hand, they are a good choice for experimental setups excelling in reducing shot noise and rapid gathering of photon statistics due to the high repetition rate of the light source, best paired with single-photon-counting modules like the avalanche photo-diodes used in this work. Such pulse-shaper designs have already shown to be suitable for sub-10-fs laser pulses with octave-spanning spectra [114, 115].

For this reason, a two-layer LCD pulse shaper is used in this work, using a double-layer 640-pixel spatial light modulator (SLM) (SLM-S640d, Jenoptik AG) as active element of

the $4f$ setup. The delay between application of a voltage pattern and the full reorientation of the liquid crystals is on the order of 500 ms for this model. The extinction ratio of the p-polarization of the incident light is optimized by P_1 (LPVIS050-MP2, Thorlabs) in front of the pulse shaper. An identical polarizer (P_2) directly after the $4f$ setup is used to transform the polarization modulation introduced by the LCD into amplitude modulation by transmitting only the p-polarized component. Spatial separation of the spectral components is done by volume phase-holographic gratings (Wasatch Photonics). They are designed for maximum transmission at 800 nm (> 90 %) and offer transmission above 65 % for the whole spectral range of the pulse shaper design, from 650 nm to 950 nm wavelength for s- and p-polarization. The spectral resolution of the 640-pixel LCD is 0.53 nm/pixel. According to the Nyquist theorem, the shaping window is $\pm$ 1.9 ps and the maximal second-order spectral phase that can be introduced is about $\pm$ 5000 fs^2 [116].

Both types of shaper technologies, the AOM and the LCD designs, bring with them an inherent set of imperfections which lead to artifacts and deviations in the desired shaped pulse forms. Some of the artifacts can be minimized by proper design choices and a perfect calibration of the beam path and the active element. As described, an LCD pulse shaper in single-pass geometry is used here. The implications of this choice on space–time coupling and other artifacts will be discussed in Section 2.12, together with correction procedures that can minimize their influence.

2.9 Pulse compression

Taking care of the spatial and temporal beam profile is crucial. However, it does not solve the problem of pulse pre-compression to compensate the higher order spectral phase mainly introduced by the transmissive optics that cannot be avoided or replaced. There are different methods for pulse compression that could be conducted, but not all of them are capable of controlling the phase over the required spectral range with sufficient degrees of freedom. Accordingly, the Tailor expansion of the spectral phase around the center frequency of the laser ω_0,

$$\begin{aligned} \Phi(\omega) &= \textstyle\sum_{p=0}^{\infty} \frac{1}{p!} \left.\frac{\partial^p \Phi(\omega_0)}{\partial \omega^p}\right|_{\omega_0} (\omega - \omega_0)^p = \\ &= \Phi(\omega_0) + \Phi'(\omega_0)(\omega - \omega_0) + \tfrac{1}{2}\Phi''(\omega_0)(\omega - \omega_0)^2 + \tfrac{1}{6}\Phi'''(\omega_0)(\omega - \omega_0)^3 + ..., \end{aligned} \tag{2.4}$$

can be compensated to a certain order. As is listed for common pulse compression methods from the overview in Fig. 2.8, prism [Fig. 2.8(a)] and grating [Fig. 2.8(b)] compression mainly minimizes the quadratic spectral phase coefficient Φ''. Chirped mirrors [Fig. 2.8(c)] are typically designed to match up to the fourth order coefficient Φ'''' induced by common types of glass (e.g. BaF_2 or fused silica). In pulse shapers, the amount of degrees of freedom for phase compensation matches the amount of pixels in SLM-based pulse shapers (Figs. 2.8e) and is given by the resolution of the acoustic wave in AOM-based pulse shapers (Figs. 2.8d). An overview over each of the mentioned methods shall be given now.

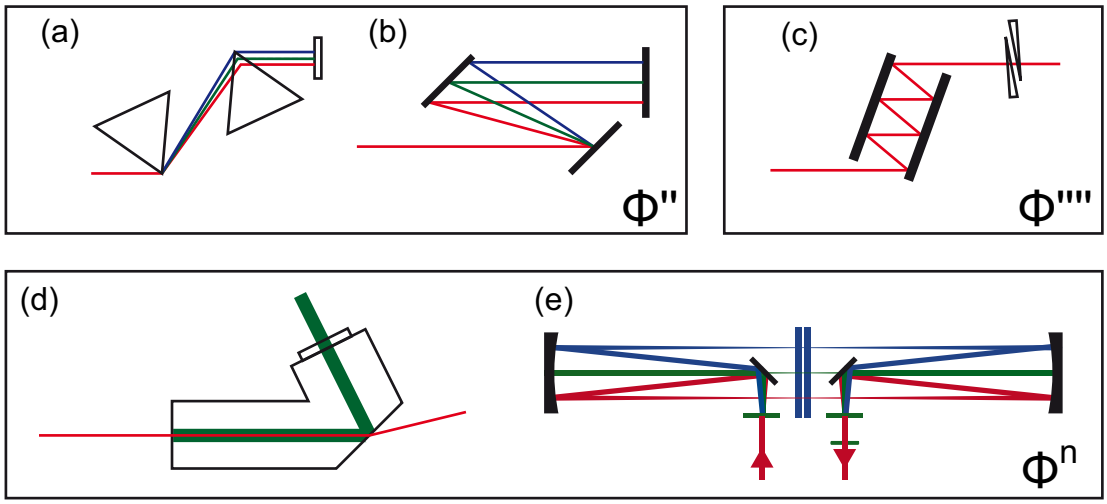

Figure 2.8 | Methods for chirp compensation, categorized by the highest polynomial order of spectral phase they are designed to address. (a) Prism compressor for compensation up to Φ''. The spectral components are spatially dispersed by a Brewster angle dispersing prism. A second prism is used for collimation. By a second pair of prisms or a back-folded geometry, a geometrical path-length difference is introduced between the spectral components. Subsequently, they are recombined. (b) Grating compressor for compensation up to Φ''. With a working principle equivalent to a prism compressor, gratings offer the introduction of high amounts of spectral phase. (c) Chirped mirrors for compensation up to Φ''''. The dielectric mirror coatings are tailored to offer a spectral dependence on the penetration depth, introducing a fixed amount of path length difference at each reflection. Fine-tuning is facilitated by an additional pair of glass wedges. Pulse shapers of the type (d) AOM and (e) LCD offer compensation of spectral phase up to a high order Φ^n, depending on their complexity, i.e., resolution of the acoustic wave or accordingly, the amount of pixels.

2.9.1 Prism and grating compressors

A commonly used geometry is the prism compressor, which was also facilitated in former versions of the experimental setup used in this work. However, the distances between the prisms and the propagated amount of extra glass in the prisms itself mainly tunes the second order coefficient of the spectral phase (see Eq. 2.4) with limited additional control over the third order. Using optical gratings instead of prisms renders an equal flexibility, typically with larger absolute values. For the purpose of this work, none of the two methods would be sufficient by itself. However, in recent years a combination of both, the grism, became available which could potentially compress broadband pulses [117].

2.9.2 Chirped mirrors

The approach that was used here instead is based on dielectric mirrors. The performance and the design limitations of dielectric mirrors are based on the amount of possible subwavelength layers. The latter has steadily grown in the last years, which lead to the advent of the previously mentioned broadband high reflective mirrors. A higher order spectral phase is introduced onto the reflected light if the penetration depth of

the spectral components is not uniform, effectively by the introduction of a spectrally dependent path length. This effect is exploited in chirped mirrors, where the introduced phase is tailored over a large bandwidth to compensate transmission through common glass types up to the fourth order of the spectral phase. The amount of possible surface layers leads to a trade-off between introduced phase and bandwidth, making it desirable to closely match the mirror design to the laser spectrum. The exact desired amount of phase compensation is then usually achieved by multiple reflections off pairs of chirped mirrors combined with phase fine tuning done by a pair of glass wedges. Both the use of grisms and chirped mirrors allows for pulse pre-compression for the use of a high-NA microscope objective with broadband pulses.

In the experimental setup at hand, chirped mirrors are used inside the cavity to allow for mode-locked operation and after the laser for pre-compression. To compensate for all dispersive media with chirped mirrors alone would be possible using around 30 pairs of bounces on the used chirped mirror type (DCM7, Venteon), which are specified at 120 fs^2 second-order phase-compensation at 800 nm per bounce-pair. Successful facilitation of such large amounts of reflections have been shown, but have downsides like the degradation of the spatial beam profile, mostly by off-center reflections on mirrors with surface coating inhomogeneities or a small clear aperture. Therefore, only a part of the precompensation (4 bounce pairs) was done by the chirped mirrors.

2.9.3 Pulse-shaper-based compression

In contrast to the small number of degrees of freedom offered by the methods described above, pulse shapers allow for arbitrary phase masks that can be applied to the laser pulse, thereby making it the most flexible tool for pulse compression. The limit of the amount of phase that can be applied, the shaping window, can be calculated if the geometry of the pulse shaper is known [102, 116]. The pulse shaper used in this work is capable of delivering a linear phase of 1.9 ps or a quadratic phase of 5000 fs^2/rad. It has to be kept in mind that applying a constant offset phase reduces shaping window for other uses, e.g., generation of multiple sub-pulses for spectroscopy.

In order to determine the phase which has to be applied to the pulse shaper to compress the pulse, a nonlinear feedback and a systematic phase scan were facilitated. These tools to determine the overall spectral phase imprinted on the laser pulses on the path towards the sample position are presented now.

2.9.4 Nonlinear feedback

Assuming one has the possibility to compress the temporal profile of a laser pulse at a desired location by any of the mentioned methods, the result has to be confirmed and in the ideal case, the full complex vectorfield has to be retrieved. Since linear processes are sensitive only to the amplitude but not on the phase of the field, a nonlinear process has to be exploited. Mechanisms often used as nonlinear feedback are second harmonic or sum frequency generation in nonlinear crystals like β-barium borate (BBO), iron(III) iodate ($Fe(IO_3)_3$), or barium titanate ($BaTiO_3$). Apart from nonlinear crystals, other nonlinear processes can also be used yielding comparable results [118, 119], including higher-order photodetectors (e.g. TPPDs), photoemission, and photocurrents.

2.9.5 Pulse characterization and compression

Pulse compression can be achieved by maximizing the feedback from a nonlinear process with the reasonable assumption that the transform-limited laser pulse defines the global maximum of the yield. A straight-forward pulse-compression approach is to manipulate the spectral phase and maximizing a nonlinear feedback from any of the possibilities described above. This can also be done by varying the phase with the help of the other described compression setups, i.e. changing the tip-to-tip-distance in a prism or grating compressor, or by changing the amount of reflections on chirped mirrors. For fine-tuning the compression phase, the light path length through dispersive media, i.e. a pair of glass wedges or one of the prisms, can be slightly varied. When using a pulse shaper, an equal scan can be conducted by varying the second order spectral phase, or even including scans of higher orders to improve the result.

Phase optimization by simple nonlinear feedback maximization relies on the assumption that a transform-limited pulse, i.e., a flat spectral phase, defines the optimum. However, the result could as well be merely a local optimum. Therefore, to reach a reliable result, supporting measurements should be conducted. From the higher-order autocorrelation, the spectral phase cannot be extracted because the complex laser pulse leading to a trace is not unique. When the spectral amplitude is known, the experimentally measured autocorrelation can be compared to a calculated trace using the measured spectrum and assuming a flat spectral phase. A close resemblance of these two curves in combination with a minimized temporal width of the experimentally achieved autocorrelation have proven to be conclusive arguments for a successful compression of the laser pulse.

A conclusive and complete argument for the pulse length and overall temporal shape can only be obtained by full retrieval of either the full spectral or temporal vectorfield. Knowledge from one of the two domains suffices, as they can be deduced from each other by Fourier transformation. Furthermore, when assuming a linear polarization state, which is a proper assumption for many experiments, the polarization perpendicular to the primary polarization direction (as well as the z-component in direction of propagation) does not need to be characterized.

When considering full phase retrieval in the time domain, in most cases, there is no other process available fast enough to gate the laser pulse at a femtosecond timescale. Therefore, a delayed replica of the pulse itself, for example generated by interferometric methods, can be used for pulse characterization.

Generation of a collinear pulse pair in applications as ultrafast spectroscopy is often facilitated by a Michelson interferometer or a Mach–Zehnder interferometer. Variation of the inter-pulse delay τ is either done by moving mirrors on a linear translation stage or by varying the amount of dispersive media in one arm of the interferometer, both changing the relative optical path length between the two generated pulse copies. Manipulation of the higher order phase or the polarization state of one of the pulse copies can also be introduced, which is exploited in a variety of pulse compression methods.

It shall be noted here that pulse shapers can of course also be used for generation of one or more pulse copies, with the advantage of inherent phase stability. In addition, this method offers arbitrary variation of the phase relation between pulses, often used for controlling the relative carrier-envelope phase.

Facilitation of such a pulse pair with variable temporal delay initiates the following selection of pulse-compression methods. A double-pulse scan with spectrally integrated detection involving a nonlinear feedback yields an autocorrelation, which can give insight over the temporal shape of the laser pules as described above. Using a spectrally resolved detection, however, results in a time-frequency trace of the method called frequency-resolved optical gating (FROG) [120–122]. From this trace, the full field of the laser pulses can be reconstructed. Apart from the sign of the spectral phase, every change in the spectral/temporal shape of the laser pulse results in a different, unique FROG trace. This also means that only the accuracy of the measurement limits the arbitrarily exact reconstruction of the field. When using sum-frequency generation of the laser pulse and a chirped reference pulse, the spectral phase interferometry for direct electric-field reconstruction (SPIDER) algorithm [123–126] allows for quick reconstruction of the electric field, as the name implies.

When a pulse shaper is used instead of interferometric methods, amplitude modulation is not necessarily required for pulse compression. Phase-only methods for pulse-shaper-based pulse compression include simple search algorithms for scanning the phase which, besides the advantage of their simplicity, take a long time to complete due to their high amount of degrees of freedom. To speed up this process, evolutionary algorithms and simulated annealing have been used [127–129]. A popular algorithm used today is called multiphoton intrapulse interference phase scan (MIIPS) [130], where, in the most common implementation, only a sinusoid phase modulation is needed in order to allow for reconstruction of the complex electric field [131].

Another systematic approach for searching optimal phase by a sophisticated algorithm has evolved with phase-resolved interferometric spectral modulation (PRISM) [90]. This method is shown in Fig. 2.9(a), in which the pixels of the pulse shaper are not modulated randomly, but put into random groups. The phase of the pixels is systematically scanned one group at a time. The Fourier transform of the collected signal of each pixel allows for identification of the contribution from each individual pixel. This identification is possible since each pixel is assigned a unique phase modulation frequency. By maximization of the nonlinear feedback from each pixel, the optimum phase for the first group of pixels is found. The same procedure is then repeated for the other groups. Since no assumptions have to be made on the phase, also complicated phase patterns, e.g. containing phase jumps, can be reconstructed. These advantages led to the PRISM algorithm being selected for pulse compression done in the scope of this work. By using more than one iteration, a refined result can be obtained. In the case presented in Fig. 2.9(b), two iterations have been made using 4×40 steps (black and red lines) by binning the pulse-shaper pixels in groups of 4. Two additional iterations without binning, i.e., 4×160 steps, refined the result (green and blue lines). As described above, the pulse shaper used here is capable of introducing up to -5000 fs^2/rad of negative dispersion, which is enough to compensate for all dispersive elements between light source and sample, including the microscope objective (2800 fs^2/rad by itself).

Where possible, reflective or thin dispersive elements were used to ease compensation by the pulse shaper, e.g. pulse-shaper gratings with 1 mm thickness and linear polarizer with about 200 μm thickness. Although a major fraction of the shaping window can be used for solely compressing the laser pulses with the pulse shaper, additional pre-compression by chirped mirrors was used. This way, a larger part of the shaping window

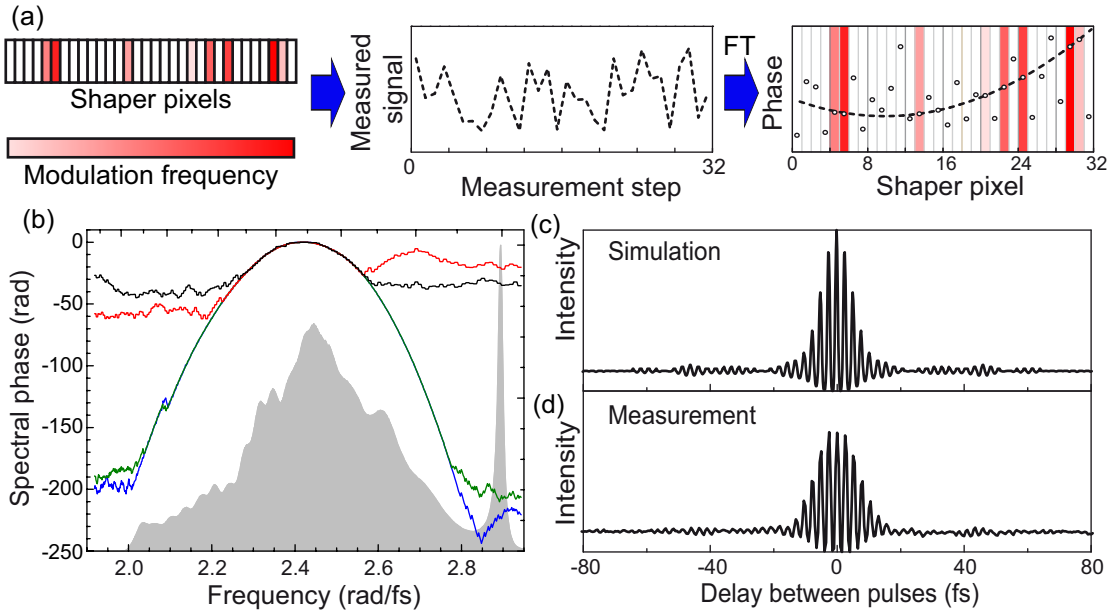

Figure 2.9 | Chirp compensation with the PRISM algorithm. (a) The phase of a fraction of the pulse-shaper pixels is modulated with a frequency unique to each pixel (upper left). The integrated intensity is recorded involving a nonlinear process to access phase information (upper center). By Fourier transformation, the information is decomposed into the contribution of the individual pixels. The phase (circles) of the modulated pixels (red) can thereby be set to the optimum compression phase (dashed line). The remaining pixels are modulated in groups to yield a compression phase over the whole spectrum. (b) Retrieved spectral phase after PRISM iteration one (black), two (red), three (green), and four (blue). By comparing a simulated quadratic autocorrelation using the experimental spectrum [grey in (b)] and a flat spectral phase (c) with a measured trace (d), the successful compression to a pulse duration of below 10 fs (FWHM) could be confirmed. Figure adapted and modified from Ref. [3].

was reserved for additional pulse modification, e.g. the generation of pulse sequences for spectroscopy.

As described in the following section, the approach for pulse compression presented above allows for sub-10-fs laser pulses, also in the focus of the microscope objective. Before the results are shown, the additional precautions needed when desiring pulse compression in a small focus are discussed.

2.9.6 Pulse compression in the microscope

The compression methods described in the previous section in principle also work in a tight laser focus. However, some adaptions may be necessary. An intrinsic advantage of the highly confined fields is a higher relative yield of the nonlinear processes, potentially improving the signal-to-noise ratio and reducing the necessary acquisition time.

On the other hand, when compressing a broadband laser pulse in the focus of an immersion oil microscope objective, the use of nonlinear crystals is far from trivial. The crystal needs to be very thin (in the range of 10 μm) to allow for phase matching over the whole spectral range and placed on top of a thin glass substrate, typically of 170 μm thickness. A convenient alternative to the crystal sheet is using a grinded nonlinear

medium on the surface of a glass substrate in the form of micrometer- or nanometer-sized powder, therefore intrinsically achieve full phase matching. It has been shown that pulse compression is possible with this method using nonlinear crystals for generation of higher-order feedback, e.g. $Fe(IO_3)_3$ and $BaTiO_3$ as described above, can also be utilized in the shape of nanocrystals [92]. When utilizing the nonlinearity from a single nanocrystal, sub-micrometer spatial resolution has been demonstrated [57, 132, 133]. One problem arising with methods like FROG and MIIPS is that light from SHG has to be collected. As common microscope objectives do not effectively transmit broadband UV-VIS light, a workaround could involve collecting the light in transmission direction with an UV objective.

Furthermore, the sensitivity of the detection is reduced by losses when collecting the nonlinear signal either in reflection or in transmission and by the separation of fundamental and nonlinear contributions. On top, using a spectrally resolved detection, the necessary distribution onto an array of detector pixels imposes further hurdles by decreasing the signal-to-noise ratio.

In the work presented here, using nanocrystals has proven impractical because of the low damage threshold of the crystals which hinders compensating the low nonlinear yield by increasing the pulse energy. At 80 MHz repetition rate, the low pulse energy makes it necessary to use high average powers for an adequate nonlinear optical sample response, measuring the pulse length at a single diffraction-limited area on a surface is challenging. Instead of the collinear SHG FROG trace, one can measure the spectrally integrated trace, effectively a collinear autocorrelation. A major remaining experimental difficulty is the bleaching stability of the nonlinear crystal powder which limits the signal strength to problematic levels even with spectrally integrated detection. These challenges can be avoided when exploiting a different nonlinear process, i.e., by measuring the integrated signal directly in focus. As discussed in Section 2.9.4, one possibility is to use a TPPD which can be placed in the microscope focus. A suitable diode (G5645, Hamamatsu) was placed in oil in the focused beam of the microscope objective. Due to the short working distance of the objective, a diode without casing hat was used to bring the diode surface closer to the focus. In later applications of the pulse compression, a diode without the protective polymer layer on the surface of the active diode area was used to decrease this distance even further. Both experimental realizations, with and without the polymer coating, were used on the assumption that the remaining distance between active area of the TPPD chip and the focus are small enough to add only negligible amounts of additional dispersion to the reconstruction.

The amplified TPPD response could further be refined by using lock-in detection. The spectral phase was optimized with the PRISM algorithm [90, 134, 135], which was conducted in four iterations with the 640 pixel SLM-based pulse shaper. As described in the previous section, the pixels were randomly divided into four groups. The groups were scanned consecutively according to the algorithm, meanwhile leaving the phase of three inactive groups unchanged. To achieve a fast approximation, every four consecutive pulse shaper pixels were binned to obtain only 160 effective pixels in the first two iterations, taking less than 10 min each. Two additional iterations, each with a duration of 35 min, were done without binning to achieve a refined reconstruction of the spectral phase.

After the pulse compression, the inverse of the reconstructed phase [blue curve in Fig. 2.9(b)] was applied to the pulse shaper. A characterization by interferometric

collinear quadratic autocorrelation was done by conducting a pulse-shaper assisted double pulse scan. Figure 2.9(d) shows the recorded feedback, using the same TPPD as was previously used for PRISM. The theoretical intensity ratio of 8:1 between full temporal overlap at $\tau = 0$ fs and complete temporal separation of the two pulses could not be observed. This was attributed to saturation effects in the diode at the center of the tightly focused beam. Please note that the full spectral phase of the compressed laser pulse is not retrieved by the interferometric autocorrelation (iAC). Instead, the iAC is numerically calculated assuming the experimental spectral intensity and a flat phase [see Fig. 2.9(c)]. The close resemblance between the measured and the calculated autocorrelation traces confirms the success of the PRISM algorithm in temporally compressing the laser pulse. The measured pulse duration retrieved from the autocorrelation is 9.3 fs, close to the Fourier limit of 7.6 fs. Determination of the pulse duration was done by Fourier filtering out the oscillating component and taking the FWHM of a Gaussian fit from the non-oscillating curve. In addition, a FROG trace was also measured through SHG from nanocrystals (Barium titanate(IV) nanopowder, 467634-25G, Sigma Aldrich), using a lens on top of the microscope to collect the light and spectral filtering of the second harmonic. The signal-to-noise ratio has proven not good enough for field retrieval over the full spectral range. Trying to raise the nonlinear feedback by increased pulse power to increase SHG yield led to damage of the crystals, making the acquisition of a full FROG trace from a single nanocrystal impossible.

2.10 The shape of the focus

2.10.1 Nanorod measurements

When investigating nanostructures with feature sizes in the order of the laser focus, the spatial dependence of the laser spectrum becomes crucial in addition to the temporal profile. A spatial chirp in the focus plane not only leads to a decreased peak intensity and an increased pulse duration but also to a position-dependent effective spectrum which can have devastating impact onto the result of the experiment. The microscope objective itself needs to be carefully selected according to the requirements of broadband ultrafast spectroscopy. Chromatic aberration, spherical aberration and other deviations need to be corrected well over the used spectral range, as described in Section 2.5.

To assure the functionality of the microscope arrangement, information on the spatial beam profile in the focus is needed. Although it is possible to modulate the beam propagation using ray-tracing calculations, one would need exact knowledge of the optical setup. Apart from the difficulties of acquiring this information, an experimental determination is also desirable to investigate the interaction of the optical components. Existing studies have investigated pulse-front-distortion and comparing microscope objectives [136, 137], but merely measured in the collimated beam after passing the objective twice.

A more direct characterization can be done by direct beam characterization in the laser focus. Existing methods include a modification of spatially encoded arrangement for temporal analysis by dispersing a pair of light E-fields (SEA TADPOLE) [138], where a single-mode fiber is scanned through the focus. By measuring the interference between the collected light and a known reference pulse, the full information of the electric field is

retrieved by spectral interference. The achieved spatial resolution was given by the fiber diameter of 5.6μm, and was further increased by exchanging the fiber with a near-field scanning optical microscopy (NSOM) tip [139]. In the scope of this work, a different, all-optical approach was pursued: The scattered light from a nanoparticle, scanned through the focus volume, was analyzed. It allows a systematic retrieval of the full electrical field of the tree-dimensional focus structure.

Nanoparticles have already been used to investigate the impact of space–time coupling on the laser focus [140] to gain qualitative information about a pump-probe fluorescence signal when placing nanoparticles at different positions within focus. By using nanoparticles as probes, spherical deviations can be measured and by variation of the microscope incoupling, the chromatic aberration can be minimized. This corresponds to the optimum of incoupling position and direction, i.e., a centered incoupling along the optical axis of the objective. In the work described here, a sub-focus sized off-resonant nanoparticle was scanned through the focus plane and acted as a position-dependent probe for the effective spectrum. The nano-scatterer only probed part of the focus due to its small size relative to the light cone. Commercially available gold nanorods were used (Nanopartz), specified to have a length of 34 nm and a 25 nm diameter, resulting in a resonance at 550 nm wavelength. The principle of this method is similar to SEA TADPOLE [139], though the nanoparticle probe offered a superior resolution compared to a single-mode fiber or a NSOM tip. The nanorods were distributed on a microscope cover slip. Localization of individual rods was done with the help of a chromium marker structure. By comparison with previously obtained scanning electron microscopy (SEM) images, the location of single nanorods instead of clusters was assured. To oppress the reflection from the glass-air interface, the nanorods were covered with immersion oil. The measurement was repeated on different nanorods to investigate the possible influence of nanorod orientation. The measurements were conducted in the linear regime at low powers, approximately 60 μW in this case. Nevertheless, a good signal-to-noise ratio was achieved. Increasing the pulse energy by one order of magnitude resulted in no nanorod damage, confirming their adequate stability.

In the first step of the incoupling optimization, the pulse shaper was bypassed, allowing straight forward attribution of spatial chirp in the microscope focus to misalignment inside the microscope setup. The gold nanorod was scanned through the xy-plane of the focus [depicted in Fig. 2.10(b)] in 40 nm steps while collecting the reflection spectra at each point with the 2D spectrometer [spectrograph (Acton SpectraPro 2500i, Princeton Instruments) and CCD (e2v, CCD42-10 in Acton Pixis2kB, Princeton Instruments)]. In the measured configuration, the x-direction was parallel to the linear beam polarization and, when included into the beam path, also parallel to pulse-shaper spectral axis. Looking at the integrated intensity, a small focus spot can be seen [Fig. 2.10(b)]. It has to be noted that spatial chirp would not be visible in this figure to a certain degree since it would be indistinguishable from an elongated focus shape. The integrated measurement already indicates an overall focus diameter of below 300 nm (FWHM). Spatial chirp was further investigated from the spectrally resolved reflection intensity seen in Fig. 2.10(c) for the full spectral bandwidth of the laser of nearly 300 nm. As expected, the focus size increases with increasing wavelength. The spectral focus position variations are depicted by the solid red line in Fig. 2.10(c). They were obtained by individual fitting of two-dimensional Gaussians on the intensity distributions of each spectral component. When

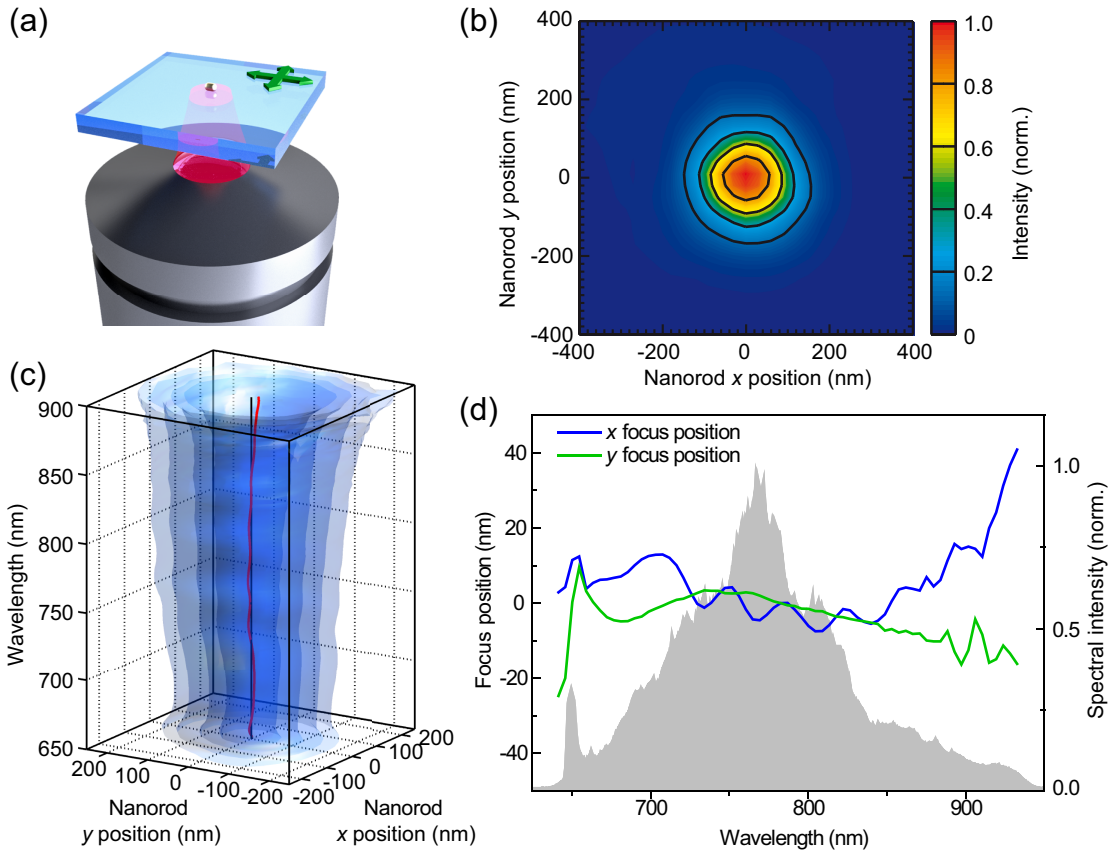

Figure 2.10 | Spatial mapping of the spectral intensity through the focus of the microscope objective with a nanorod scatterer. (a) Sketch of the gold nanorod on the surface of a glass plate in the focus of the objective. (b) Spectrally integrated mapping of the light scattered back in dependence of the nanorod position. The same information is spectrally resolved in (c), depicting the regions containing more than $6/e^2$, $4/e^2$, $2/e^2$, and $1/e^2$ of the maximal intensity for each wavelength by the blue contours. The wavelength-dependent center of the focus is depicted by the red curve, compared to the overall center position marked by the blue line. (d) Decomposition of the wavelength-dependent focus position onto the x-direction (blue curve) and the y-direction (green curve). The normalized spectral intensity is shown for comparison. Figure adapted from Ref. [3].

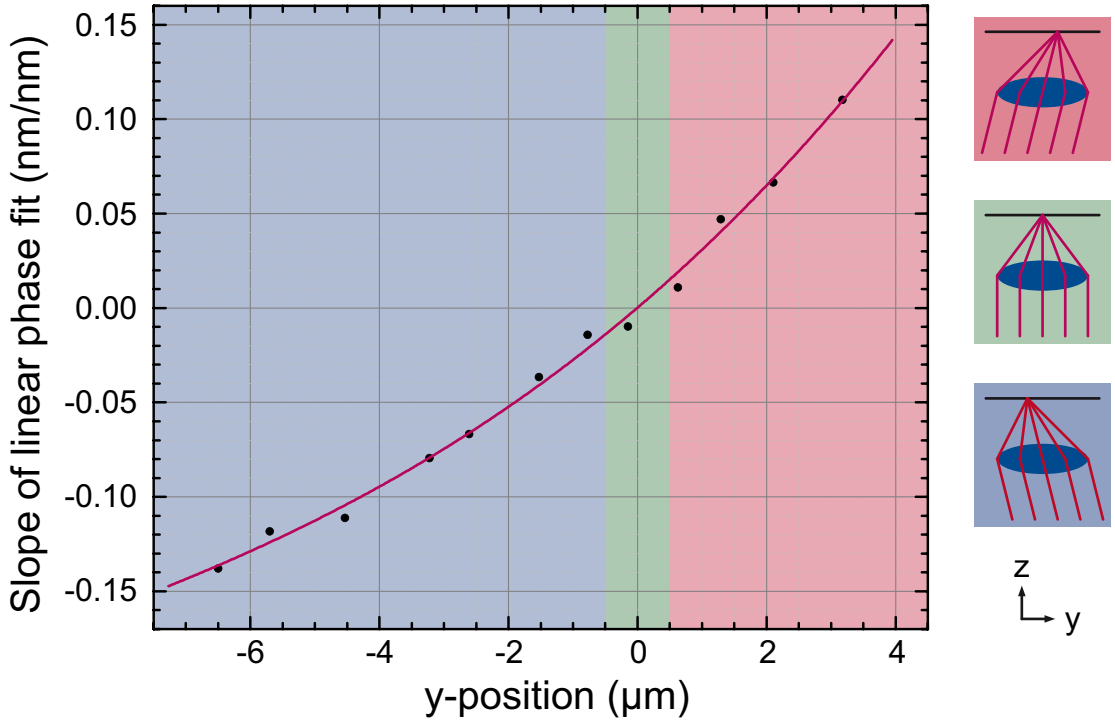

Figure 2.11 | Dependence between the spatial chirp in the image plane and the microscope incoupling. In the optimal situation sketched with green background on the right-hand side, spatial chirp is minimized by the objective design. Deviations in the direction of the beam incident on the microscope back-aperture lead to a change in the focus positions, as demonstrated by the red and blue box on the right-hand side for the y-direction. On the left-hand side, the linear fits to the spatial chirp, experimentally retrieved by scans of a nano-scatterer, are shown in relation to the focus-position in y-direction (black spheres). From a cubic fit to the data (red curve), the position with vanishing spatial chirp is identified.

compared to the integrated center marked by the solid black line, it can be seen that the deviations are small compared to focus size. The latter is depicted by the blue three-dimensional (3D) contours marking $6/e^2$, $4/e^2$, $2/e^2$, and $1/e^2$ of the maximal intensity for each wavelength. To take a closer look at the wavelength-dependent focus position, Fig. 2.10(d) shows their projections on the x and the y direction for wavelengths between 700 nm and 850 nm, the spectral region where most of the intensity was distributed. The focus position deviation was lower than 10 nm from the center wavelength focus position in the region of significant spectral intensity.

As mentioned above, the described measurements were taken without the pulse shaper included in beam path. In conclusion, the deviations have to come from the laser output, or the remaining optics towards the sample. Possible reasons include the influence of chirped mirrors and imperfect incoupling into the microscope objective. The oscillations along the x-direction of the focus position were attributed to the former. Linear or higher-order slopes of the spectral focus-position dependence however correlate with changes in the incoupling, which has already been optimized prior to the measurements shown above in Fig. 2.10. As can be seen in the illustrations on the right-hand side of Fig. 2.11, a change in the incoupling angle on the backside of the microscope objective results in a change in the beam position inside the focal plane, in this case in the y-

direction. Since the optimization of the aberration correction contributing to the design of the microscope objective is primarily done for incoupling along the optical axis, the spectral irregularities of the focus position are expected to increase when the incoupling angle is tilted away from the axis.

To ensure a precise incoupling along the optical axis, a direct incoupling angle alignment was done for coarse adjustment. The pattern of the focus in an image plane after passing a second linear polarizer in the detection path could be mapped onto a screen or camera [82]. A regular pattern indicates correct incoupling, in contrast to an asymmetrical spatial intensity distribution hinting at misalignment. The irregularities are more pronounced when the interface from which the reflection stems is slightly out of focus, where a defocus of about 1 μm proved to be effective in the present setup.

The spatial focus pattern optimization is only the first part of a two-step alignment process, since the precision needed here can only be achieved with a sophisticated tool for fine-adjustment. The presented nanorod intensity measurement has proven to be a time-consuming but effective method for fine-tuning. From the spectrally resolved spatial intensity distribution, the slope of the spectral dependence was measured and fitted for different focus positions and therefore incoupling angles in both the x and the y direction. The result can be seen on the left-hand side of Fig. 2.11 for the y-direction, indicating the correlation. From these measurements, the incoupling angle resulting in a minimal slope and therefore minimal spectral dependence of the incoupling position was found inside the xy-plane, corresponding to incoupling along the optical axis of the microscope objective.

The remaining deviations on the order of 10 nm, mainly the wavelength-dependent oscillations seen in Fig. 2.10(d), are large compared to the size of the nanorod, but small compared to the beam focus having a diameter slightly below 300 nm (FWHM). The intensity deviations of a 10 nm shift are 0.5 % at beam center and 8 % at the position of the steepest slope of Gaussian spatial intensity distribution, fluctuations too small to introduce detrimental spectral deviations in experiments. The origin of the oscillations in x-direction is likely to be found in Fabry-Pérot-type reflections inside the pulse-shaper LCD, which are addressed below in Section 2.12.3. Due to its time-consuming nature (roughly 200 individual positions for each spatial map), the fine-adjustment by the nanorod method were only done when changes to the setup were made. This has proven to be sufficient to minimize spatial deviation of the wavelength-dependent focus position.

A question remaining is if this diligent optimization also results in a homogeneous pulse arrival time in the focal plane, which can also be investigated by nanorod reflection measurements as described in the following. More precisely, when the reflected beam is overlapped with a reference beam not passing the objective and sample, the retrieval of the spatial spectral phase dependence inside the focus volume is accessible by nanorod scatterer measurements, in addition to spectral amplitude distribution. The first order of this dependence is the spatial distribution of the pulse arrival time, which can therefore be measured by spectral interference.

The result is depicted in Fig. 2.12, showing the pulse arrival time relative to beam center with sub-diffraction resolution and thereby the radial chirp of the microscope objective. For a quantitative analysis, it has to be taken into account that light passes the objective twice. With the assumption that the introduced distortions are independent from the direction the light passes the objective, the measured arrival time deviations

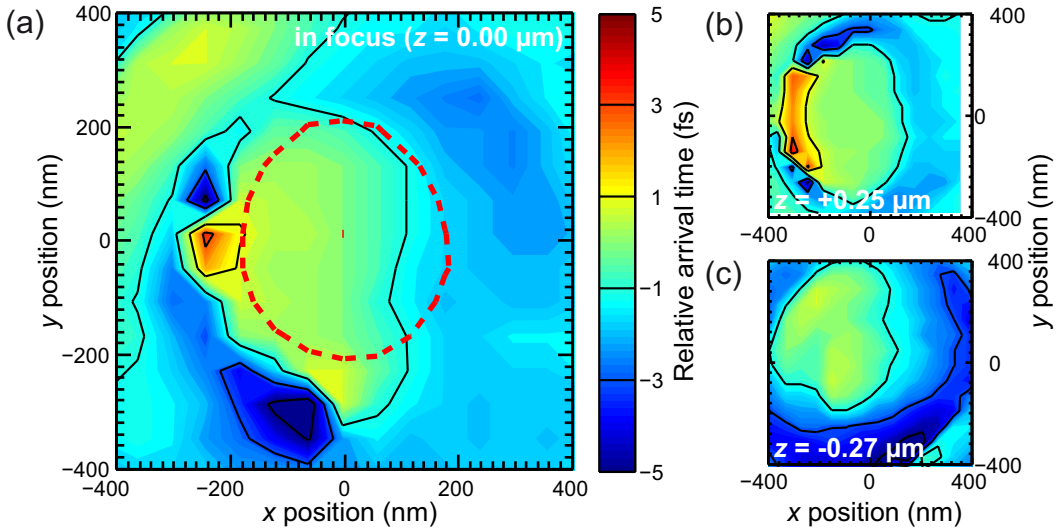

Figure 2.12 | Pulse-arrival-time variation in the microscope focus. (a) Measurement in the focal plane. Color-coded is the arrival-time relative to the center of the focus. The area of the focus is distinguished by the red dashed line. Pulse-arrival-time variations increase when mapping a plane above [(b) for z=+0.25 μm] or below [(c) for z=-0.27 μm] the focal plane of the objective. Figure adapted from Ref. [3].

are divided by 2. The red dashed line depicts the positions corresponding to $1/e^2$ of the maximum intensity. Inside these borders, the deviation of the arrival time is on the order of 1 fs. Prior measurements of the arrival time deviations showed that this minimal residue of spatial chirp can only be achieved by prior incoupling optimization with high precision.

In addition, if parts of the beam that travel through the objective near the optical axis traverse through different amounts of dispersive media than the parts from the rims of the spatial beam profile, the focused laser pulse will be inevitably stretched, an effect that has to be minimized.

To sum up, the investigation showed a strong wavelength position dependence of the focus position for incoupling angle misalignment, which has to be adequately minimized by suitable highly sensitive methods. With the help of nanorods scanned through the focal plane of the microscope objective, the focal shape was mapped and compared for variation in the incoupling angle on the objective backside.

When including the pulse shaper into the beam path after microscope incoupling optimization, one can be sure that additionally introduced deviations are due to the pulse shaper. Pulse-shaper-induced deviations are present even for a perfectly aligned $4f$ setup. In addition, the spatial beam profile is dependent on the temporal pulse shape due to space–time coupling. In addition, the cylindrical mirrors used to focus onto the LCD array (see Fig. 2.1) introduce spherical aberration (as would cylindrical lenses), i.e. the effective focal length depends on distance from the optical axis.

In the configuration used here, the beams inside the $4f$ setup are not arranged in a plane. The incoupling mirror in front of the first grating is slightly tilted upwards, resulting in a beam propagation upwards to the cylindrical mirror at an angle of less than 3°. This tilt results in a vertical displacement of wavelengths on the edges of

the spectrum in the output beam. In an alternative configuration, all beams would propagate in one plane, but the cylindrical mirrors would have to be hit from the side, i.e. off-axis, which would result in chromatic aberrations. Ray-tracing with the Optica package of the software Mathematica indicated that the aberrations from vertical tilt have a smaller impact on the overall spatial beam quality, which is why this design was realized.

When considering the cylindrical mirrors, a higher focal length results in a small angle and thereby in smaller deviations. On the downside, the beam waist increases with the focal length, which limits the shaper resolution and increases the influence on the output beam profile [141]. A telescope in front of the pulse shaper expands the beam profile to 7 mm diameter ($1/e^2$). With the 300 mm focal length of the cylindrical mirrors, this results in a beam diameter of 45 μm in the Fourier plane for a single spectral component, denoting a compromise between a low incident angle and a focus size sufficient small to stay below the pixel width of the used LCD (100 μm). The latter ensures that the spectral resolution is mainly limited by the amount of pulse shaper pixels and not further reduced by mapping a single spectral component onto multiple pixels.

As described in Section 2.8, the single-pass arrangement is not the only possibility. An alternative arrangement constitutes of a mirror after the second grating, resulting in the whole pulse shaper being passed twice. After the second pass, the incident and the outgoing beam are separated by a beamsplitter or a pick-of mirror if the folding mirror introduces an additional vertical displacement. As analyzed by Wefers and Coworkers [142], the double-pass cancels space–time coupling for simple pulse shapes. The cancellation is confirmed in Ref. [143] but as Ref. [140] proposes, the higher-order terms of space–time coupling remain. In addition, the double-pass arrangement doubles loss and distortions of $4f$ configuration. These considerations, together with the demonstration of the feasibility by the nanorod measurements discussed above, justify the use of the single-pass configuration for the experiments in this work.

2.10.2 Influence of phase masks and phase-and-amplitude masks

To investigate the influence of phase masks, a variable linear phase is introduced to shift pulse in time domain. In addition, a constant offset phase obtained by the PRISM algorithm for temporal pulse compression in the focal plane is applied, which introduces a high amount of phase jumps on the phase mask whose exact spectral positions are dependent on the additionally applied linear phase. Thereby both the influence of the linear phase and of 2π phase jumps are investigated. Figure 2.13 shows the wavelength-dependent focus position for -200 fs, 0 fs and $+200$ fs linear phase. To minimize the influence of drifts which lead to an accuracy of repeatability of 5 nm, for each spatial position, the three delays were measured in direct succession (in contrast to measuring all positions for a delay time directly after each other).

The measurement indicates that the wavelength-dependent focus positions for x-direction [Fig.2.13(a)] and y-direction [Fig.2.13(b)] show slightly higher variations than for the case without pulse shaper (as can be compared with Fig. 2.10). The steep slopes at the edges of the spectrum are attributed to the influence of the $4f$ telescope, since the cylindrical mirrors introduce spherical aberrations despite the geometry optimization described above.

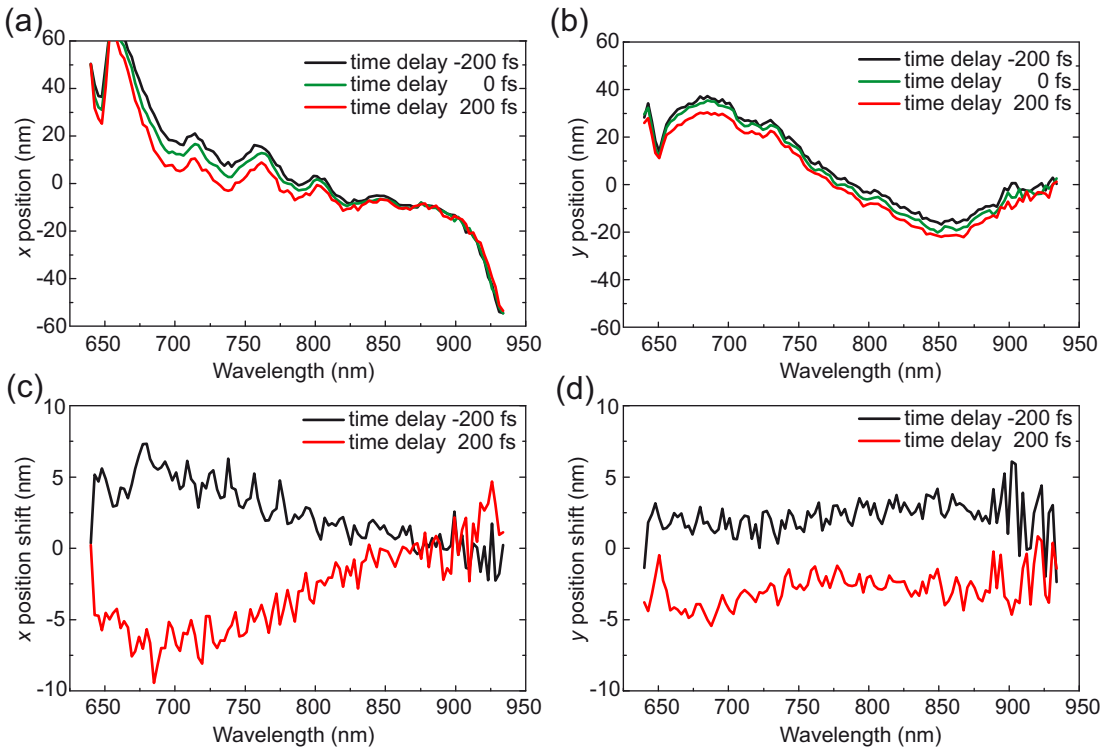

Figure 2.13 | Dependence between the spatial chirp in the focal plane of the objective and linear phase applied by the pulse shaper. The variations are shown for time delays −200 fs (black), 0 fs (green), and +200 fs (red) (a) in x-direction and (b) in y-direction. The relative difference to 0 fs time-delay is plotted (c) for the x-direction and (d) for the y-direction, respectively. Figure adapted and modified from Ref. [3].

In addition, the measurement unveils systematic differences in dependence of the delay time. Those can be seen more clearly in Figs. 2.13(c,d), in which the deviations from a 0-fs-delay pulse are plotted for the x-direction and the y-direction. No further alignment or other changes were done in between the measurements, which means that the delay-dependent changes can directly be attributed to phase-time coupling. The latter postulates a dependency between the spatial beam pointing and the applied pulse shape, which is described below in Section 2.12.4. The influence is on the order of 5 nm and thereby small compared to the focus size.

To compare the arrival times, separate measurements were conducted. The results closely resemble the previous case described above, where no pulse shaper was included into the beam path, which means that the deviations most likely originate from the microscope objective.

The same measurements of the wavelength-dependent focus position were repeated for different delay times and without applying PRISM compression phase, yielding results similar to the presented measurements for the compressed pulse. At larger delay times of ±1 ps and ±2 ps, the maximal shift of the focus position is 15 nm when compared to the 0-fs-delay pulse, as can be seen in Fig. 2.14. Frei and coworkers argue that there is no effect of space–time coupling directly in the focal plane when only the spectral phase is modulated [144]. Other groups claim that the effect vanishes at the geometrical focus position rather that at the beam waist minimum [141, 145].

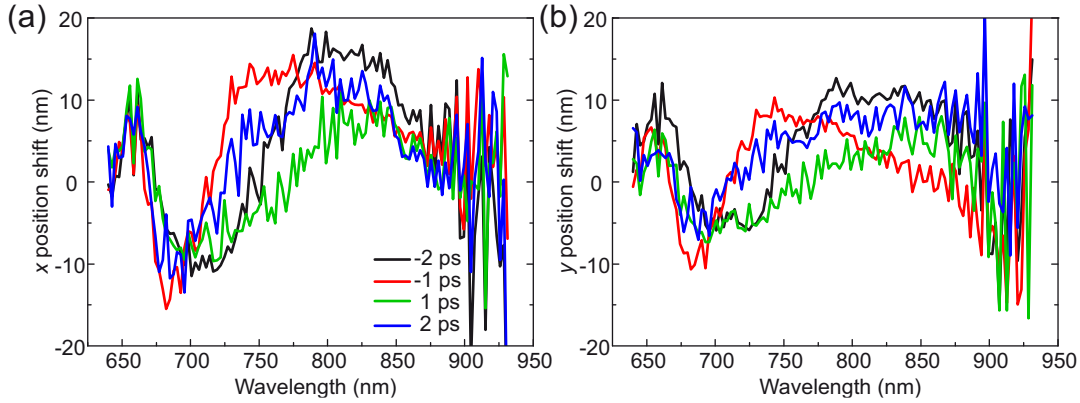

Figure 2.14 | Changes of the spatial chirp in the focal plane of the objective for high amounts of linear phase. The relative deviation from a delay of 0 ps is shown for delays of −2 ps (black), −1 ps (red), 1 ps (green), and 2 ps (blue) as shift (a) in x-direction and (b) in y-direction. Figure adapted and modified from Ref. [3].

With the nanorod-method presented above, the influence of phase-only mask is investigated more systematically. The fact that increasing the delay by one order of magnitude only triples the focus position shift hints that the deviations are the result of multiple interacting artifacts, which makes it hard to predict the overall influence. The deviations have proven not to be proportional to the linear phase, but instead seems to run into saturation. This result complements earlier observations acquired for collimated beams [144]. Only the linear phase influences were investigated here, but higher order phase influences can be approximated locally by sections of linear dependence. Therefore, similar effects are to be expected.

Apart from phase-only modulation, the influence of phase-and-amplitude modulation was investigated in addition. Such modulations are of high practical relevance since they are needed for creating common pulse shapes used in spectroscopy and coherent control. For example, pairs of pulses with varying delay τ require periodic amplitude masks in addition to phase modulation. One fundamental advantage of double pulses created in a pulse shaper compared to an interferometer is the inherent phase stability and full pulse overlap. However, the latter only holds when neglecting space–time coupling.

To investigate the influence of space–time coupling on the wavelength-dependent focus position for a pair of double pulses generated by the pulse shaper, Fig. 2.15 shows the results for inter-pulse delays of 100 fs and 400 fs. For comparison, the intensity patterns are additionally plotted in grey. They show the measured intensity relative to that of a single pulse, i.e., for full transmission. Periodic distortions of the wavelength-dependent focus position are visible and show the largest deviations for the lowest transmission. If a slight spatial displacement between the two pulses is existent, the pulses potentially have different propagation paths through the objective lens. For the 400 fs delay, the spatial dependence of the inter-pulse delay was measured. The deviations from the intended delay are plotted in Fig. 2.16. As can be seen, the variation of the temporal separation between the two pulses across the focus are below 1 fs, i.e., they are small compared to the pulse duration.

To sum up, measurements of the pulse arrival time and the wavelength-dependent focus position in the focus of a high-NA microscope objective with gold nanorods as

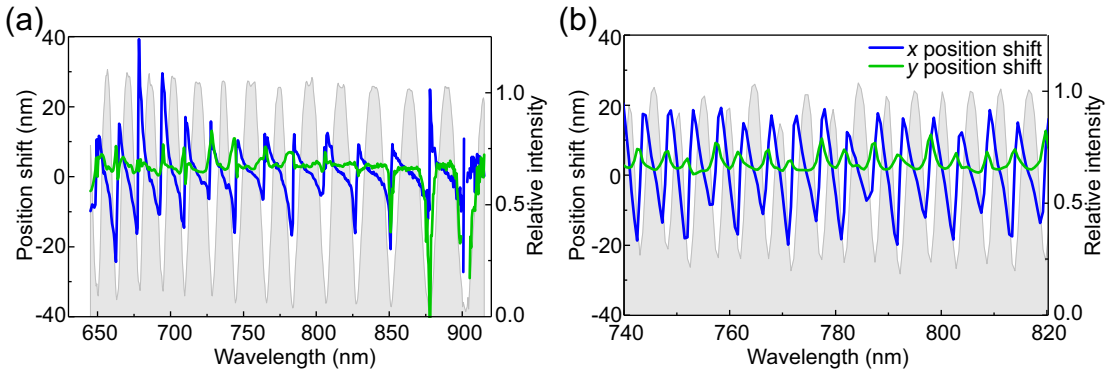

Figure 2.15 | Spectrally dependent focus-position variation for double pulses separated by (a) 100 fs and (b) 400 fs. A periodic position deviation is observed both in x-direction (blue) and y-direction (green). A correlation of the position deviations to the intensity modulation can be seen in the spectra of the double pulses (in grey, normalized to a single-pulse spectrum). Figure adapted and modified from Ref. [3].

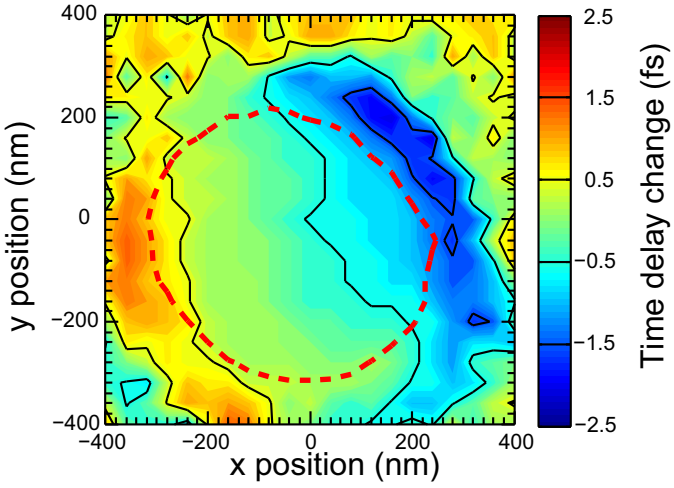

Figure 2.16 | Spatial variation of the 400 fs inter-pulse delay of a pulse pair. The time-delay change is below ±1 fs for the focus confined within the red dashed line depicting $1/e^2$ of the maximal intensity. Figure adapted and modified from Ref. [3].

probe were demonstrated. The incoupling into the microscope objective was optimized by minimizing spatial chirp in the focal plane. With the help of the pulse-shaper-based PRISM algorithm, the laser pulses were compressed to below 10 fs. The subsequent investigation of the pulse-shaper-induced influence on the temporal and the spectral shape of pulse in the focus proved the existence of deviations in all measurements. However, the deviations have proven to be of magnitudes that do not influence the outcome of typical experiments in a perceptible manner.

As a next step, an insight into the systematic characterization and correction of pulse shaper artifacts shall be given in the following section, giving raise to further improvements of the temporal and spectral shape of the microscope objective focus.

2.11 Pulse shaper calibration

One of the key prerequisites for optimal pulse shaper functionality is a precise calibration, so that the desired phase change in an LCD pixel can correctly be applied by changing the voltage between the two electrodes enclosing the liquid crystal layer. This has been described in various publications [102, 107, 116]. Nevertheless, it shall be discussed here for the experimental setup used in this work to allow for explanation of the pulse-shaper artifact corrections presented in Section 2.13 below.

In general, a two-layer LCD-based pulse shaper can be used to modulate the transmission $T(x, U_1, U_2)$ and the phase $\Phi(x, U_1, U_2)$ for each pixel x of the LCD array, depending on the individual voltages applied to the LCD layers 1 (U_1) and 2 (U_2). The LCD used here is operated in the "low-voltage mode" with a range of 3 V. This range is addressed individually for each pixel in 4096 levels, resulting in a step size of 732 μV, simply called (voltage) steps in the following. A straight-forward approach of measuring the whole range of the pulse-shaper response could involve spectral interference with an unshaped (and independently characterized) reference pulse. Apart from the potential inaccuracy of phase and amplitude reconstruction, the duration of the measurement renders this method impractical. For the pulse shaper used in this work, the duration can be estimated to be 388 days, assuming 1 s for application of the pulse shape to the LCD, the same duration for data acquisition on a spectrometer and 16 Million voltage step combinations (U_1 and U_2, 4096 steps each). In addition, handling this data all at once would require memory on the order of 10 TB with the evaluation presented below. This would result in impractical split-up of the data in many small pieces for realistic computing capabilities. A reduction of the acquired data by reducing the measured voltage steps, either by even reduction or by sparse sampling [146, 147], could of course reduce or even solve the problems. This introduces additional issues with interpolating the data for a complete calibration and does not solve the delicate signal reconstruction by spectral interference.

If one assumes the independence of the voltages and thereby phases applied to each of the two layers, the amount of required data can be drastically reduced. For each layer, only one voltage scan is required while the voltage of the other layer is kept constant. This voltage scan can be conducted without the need for phase retrieval, since the knowledge of $T(x, U_1, U_2 = \text{const})$ and $T(x, U_1 = \text{const}, U_2)$ is sufficient to calculate the individual phases applied to each pixel of each layer, as can be seen from

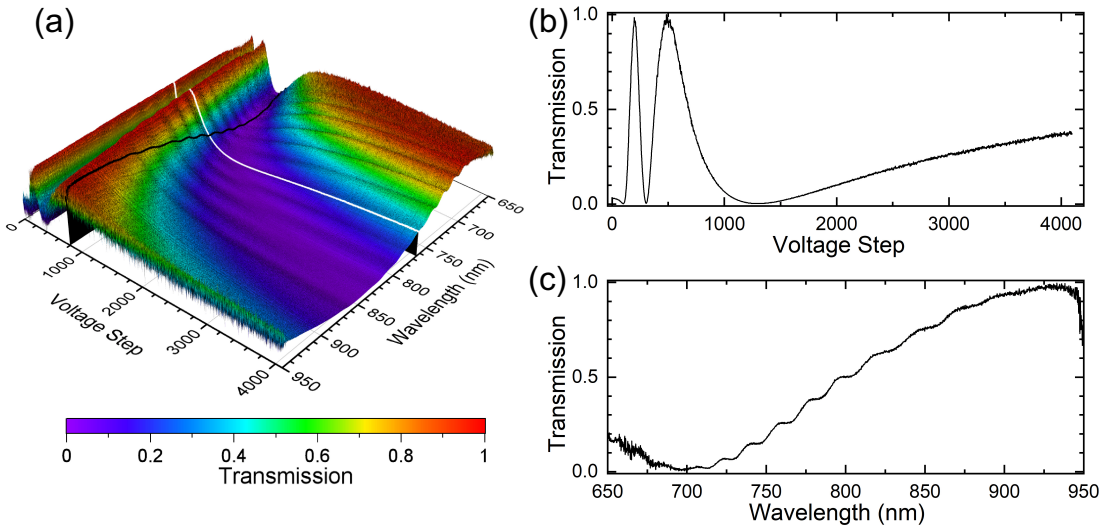

Figure 2.17 | Raw data of the voltage-dependent transmission curve $T(x, U_1, U_2 = 200)$ used to create the phase-to-voltage calibration. (a) Full data set with color-coded transmission height map normalized to each spectral component. Noise is mainly visible at the edges of the spectrum. The white curve marks a cut along a wavelength of 765 nm, close to the laser center wavelength, is separately plotted in (b). A cut along a constant voltage of 800 marked as the black curve in (a) and separately plotted in (c) clearly reveals oscillations most likely originating from Fabry-Pérot-type artifacts.

$$T\left(U_1, U_2\right) = \cos^2\left(\frac{\Phi_1\left(U_1\right) - \Phi_2\left(U_2\right)}{2}\right). \tag{2.5}$$

More specific, Equ. 2.5 shows that the overall transmission of a pulse shaper pixel is only dependent on the difference of the phases Φ_1 and Φ_2 induced by the two LCD layers [148]. If, e.g., the voltage U_2 and thereby the phase Φ_2 is kept constant, the dependency $\Phi_1\left(U_1\right)$ can be retrieved with knowledge of the transmission T from a scan of $T(x,U_1,U_2 = \text{const})$. Doing this for both layers, together with a wavelength calibration for each pixel $\lambda(x)$, the pulse shaper is fully characterized. Together with the transmission $T\left(U_1, U_2\right)$ defined in Equ. 2.5, the phase $\Phi\left(U_1, U_2\right)$ induced by a dual-layer pulse-shaper pixel is defined through

$$\Phi\left(U_1, U_2\right) = \frac{\Phi_1\left(U_1\right) + \Phi_2\left(U_2\right)}{2}. \tag{2.6}$$

The steps needed for such a characterization shall be presented now for the pulse shaper used in the scope of this work. The curves $T(x, U_1, U_2 = \text{const})$ and $T(x, U_1 = \text{const}, U_2)$ have to be retrieved first. The relative transmission from a voltage scan of layer 1, detected by a spectrometer, is shown in Fig. 2.17(a). The voltage for all pixels of layer 2 was kept constant at $U_2 = 200$. The data was taken for every odd voltage step U_1 to speed up acquisition and reduce memory usage in the evaluation software. It has to be noted that the wavelength axis is given by the spectrometer calibration and not

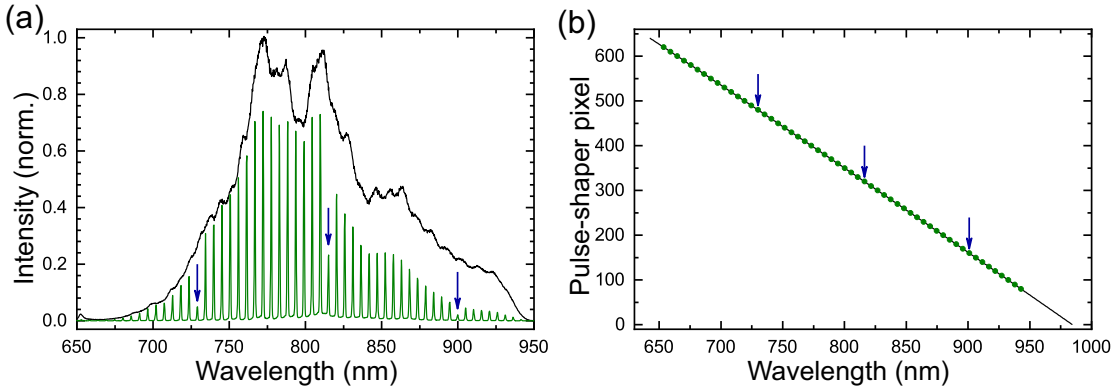

Figure 2.18 | Pulse-shaper wavelength calibration. By identification of voltages facilitating low and high transmission values, a transmission mask blocking all but every tenth pixels can be created. (a) The resulting pattern is plotted in green and spans the whole spectral range of the full spectrum plotted in black. The blue arrows mark three special pixels set to partial transmission, allowing for absolute localization of the pulse-shaper pixels relative to the laser spectrum. (b) The spectral position of the transmission peaks is mapped to the pulse-shaper pixels (green dots) considering the special pixels (marked by blue arrows). A quadratic fit (black solid curve) to the peak positions represents the final wavelength calibration.

yet linked to the pulse-shaper pixels by $\lambda(x)$. The intensity measured by every single spectrometer pixel is normalized. One of the resulting curves is plotted separately in Fig. 2.17(b), which was taken from the spectral region around the center wavelength of the laser spectrum. The exact position of the curve at $\lambda = 765$ nm is also depicted by the white curve in Fig. 2.17(a).

A cut along the wavelength axis at a constant voltage, as shown in Fig. 2.17(c) and by the black curve in Fig. 2.17(a) for $U_1 = 800$, reveals oscillatory transmission behavior. This can not be explained by the dispersive properties of the liquid crystal layer itself, but rather by a Fabry-Pérot-type effect closer discussed below in Section 2.12.3.

To determine the wavelength calibration of the pulse shaper, $\lambda(x)$, a phase pattern is created that sets the transmission to 1 for every 10th pixel and to 0 for all other pixels. The voltage combination $T(x, U_1, U_2)$ needed for both cases is estimated for all wavelengths from the transmission measurement plotted in Fig. 2.17(a). Figure 2.18(a) shows the transmitted spectrum when such a pulse shape is applied (green curve). When compared to the full spectrum (black curve), it is apparent that the transmission estimations were best for the blue part of the spectrum in this case, as the relative transmission of the green curve maxima are highest for this part of the spectrum. Nevertheless, clear transmission peaks are shaped over the whole spectral range of the laser and their exact spectral positions can be extracted. To allow for identification of unique peaks, three "special pixels" are defined at pixel 160, 320, and 480 with reduced transmission. They are easily recognized in the spectrum and marked with the blue arrows in Figs. 2.18(a,b). Figure 2.18(b) shows the maxima at the pixels x over their spectral position (green dots). The black solid line depicts the result of a quadratic fit of the peak positions, delivering an interpolated wavelength calibration between the detected peaks, but also extrapolated for the edges of the spectral shaping window. The latter is most notable for the red

part of the spectrum for wavelengths above 940 nm, outside the spectral region where light was detected.

With the help of the acquired wavelength calibration, an exemplary transmission curve for each pixel x of both layers is interpolated from the data shown in Fig. 2.17 for layer 1. For one full oscillation of the transmission curves along the voltage direction [compare to Fig. 2.17(b)], the phase introduced by the LCD layer changes by 2π. For the shown curve, e.g., a phase range of slightly above 4π can directly be estimated. After smoothing of the curves in voltage direction, the extrema values are extracted and the curves are split at these positions. For the individual pieces, defining a phase range of π each, the phase is calculated.

At this point, the phase calibration could, in principle, be used, since it now contains the phase curves for the spectral range where the laser has sufficient intensity. To gain a pulse-shaper calibration that is smooth over all pixels x and for all voltage steps, further refinement of the calibration surface is conducted.

As a first step, the voltage curves are individually evaluated. Curves that do clearly not show monotone behavior, mostly due to a high degree of relative noise, are sorted out. The remaining curves are smoothed in voltage direction. If they were not acquired for every single of the 4096 voltage steps, they are subsequently interpolated. Common measurement schemes involved every second step (as done in the data presented here) or taking 1024 steps over the whole span. The reduction of steps is justified by the fact that no phase oscillations on the length scale of a few voltage steps are expected from the LCD system.

Afterwards, the data is smoothed in wavelength direction and interpolated for pixels where data was previously sorted out due to high noise. For the edges of the spectral pulse-shaper range, the measurement does also not deliver reliable phase data, since the laser is spectrally narrower. One could argue that no calibration is needed for regions of negligible spectral intensity, which is, in principle, reasonable. Leaving all nonrelevant pixels at, e.g., $U_1 = U_2 = 0$ potentially leads to high voltage jumps between adjacent pixels in a single LCD layer. Previous investigations have shown that intra-layer voltage crosstalk of a few pixel range leads to phase and transmission deviations and should therefore be avoided where possible. In the case of the spectral edges, the problem can effectively be avoided by always setting the relevant pixels to the same voltage as the closest successfully calibrated pixel. This renders the calibration curve complete since now, the smoothed phase-to-voltage curves are defined for all pulse-shaper pixels and all voltage steps (640×4096 in this case), as can be seen for layer 1 in Fig. 2.19.

At last, a range of $n \cdot 2\pi$ of the phase curves is defined that is used for the actual pulse shaping. All phase masks (within the shaping window) that exceed this range are applied by back-folding the phase curve on the edge of the range, the so-called phase wrapping. The beginning of the range is set to be at the lowest voltages showing significant phase change. Here, the lower voltage limit was chosen to be $U_{1,\mathrm{min}} = U_{2,\mathrm{min}} = 120$ for all pixels, matching the given criterion as seen by the associated green curve in Fig. 2.19.

A phase range of 2π is depicted by the white line, which is set as upper voltage limit here. Using a range of 4π would drastically reduce the amount of necessary phase jumps, down to approximately half for complex pulse shapes. However, as apparent through the 4π-upper-voltage limit depicted in red in Fig. 2.19, the phase range is not sufficient for the red part of the spectrum due to the reduced dispersion of the liquid crystals. A

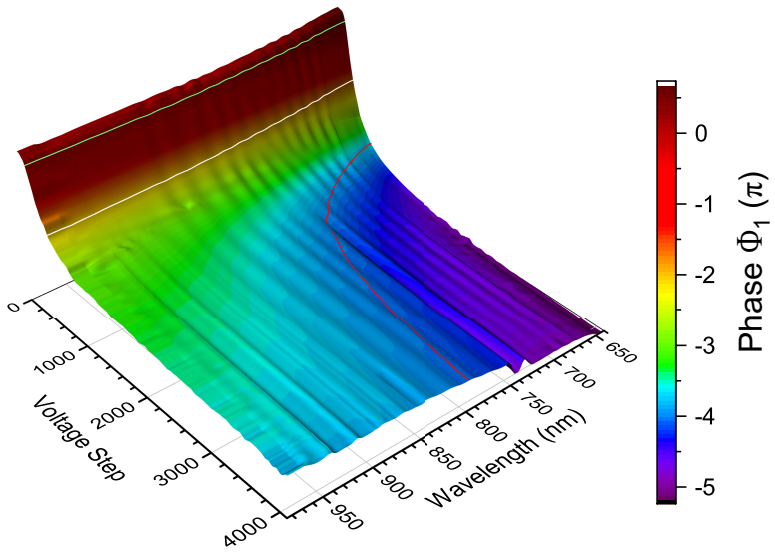

Figure 2.19 | The final phase-to-voltage calibration with color-coded height map depicting the induced phase of layer 1. The green line marks the lower voltage limit of the calibration at U_1=120. The final calibration uses a 2π phase-range with a pixel-dependent upper voltage limit marked by the white curve. Due to the increased dispersion of the liquid crystals on the blue part of the laser spectrum, a phase range of 4π can be scanned, marked by the red curve. The higher phase range is however not utilized to keep the full spectral bandwidth.

range exceeding 2π can thus only be used if the spectral range of the pulse shaper would be shifted to the blue, e.g. by tilting of the gratings, or simply by confining the laser spectrum to the blue part of the existing spectral range. A back-folding of the beam path, either directly after the LCD or after the full $4f$ layout, would also double the available phase range.

Here, the existing design is carefully adapted to the overall experimental setup used in this work and a spectral confinement of the laser spectrum, accompanied by the loss of temporal resolution, is not desirable. Therefore, the used phase range was set to 2π for all experiments conducted. In general, phase jumps do not influence the quality of the resulting pulse shape if one assumes a perfect pulse shaper without artifacts and aberrations, equipped with a flawless calibration. Therefore, an overview of pulse-shaper imperfections shall be given in the following section.

2.12 Pulse shaper imperfections

Deviations between the theoretical spectral and temporal shape of a laser pulse and the actual experimental result can be tracked down to a number of origins. On the hardware side, physical limitations or design flaws can influence the performance. Since some of them are inherent, they can lead to artifacts that also affect the measurements used for calibration. In general, pulse shaper artifacts are largely dependent on the used spectral

range, the geometry of the pulse shaper and the type, design and manufacturer of the LCD. Therefore, the impact of the artifacts and the need for countermeasures has to be evaluated for the individual experimental setup. The influence on the calibration procedure has to be kept in mind and reduced to a minimum by an adapted procedure or a belayed correction, as shall be discussed in the section below. Before that, general notes on the quality of the pulse shaper calibration and on the origins of artifacts are given.

2.12.1 The quality of the pulse-shaper calibration

Obvious criteria for a good calibration procedure are a stable light source with a sufficiently broad spectral bandwidth and high spatial beam quality, as well as a spectrometer with a high signal-to-noise ratio and a spectral resolution exceeding that of the pulse shaper.

Further, more subtle factors include the selection of the constant voltage of the inactive layer. To minimize the amount of inter-layer voltage crosstalk, the voltage is usually set to a value in the middle of the interval used on the active layer. In the LCD used here, a voltage step of around 2000 is therefore used when calibrating the whole 4096-step range, or a constant voltage between 200 and 300 if the final calibration only consists of a 2π phase range with voltage values between 100 and 400. One has to be aware of the fact that the value of the constant voltage shifts the calibration curve of the scanned layer, i.e., the transmission curve will always have a maximum if the voltage value is the same for both layers. Therefore, a constant voltage value of 4095 is advised if the calculation of the phase-to-voltage calibration, i.e., the detection of the extreme values on the transmission curve, is the factor limiting the calibration quality. A maximum at voltage value 4095 ensures a minimum at a voltage position well below the high-voltage limit. This may be desirable since for the highest voltages, the curves have the lowest slope, but also the highest noise, hindering a robust detection of the maximal and minimal positions in the transmission curves.

Phase-to-voltage curves of low quality, i.e. containing high noise or obvious deviations from the expected monotone behavior should be excluded to avoid influence on the adjacent curves during the smoothing of the curves in pixel direction. In the end, by interpolating and extrapolating the remaining "good" curves in addition to smoothing both in voltage and in pixel direction should result in a robust phase calibration. The issues with voltage crosstalk can be reduced if the selected $n \cdot 2\pi$ region is chosen at low voltage values. The origins of both types of crosstalk, intra- and inter-layer, is discussed now.

2.12.2 Pixel crosstalk

Each liquid crystal pixel is embedded in a plate capacitor and switched by the electric field applied to it. Ideally, each pixel is only affected by the voltage set to its own pixel, which is a reasonable approximation. Especially for high voltage differences, as they occur, e.g. for phase jumps, the influence of neighboring pixels has to be considered. The issue can directly be observed through dips in the spectral intensity, especially for high amounts of additional phase applied. It has no influence on the phase-to-voltage

calibration procedure, since the same voltage is applied to the whole layer at any time. The influence on the wavelength calibration is also considered minimal. Personal communications with the manufacturer of the LCD used in this work and other working groups have confirmed this influence of voltage differences between neighboring pixels. Countermeasures can be taken by feedback loops and adaptive voltage fine-tuning, ideally with the help of spectral interference to include phase information. In this work, no additional optimization on this intra-layer crosstalk has been facilitated. In contrast, the crosstalk between the same pixels on the two different layers is considered more severe and countermeasures are taken, as seen below in Section 2.13. Voltage scans have shown that systematic deviations from the estimated behavior (defined by the calibration) in the actual phase applied exist. For a single pixel, constant deviations could be attributed to the calibration disturbances described above. However, besides the wavelength dependence, phase deviations in dependence of the applied voltage on the first LCD layer $\Phi(U_1)$ and the voltage of the second LCD layer $\Phi(U_2)$ and the combination of both, $\Phi(U_1, U_2)$, were unraveled. This is attributed to overlap of the electric fields from electrodes of one layer to the other one. Furthermore, owing to the direction of the field, these deviations also depend on the sign of the voltage difference, i.e., a correction of the sort $\Delta U(U_1 - U_2)$ cannot be simplified to the absolute phase difference $\Delta U(|U_1 - U_2|)$. Since the inactive layer in the calibration is left at the same voltage for the whole procedure, it is inherently insensitive to the inter-layer crosstalk. Therefore, a phase-correction procedure is presented in Section 2.13, after additional pulse-shaper imperfections have been discussed.

2.12.3 Fabry-Pérot effect

Back-reflections in transmissive optics result in delayed pulse copies, effectively forming a Fabry-Pérot resonator. In consequence, periodic intensity modulation over the spectrum and pulse replica in the temporal domain are observed. These effects are usually suppressed by the design of the optics, most prominent by the use of anti-reflection coatings or generally by avoiding interfaces with high difference of the refractive indices. In case of the LCD at hand, this suppression is apparently missing for certain interfaces, most likely between the transparent electrodes and the liquid-crystal layers. Resulting oscillations are observed in the spectra, as seen in Fig. 2.17(c). The influence on the spectra is not constant in this case, as the optical path length of the resonator is changing with the applied voltage. As a result, the modulations pose a problem that is not simply fixed by a static correction. In addition, the influence on the transmission curves of the calibration is not trivial. As an approximation, the oscillation can be averaged out either by smoothing or fitting (e.g. spline or polynomial). However, as presented in Section 2.13, more advanced correction mechanics can be applied instead, which also take care of the pixel crosstalk described above.

2.12.4 Space–time coupling

A phase change of a spectral component through a spatial light modulator is accompanied by spatial beam profile distortions. This effect termed space–time coupling was reported on theoretically already in 1994 [142]. In the last decades, studies on space–

time coupling and other pulse shaper artifacts followed, which also compared different pulse-shaper configurations [136–138, 140, 141, 143–145, 149–151]. In general, the influence of spatial shifts on phase and amplitude can be considered minimal as long as the spatial deviations do not alter the functionality of the optical components. This is especially valid when calibrating the pulse shaper if the detector and previous optics do not clip parts of the beam profile. For more complex optical systems like microscope objectives, the influence of space–time coupling has to be characterized. In the experimental setup used in this work, spatial chirp and other beam profile distortions were investigated by the nanorod measurements presented in Section 2.10.1. As a result, no significant impact on the beam was observed, even when the light was passing spatially sensitive optics as the microscope objective and a PH (PH_2 in Fig. 2.1). Therefore, space–time coupling is considered to be minimal and no further countermeasures have to be taken for the experimental setup at hand.

2.13 Pulse-shaper artifact correction

2.13.1 Pulse-shaper calibration fine tuning

Previous sections have shown how a pulse-shaper calibration is measured and evaluated in a systematic way. Once applied, the calibration can easily be tested with transmission masks, most prominently zero transmission, and looking at the shaped spectrum. The influence of phase jumps can separately be tested by applying only a linear phase mask and checking the influence on the transmission at the spectral position where the pulse shaper is wrapping the phase curve. An investigation by spectral interference or other methods for phase retrieval allows for additional information on the quality of the calibration, as it allows for analysis of arbitrary phase and amplitude masks. In the case of transmission masks, an additional optimization can be conducted if the primary calibration proves to be flawed. Assuming effects as described in the previous section, i.e., Fabry-Pérot-type deviations or voltage crosstalk, the phase-to-voltage curves are affected and the real applied phase values differ from the intended ones. If the curves are simply shifted by a certain voltage, a constant voltage offset ΔU to the whole curve, but individually for every SLM pixel, can be retrieved. This constant voltage correction is presented in the next section.

2.13.2 Constant voltage correction

The principle of the constant voltage correction is sketched in Fig. 2.20. The numeric values given in this figure are given to ease understanding of the method, but do not originate from experimental data.

In Figs. 2.20(a-c), the voltage calibration of a pulse shaper is shown for three exemplary pulse-shaper pixels corresponding to the wavelengths 765 nm (red), 770 nm (green), and 775 nm (blue). The colors illustrate the connection to this wavelengths throughout Fig. 2.20. The phase-to-voltage relations in Figs. 2.20(a-c) are assumed to be flawed, i.e., the curves are displaced by a constant voltage in relation to a correct calibration depicted as the curves dotted in black. To correct the flaws, the curves would have to be shifted back by a voltage correction value ΔU, as shown in Fig. 2.20(c). The correction

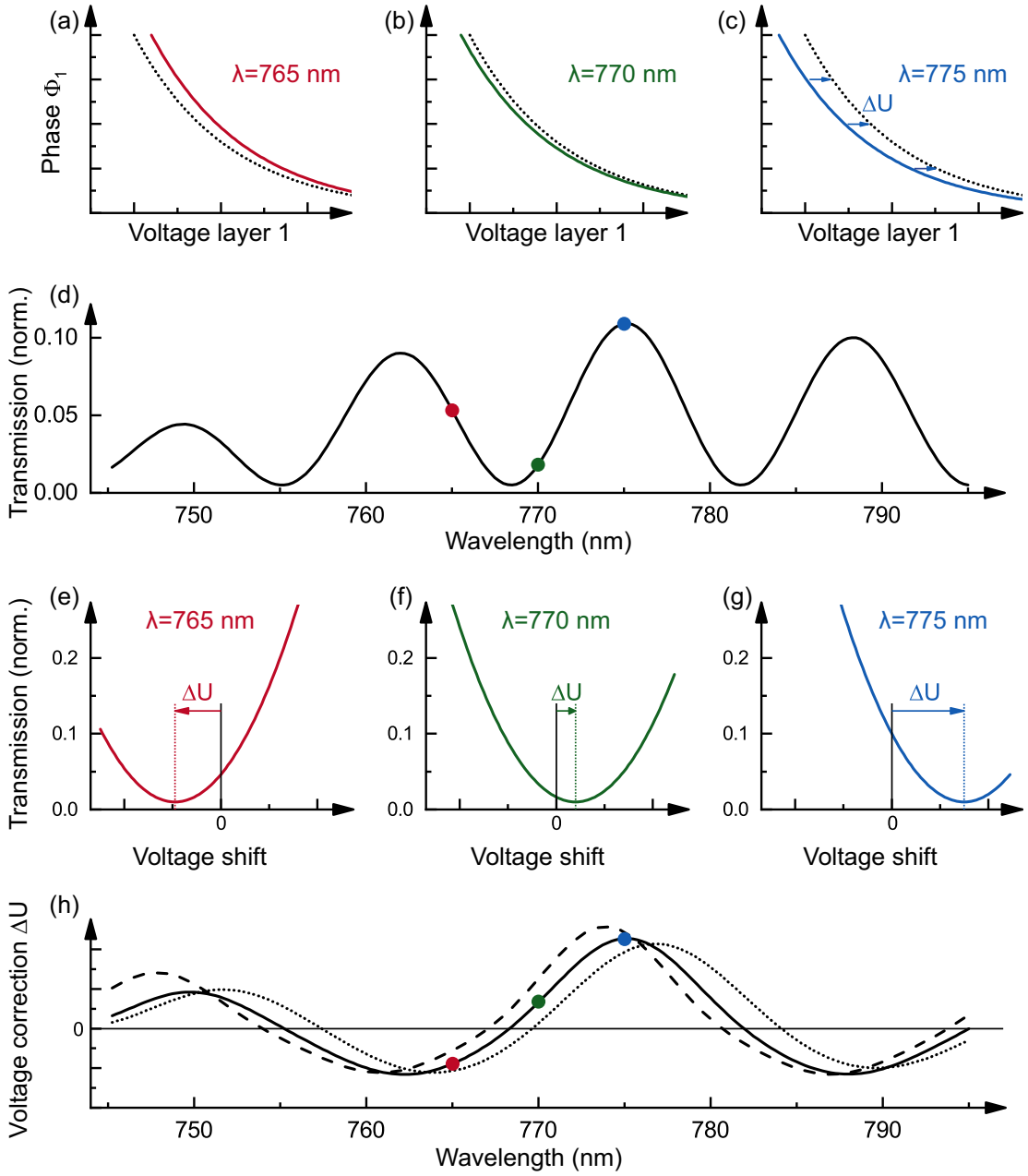

Figure 2.20 | Principle of the constant voltage correction procedure, exemplified by pulse-shaper pixels corresponding to wavelengths of 765 nm (red), 770 nm (green), and 775 nm (blue). (a-c) Individual phase-to-voltage curves of a flawed calibration (solid lines) displaced by a constant voltage offset ΔU from the actual relation (dotted lines). (d) Residual transmission resulting from a flawed calibration despite setting a pulse shaper to minimal transmission. (e-g) Determination of ΔU for each individual pixel by scanning the voltage around the flawed minimal transmission value. (h) Resulting voltage correction values for the exemplary pixels (colored spheres), the whole displayed spectral range (solid line) and additional corrections using constant voltage offsets for both layers (dashed and dotted lines).

is assumed to be constant for the whole voltage range U_1 applied to a single pixel of the first pulse-shaper layer, but dependent on the pixel x and therefore the wavelength.

As mentioned above, a common check for the quality of the pulse-shaper calibration is to apply a zero transmission phase to the pulse shaper. Without correction, residual transmission is expected for parts of the spectral range, as can be seen from the black line in Fig. 2.20(d). In this example, the high voltage offset at 775 nm leads to a high transmission (blue sphere) compared to other parts of the spectrum.

By scanning the voltage applied to the first pulse-shaper layer in a range around the assumed phase for zero transmission, the actual voltage leading to minimal transmission can be determined for each pixel, as is depicted in Figs. 2.20(e-g). The voltage difference between the expected and the actual minimum of transmission directly corresponds to the voltage correction ΔU. The voltage correction $\Delta U(x)$ is determined for all pulse-shaper pixels x. An exemplary result is plotted in 2.20(h) as the solid black line together with the three colored spheres corresponding to the regarded pixels. This correction is applied to the first pulse-shaper layer as offset for all pulse shapes.

In the pulse-shaper design considered here, i.e., with parallel polarizer scheme, minimal transmission is achieved when the phase difference between the two layers is set to π. This relation $[\Phi_1(U_1) = \Phi_2(U_2) \pm \pi]$ can be deduced from Equ. 2.5. Since a constant phase applied to both pulse-shaper layers does not affect this phase relation, the correction procedure can be repeated for different absolute voltage positions.

In theory, one would expect the same resulting voltage correction $\Delta U_{\mathrm{corr}}(x)$ for a constant shift of the calibration curves as depicted in Figs. 2.20(a-c), regardless of which position on the curve is chosen. Due to more complex influences, e.g., voltage crosstalk between the pulse-shaper layers, the voltage offset can vary. Examples for the resulted shifted curves are shown in Fig. 2.20(h) as the dashed and dotted lines. The voltage correction $\Delta U_{\mathrm{corr}}(x)$ can be refined by averaging over the variations for each individual pixel. For further refinement, the correction procedure can be repeated for pulse shapes resulting in maximal transmission, i.e., by applying the same phase to both pulse-shaper layers $[\Phi_1(U_1) = \Phi_2(U_2)]$.

Following to the procedure described above, the constant voltage correction was experimentally carried out for the pulse shaper used in this work. The voltage U_1 of the first pulse-shaper layer was scanned around the zero transmission value proposed by the calibration. Figure 2.21(a) shows a scan around the initial voltage value, with a shift range from -50 to $+50$ steps at a step size of 1. The color-coded transmission showed oscillatory behavior along the wavelength-direction, most likely due to the Fabry-Pérot-type effects. For every spectrometer pixel, the voltage-dependent curve was normalized and the minimum value was marked with a green dot in the plot. To smooth the resulting wavelength dependence, each curve was fitted by a Gaussian curve (with negative amplitude) in voltage direction, followed by a spline fit in wavelength direction. The resulting curve is plotted in white in Fig. 2.21(a). The Gaussian fit is justified since the voltage curve is nearly linear in the low-voltage region, resulting in a symmetrical shape of the transmission curve along the voltage direction. The systematic deviation between the points with minimal transmission and the fitted curve at the red part of the spectrum most likely originates from the asymmetric range of the scan, but has negligible influence on the final correction, since additional iterations of the corrections

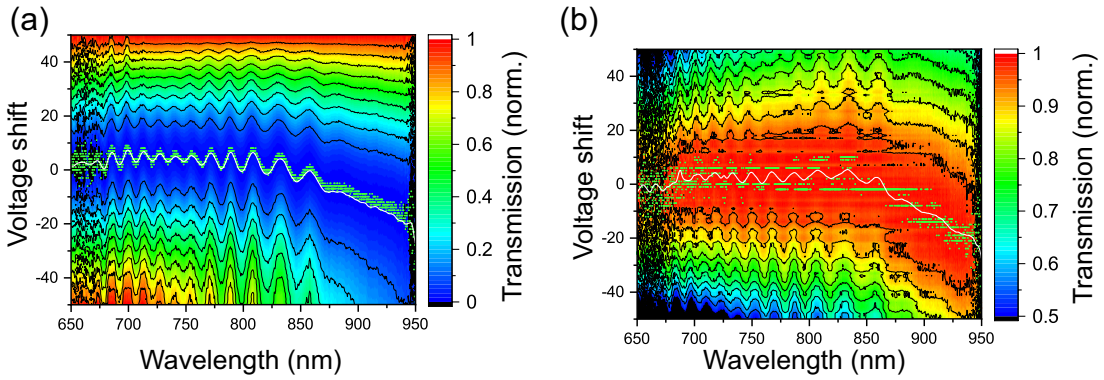

Figure 2.21 | Scans of the voltage offset ΔU around pulse-shaper phase setting for (a) minimal and (b) maximal transmission. The color-coded transmission curves are normalized individually for each spectral component. The minimal (a) and maximal (b) value of each spectral component is marked by a green dot (not related to the color bar), the result of a Gaussian Fit in voltage offset direction with subsequent spline-fit in wavelength direction is depicted by the white curves, forming the basis for the voltage correction.

are conducted. In general, for asymmetric scan ranges and phase-to-voltage relations with significant curvature, an asymmetric fitting function is advantageous.

To get a confirmation that the acquired phase-correction curve is valid for all phase combinations, additional measurements were taken. If the relative phase between the two layers is zero, maximal transmission is applied. A second voltage offset scan was taken for this case, as seen in Fig. 2.21(b). From this measurement, the need for fitting and smoothing the maximum position curve becomes apparent. Due to noise, the maximum value in the voltage-dependent curves could not reliably be extracted by the point with highest intensity. The fitted and smooth curve follows the oscillatory behavior indicated by the contour lines in the plot. In addition to a change in the relative phase between the two layers, the absolute phase was offset by a constant phase, shifting both voltages through the defined phase range of 2π and inducing phase jumps where the offset leads to phases exceeding the range. Both for the voltage shift scan around the minimum and the maximum, the measurement was repeated for each constant voltage offset of $\pi/10$, resulting in 20 measurements each along the complete range of 2π. The average voltage shift curve can be seen in Fig. 2.22(a) both for the measurement around the minimum (green curve) and the maximum (red curve). The fact that they closely resemble the same oscillatory behavior validates the theory of the curves being merely shifted by the influence of artifacts, primarily Fabry-Pérot-type, rather than having a wrong profile.

From the mean correction curves acquired from the minimum and the maximum transmission measurements, the common average was once more calculated, as seen in Fig. 2.22(b) as the red curve, and applied as pixel-dependent voltage offset to the phase-to-voltage calibration plotted in Fig. 2.19. The offset was applied solely to layer one. A symmetrical distribution on the two layers, i.e., half of the absolute correction value on each with different sign, would be an alternative approach with the advantage that only the transmission is changed and the overall phase from the initial calibration is kept intact. To decide which fraction of the correction has actually to be applied to the layers can only be done with a calibration correction facilitating additional phase

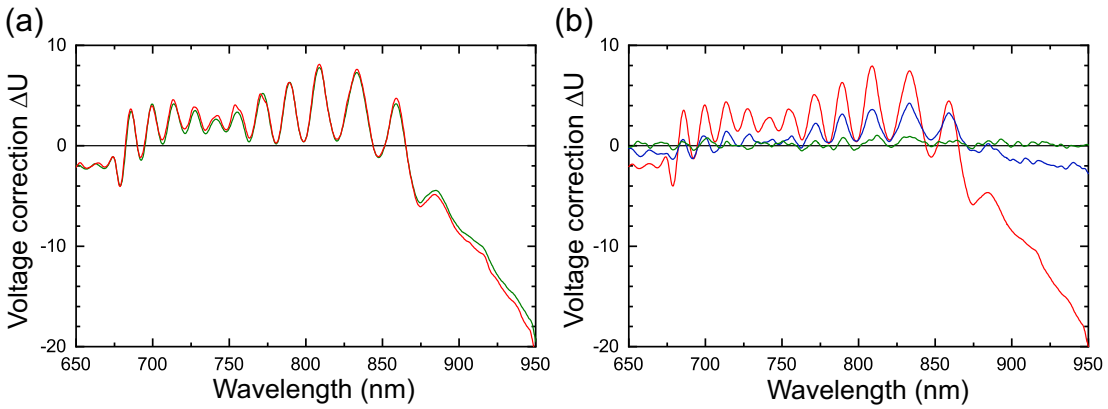

Figure 2.22 | Final result of the pulse-shaper voltage correction of the type $\Delta U_{\mathrm{corr}}(x)$. (a) Averages of the voltage offset corrections for minimum (green curve) and maximum (red curve) transmission, each obtained from 20 individual scans with different constant spectral phase applied. The close resemblance of the curves confirms the universality of the correction. (b) Mean voltage offset correction from minimum and maximum measurements for iteration 1 (red curve), iteration 2 (blue curve), and iteration 3 (green curve).

retrieval, e.g. spectral interference. Here, the correction procedure consisting of 40 voltage-offset-scans was iterated twice to refine and confirm the artifact correction. The results of the iteration two (blue curve) and three (green curve) in Fig. 2.22(b) showed gradual convergence of the phase-to-voltage calibration to a deviation of below a single voltage step towards the target positions.

The applied three-step correction optimized the transmission contrast achieved by the pulse shaper. In addition, the artifacts in the maps acquired by 2D spectroscopy, presented in Chapter 4, were significantly reduced by the constant voltage correction presented above. The latter is of the type $\Delta U_{\mathrm{corr}}(x)$ and thereby only dependent on the pulse-shaper pixel, i.e., the wavelength. It has proven effective despite solely relying on transmission measurements, without the need of additional spectral phase reconstruction, e.g. by spectral interference measurements. The correction can however be further refined by increasing its complexity, either by including phase retrieval or expanding the correction by including a voltage dependence of the two layers ($U_{1,2}$). The latter has already been implemented in the scope of this work and will be presented in the following section.

2.13.3 Two-dimensional voltage correction

The artifact correction of the type $\Delta U_{\mathrm{corr}}(x)$ presented in Section 2.13.2 brought improvements both to simple transmission measurements as well as complicated pulse shapes needed for nonlinear spectroscopy. However, it mainly addressed deviations in the initial calibration originating from Fabry-Pérot-type artifacts and static voltage-crosstalk from a fixed voltage applied to the inactive layer while scanning the voltage from the active layer. The inter-layer voltage crosstalk is expected to scale with the voltage difference $U_2 - U_1$ between the two layers. The correction $\Delta U_{\mathrm{corr}}(x)$ was taken for fixed phase differences between the two layers of zero (for full transmission) and π (zero transmission). With the additional scan of the constant phase across the whole accessible phase

range, the constant voltage offset ΔU for a single pulse-shaper pixel was averaged over a reasonable fraction of the full voltage range (U_1, U_2) selected in the calibration procedure. If the correction is extended to the format $\Delta U_{\mathrm{corr}}(x, U_1, U_2)$, this fraction should be expanded to represent all possible combinations of the two voltage ranges.

Similar to Section 2.13.2, the principle of the correction is illustrated in theory before the experimental implementation is presented. Numeric values depicted in Fig. 2.23 are for clarification, but not originating from experimental data. Figure 2.23(a) shows an example of residual transmission due to a flawed pulse-shaper calibration when a pulse shaper is set to zero transmission, equivalent to Fig. 2.20(d). The resulting transmission (black solid curve) is shown in relation to the desired transmission of T = 0.0 (black dotted line). Three exemplary pulse-shaper pixels are marked as colored spheres, corresponding to wavelengths of 765 nm (red), 770 nm (green), and 775 nm (blue). In the same manner, the behavior of a pulse shaper being set to different normalized transmission values can be depicted, as is done in Fig. 2.23(b) for T = 0.5 and in Fig. 2.23(c) for T = 1.0. Analogous to the procedure described in Section 2.13.2, voltage scans of the first pulse-shaper layer can be used to retrieve a pixel-dependent voltage correction $\Delta U_{\mathrm{corr}}(x)$. An exemplary correction is shown in Fig. 2.23(d) for minimal transmission, similar to Fig. 2.20(h). Accordingly, a voltage correction is plotted for T = 0.5 [Fig. 2.23(e)] and T = 1.0 [Fig. 2.23(f)].

In the procedure presented in Section 2.13.2, all voltage correction values of a single pulse-shaper pixel were averaged to obtain a constant correction. To account for voltage-dependent variations, the correction presented here is extended to the form $U_{\mathrm{corr}}(x, U_1, U_2)$. As a result, a correction map depending on the voltages of the first (U_1) and the second pulse-shaper layer (U_2) has to be created for every pixel x. This is shown for the three exemplary pixels in Figs. 2.23(g-i), where the amount of the voltage correction is displayed as the color-coded filling of the spheres. The color of the circles around the spheres represents the corresponding pixel x and thereby the wavelength. In the case of the wavelength 770 nm [Fig. 2.23(h)], this connection is additionally displayed by the green lines linking the individual data points to their origin from the voltage correction plots for different transmission values [Figs. 2.23(d-f)].

From the sparse data seen in [Figs. 2.23(g-h)], it becomes apparent that a high amount of voltage correction values $U_{\mathrm{corr}}(x, U_1, U_2)$ has to be retrieved to adequately describe the full voltage ranges. Analogous to the description in Section 2.13.2, this can be achieved by adding a constant phase to both pulse-shaper layers, as well as conducting measurements for additional transmission values. From the collected data, interpolating or fitting of the correction values is used to obtain a correction for all pixels and voltage combinations.

According to the description given above, the two-dimensional pulse-shaper voltage correction was carried out experimentally, which is presented in the following. Figure 2.24(a) shows the range of the voltages (U_1, U_2) used for the 2π calibration. The plot contains voltage combinations that were applied to the 100 pixels where the laser has the highest spectral intensity, color-coded for the relative transmission setting on the pulse shaper. Plotted in red are the voltage combinations that yielded full transmission which originate from the phase values $(\Phi_1(U_1) = \Phi_2(U_2))$ and the correspondent phase-wrapped condition $(\Phi_1(U_1) = \Phi_2(U_2) + 2\pi)$. As facilitated in Section 2.13.2, adding a constant phase to both layers does not alter the transmission, but shifts the voltages used

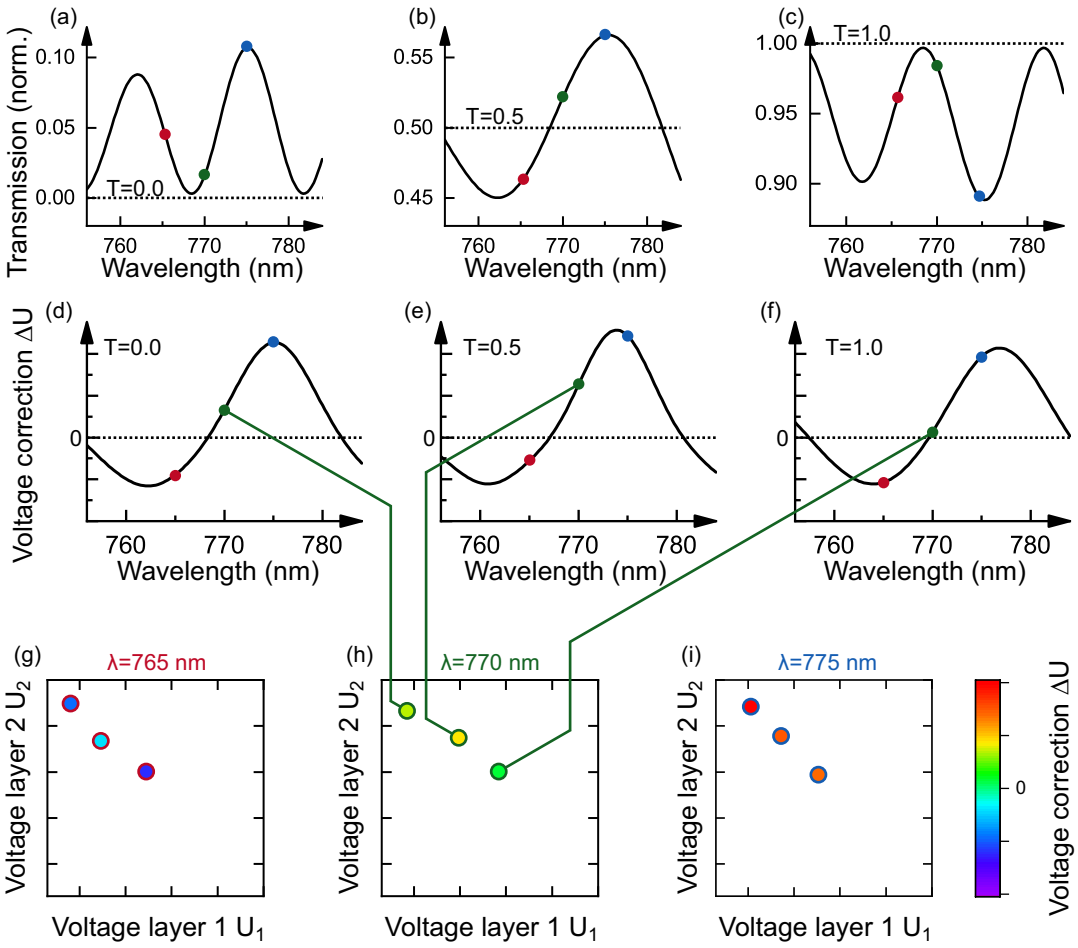

Figure 2.23 | Principle of the two-dimensional pulse-shaper voltage correction. (a-c) Transmission discrepancy between desired values of (a) T=0.0, (b) T=0.5, and (c) T=1.0 (dotted black lines) and exemplary values originating from a flawed pulse-shaper calibration (solid black curves). Three pulse-shaper pixels were selected for demonstration, corresponding to wavelengths of 765 nm (red), 770 nm (green), and 775 nm (blue). By voltage scans of the first pulse-shaper layer, separate pixel-dependent voltage corrections $\Delta U_{\mathrm{corr}}(x)$ can be obtained for each transmission value, as shown for (d) T=0.0, (e) T=0.5, and (f) T=1.0. For each pixel, an individual correction map in dependence of the voltages of the first (U_1) and the second layer (U_2) is created to obtain the correction $U_{\mathrm{corr}}(x, U_1, U_2)$, which is shown here for the selected wavelengths of of (g) 765 nm, (h) 770 nm, and (f) 775 nm. For 770 nm, the connection of the data points is depicted by the lines to the corresponding values in (d-f). For all data points in (g-i), the filling of the spheres relates to the value of the voltage correction ΔU, whereas the color of the circles corresponds to the respective pixel.

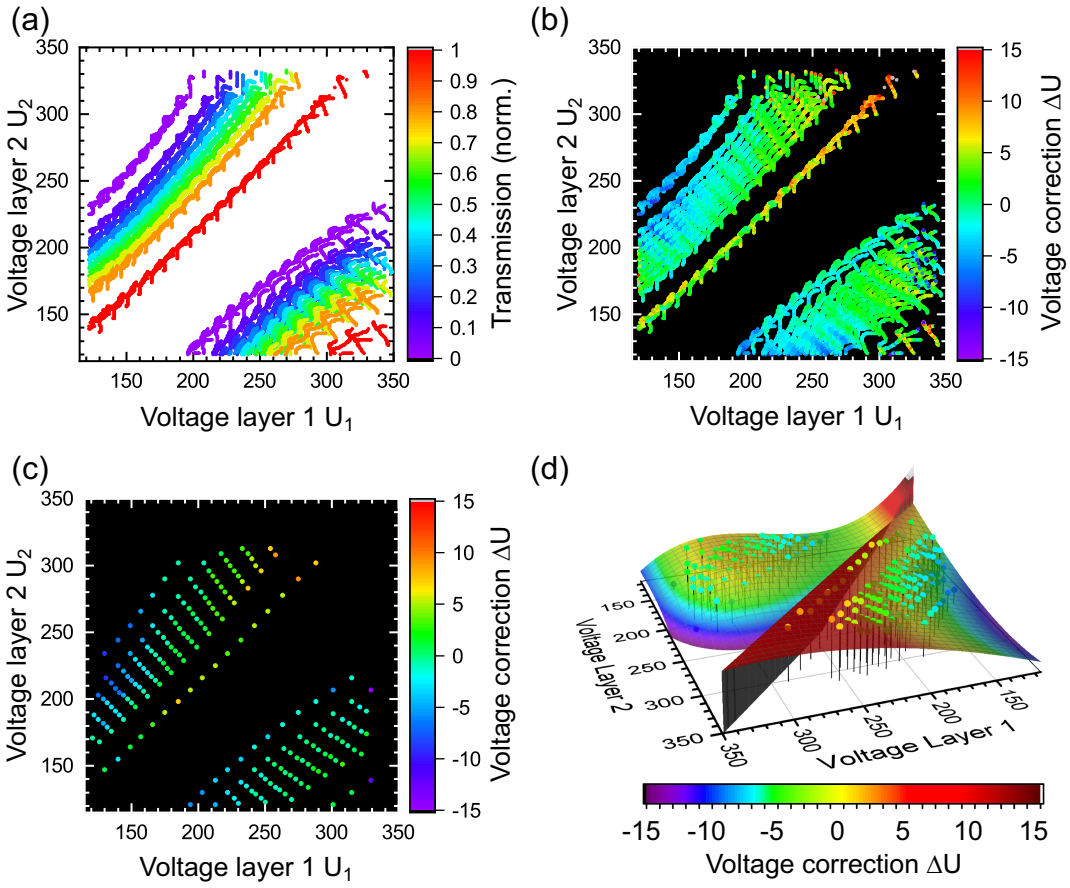

Figure 2.24 | Final result of the pulse-shaper voltage correction of the type $\Delta U_{\mathrm{corr}}(x, U_1, U_2)$. (a) Coverage of the ($U_1$, U_2) range by utilization of various transmission target values (0.0, 0.1, 0.2, 0.3, 0.4, 0.5, 0.6, 0.7, 0.8, 1.0) from the 100 pulse-shaper pixels of highest laser intensity. (b) Result of the voltage-correction values (color-coded) for all data shown in (a). (c) Voltage-correction value for pulse-shaper pixel 305 (maximum laser intensity). (d) The data from the single pixel is split into the two regimes $U_1 < U_2$ and $U_1 > U_2$ and separately fitted by a polynominal of third order in both voltage directions. Three-dimensional representation of the pixel-305 correction values (color-coded dots) and the polynominal fits (color-coded surface).

along the diagonal direction of the plot in Fig. 2.24(a). Shifts along the anti-diagonal direction correspond to a change in the difference phase and thereby a transmission change by using the phase relation $\Phi_1 = \Phi_2 \pm 2\arccos\left(\sqrt{T}\right)$ according to Equ. 2.5. Zero transmission was therefore reached by the phase combination ($\Phi_1(U_1) = \Phi_2(U_2) \pm \pi$), the resulting voltage combinations are plotted in violet in Fig. 2.24(a). Additional transmission values between 0.1 and 0.8 in steps of 0.1 were also recorded for the case $\Phi_1 < \Phi_2$, which in some cases actually led to $U_1 > U_2$ due to phase wraps in Φ_2. To achieve a full coverage of the voltage range (U_1, U_2), a similar set of transmission values could be measured for the case $\Phi_1 > \Phi_2$, which was not done for this proof of concept.

To gather the correction $\Delta U_{\mathrm{corr}}(x, U_1, U_2)$, voltage offset scans were taken for all 10 plotted transmission values with constant phase steps of $\pi/10$. The determination of the maximum and minimum positions for the measured scans with full and zero transmission was done according to the procedure described in Section 2.13.2.

For the scans with non-integer transmission values, a reference spectrum with full transmission was measured first. This was preferably done after voltage-offset correction of the full-transmission data to minimize the influence of the artifacts. The evaluation itself was done by comparing the scanned transmission data to the scaled-down reference spectrum. Besides a direct threshold determination, a preceding calculation of $|T_{\mathrm{scan}} - T_{\mathrm{ref}}|$ allowed for fitting a minimum in the same manner as presented above.

The obtained voltage correction $\Delta U_{\mathrm{corr}}(x, U_1, U_2)$ is shown as color code in Fig. 2.24(b). Although clear trends are observed, i.e., a positive correction voltage for both voltages being high and a negative voltage for one low and one medium voltage, averaging over all plotted data would result in a loss of information. Since this plot contains information from 100 pixels, the obtained correction $U_{\mathrm{corr}}(U_1, U_2)$ would only depend on the voltage dependencies, not on the pixels. To take one step back, Fig. 2.24(d) shows the correction $U_{\mathrm{corr}}(x = 305, U_1, U_2)$, solely for data collected on the pixel with the highest intensity in the laser spectrum. To extend this correction to all possible voltage combination of the single pixel, a polynominal fit of third order along both voltage directions was applied, as can be seen as the surface in Fig. 2.24(c) together with the voltage correction data of pixel 305. Additional measurements revealed a clear dependence of the correction on the sign of the voltage difference, i.e. $U_1 - U_2$. The physical design of the LCD itself seems to be the origin, but this claim has to be confirmed by further measurements. In the polynominal interpolation at hand, the data was individually fitted for two regimes, $U_1 > U_2$ and $U_1 < U_2$, to account for this dependency.

To extend the voltage correction to the full set of variables, two possibilities can be considered. If one assumes that the voltage crosstalk is the same for all pixels x and the initial calibration was merely disturbed by artifacts of the Fabry-Pérot-type, the correction could be split into a pixel and a voltage part, i.e.,

$$\Delta U_{\mathrm{corr}}(x, U_1, U_2) = U_{\mathrm{px}}(x) + U_{\mathrm{volt}}(U_1, U_2). \tag{2.7}$$

However, since the phase-to-voltage relation is not independent from the wavelength and thereby the pulse-shaper pixel, the most general correction

$$\Delta U_{\mathrm{corr}}(x, U_1, U_2) \tag{2.8}$$

may prove as the superior solution, where all three variables are globally fitted at once.

In the end, the described voltage corrections significantly improve the performance of the pulse shaper. In the most general case just shown, the correction is applied individually for all possible pulse shapes without the need for further reference measurements. In consequence, the detection of small changes in the response of the measured samples can be disentangled, which has proven advantageous for nonlinear spectroscopy, as presented in the following chapters for gold surfaces and nanostructures (Chapter 3), as well as for microscopic molecular surface systems (Chapter 4).

3 The nonlinearity of gold

3.1 Capabilities of plasmonic circuitry

The use of highly confined near-field excitations holds promise to create unique integrated device designs. Plasmonic circuits can outperform photonic devices in terms of integration density and electronic circuits in terms of transmission bandwidth [152–154]. Far-field radiation can be effectively coupled into and out of such plasmonic circuits with the help of optical antennas [155, 156]. Crucial for the design of logical elements in plasmonic circuitry is the ability to influence the near-field propagation direction. In devices realized so far, directional switching relies on linear interference of multiple plasmonic modes [4, 157, 158]. However, true conditional switching action as occurring in electric transistors requires the utilization of nonlinear effects.

One way to realize nonlinearities in plasmonic nanocircuitry consists in the combination of plasmonic materials with dielectrics having large higher-order susceptibilities. For example, the use of chalcogenide glasses has been proposed [159, 160]. However, the high precision required to embed such materials into plasmonic nanostructures constitutes a major obstacle for their realization. An alternative approach consists in directly using the nonlinear Kerr-type response of the electron plasma in metals [161]. This has been demonstrated, e.g., by four-wave mixing at gold surfaces supporting surface plasmons [162, 163] and in experiments showing third-harmonic generation in single plasmonic nanoparticles [164] and optical nanoantennas [165, 166]. The latter type of experiments make use of the fact that the inherent optical nonlinearity of plasmonic materials can be enhanced in well-designed, high-quality nanostructures in which considerable near-field intensity enhancement can be achieved. The design of plasmonic circuitry in which effects of the third-order nonlinearity of gold can be observed suffers from the lack of reliable knowledge of the nonlinear optical constants in the relevant spectral range. Uncertainties are related to the dependence of the nonlinear response on the crystalline structure as data obtained so far was recorded for multi-crystalline thin films [167–171] and data for single-crystalline gold films does not exist. Furthermore, it is unclear what effect the nonlinear refractive index has on propagation phenomena in plasmonic circuits.

In this chapter, measurements of the nonlinear refractive index of a homogeneous single-crystalline gold layer are presented and a new method to reveal nonlinear effects in plasmonic circuitry fabricated from single-crystalline gold is introduced. The nonlinear refractive index is studied using a z-scan experiment. To investigate effects of third order nonlinearity in plasmonic nanocircuitry a phase-sensitive nanointerferometer was designed which allows for retrieval of the upper bounds for nonlinear effects in plasmon propagation and in the formation of mode superpositions. The results offer some insight into the feasibility of nonlinear all-plasmonic switching based on gold.

3.2 Implementation of the z-scan method

The beam distortion resulting from the phenomenon of self-focusing of a high-power Gaussian beam within a nonlinear medium can be experimentally utilized to extract the medium's complex nonlinear refractive index $n_2 = n_2' + in_2''$, with real part n_2' and imaginary part n_2''. For this purpose, Sheik-Bahae et al. [172, 173] developed a sensitive measurement technique, the so-called z-scan method. Essentially, the sample under investigation is scanned along the longitudinal (z) direction through the focus of a laser beam, while simultaneously the fraction of light transmitted by a small, well-defined aperture placed in the diverging beam after the sample is detected in the far field (closed-aperture z-scan). This far-field transmittance shows a characteristic dependency on the exact sample position with respect to the focus caused by the self-focusing effect and allows the derivation of the sample material's n_2.

The shape of the z-scan transmittance curve is distorted by nonlinear absorption effects, e.g., due to two-photon absorption or saturable absorption. However, the nonlinear absorption can be measured separately by recording the whole transmittance with the aperture removed (open-aperture z-scan) allowing the determination of the imaginary part of the refractive index n_2''. At the same time an estimate for the real part of the nonlinear refractive index n_2' for samples showing nonlinear absorption can be obtained by a procedure that involves performing both an open-aperture and a closed-aperture z-scan and a subsequent division of the latter by the former [173].

In such a normalized z-scan the peak-to-valley transmittance change $\Delta T_{\text{p-v}}$ (i.e., the vertical distance between maximum and minimum transmittance) is related to n_2' using well-known equations of z-scan theory [174]. The real part of the nonlinear refractive index can be determined as

$$n_2' = \frac{1.232\lambda\tau w_0^2}{(1-S)^{0.25} E L_{\text{eff}}} \Delta T_{\text{p-v}}, \tag{3.1}$$

where λ is the vacuum wavelength, τ is the pulse length, w_0 is the beam waist radius, S is the aperture transmittance in absence of the sample, and E is the pulse energy. The effective length of the sample L_{eff} is defined as

$$L_{\text{eff}} = \frac{1 - \exp(-\alpha L)}{\alpha}, \tag{3.2}$$

with the linear absorption coefficient α and the physical length of the sample L. In this context, L_{eff} is referring to the intensity decay. From the open-aperture z-scan the imaginary part of the nonlinear refractive index can be estimated by [173]

$$n_2'' = -\frac{\lambda\tau w_0^2}{\sqrt{2} E L_{\text{eff}}} \Delta T(z=0), \tag{3.3}$$

where $\Delta T(z=0)$ is the transmittance change observed for the sample in the focus position. The above relations are only valid in the thin-sample regime, i.e., if L is smaller than the Rayleigh range. To obtain the nonlinear refractive index for thick samples more complex equations have to be used [175].

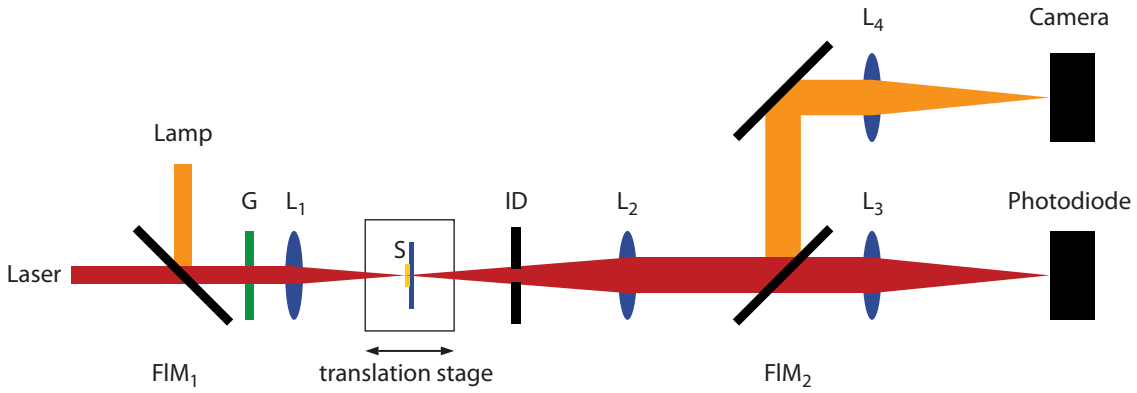

Figure 3.1 | Sketch of the experimental setup for z-scan measurements. For positioning, the sample plane is mapped onto the camera along the orange beam path under illumination with the lamp through lenses $L_{1,2,4}$. The ground glass plate (G) diffuses the white light to enable a uniform illumination of the sample (S). With G and the two flip mirrors ($FlM_{1,2}$) removed, the transmitted light from the laser is focused onto the photodiode along the red path and the translation stage is scanned. The imaginary part of the nonlinear refractive index n_2'' of the sample material is deduced from a z-scan without the use of the iris diaphragm (ID), termed open-aperture scan. Clipping of the beam by partial closure of ID is the basis for a closed-aperture scan. In general, both scans are needed to determine the real part of the nonlinear refractive index n_2'. Figure adapted from Ref. [2].

The z-scan setup is equipped with a light source capable of delivering a sufficient peak power for nonlinear experiments, even for materials with small higher-order susceptibilities.

In the present work, near-infrared pulses with a central wavelength of 797 nm and a pulse energy of 2.5 mJ are generated by a regenerative amplifier (Solstice, Spectra Physics) at a repetition rate of 1 kHz. The pulses pass a grating compressor, which reduces the pulse length to a typical value of 130 fs at the sample position which was confirmed by frequency-resolved optical gating (FROG) [176] measurements. If needed, power attenuation is achieved by neutral density filters. Power fine tuning is possible with the help of a half-wave plate in combination with a subsequent linear polarizer which also ensures a defined linear polarization state.

The z-scan setup is sketched in Fig. 3.1, where the laser beam path is depicted by the red line. The p-polarized laser pulses are focused by an achromatic lens L_1 ($f_1 = 25$ mm) onto the sample S. The beam waist of $w_0 = 5.9$ μm and the Rayleigh range of $z_R = 84$ μm were characterized by knife-edge scans. The sample is positioned within the xy-plane perpendicular to the beam propagation direction by manual translation stages. The sample positioning in z-direction and the actual scan is done by a motorized linear translation stage. The light transmitted through the sample is spatially confined by an optional iris diaphragm in the case of a closed-aperture z-scan. Afterwards, the beam is recollimated by the achromatic lens L_2 ($f_2 = 75$ mm) and focused onto a Si photodiode by the lens L_3. The photodiode is read out at 125 MSamples/s which allows integrating over about 0.2 μs for each laser shot, significantly enhancing the signal-to-background ratio when compared to continuous recording. For samples with a large surface area compared to the beam waist, no further positioning is necessary. If the

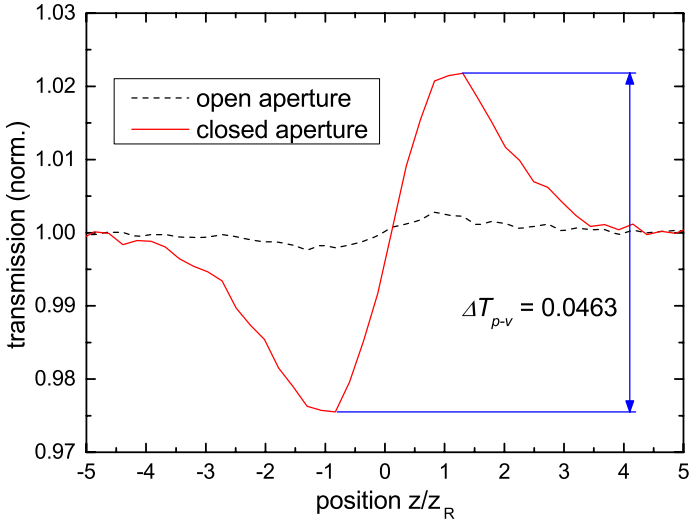

Figure 3.2 | Z-scan of a fused silica plate of 170 μm thickness. The open-aperture scan (black dashed line) shows slight modulation because the outer edges of the spatial beam profile are cut off in the detection path. The real part of the nonlinear refraction index n_2' can be extracted from the transmission change in the closed-aperture scan (red solid line). The latter was measured with partially closed iris diaphragm (ID). Figure adapted and modified from Ref. [2].

specimen covers only a small area in the sample plane, like the gold flakes measured in this work, precise sample positioning is indispensable. For that purpose, a different beam path (confer orange beam path in Fig. 3.1) is used by inserting two flip mirrors $\mathrm{FlM}_{1,2}$. White light from a halogen lamp is diffused by the additional insertion of a ground glass plate G (1500 grit) before reaching the sample plane. Hence, the sample plane is evenly illuminated and can be mapped onto a two-dimensional CCD chip (SPC900NC, Philips). In that case, the transmitted light is again collimated by lens L_2, while FlM_2 redirects the beam through lens L_4 to the camera.

To demonstrate the functionality of the z-scan setup, a fused silica plate of 170 μm thickness was measured. The normalized z-scan curves were averaged over 20 scans, both for open-aperture and closed-aperture scans, and are presented in Fig. 3.2. The scan direction was always from negative to positive z values, i.e., the distance between L_1 and S was increased during a scan. Both curves were measured with a pulse energy of $E = 28.4$ nJ, corresponding to a peak intensity of 0.20 TW/cm^2. The closed-aperture z-scan (red solid curve in Fig. 3.2) shows the characteristic behavior caused by a refractive-index modulation. The overall transmission change is evaluated to be $\Delta T_{\mathrm{p\text{-}v}} = 0.0463$. According to the modified calculation for thick samples [175], this corresponds to a real part of the nonlinear refractive index of $n_2' = 2.9 \cdot 10^{-20}$ m^2/W. For fused silica, values between $2 - 5 \cdot 10^{-20}$ m^2/W have been reported for near-infrared pulsed laser sources [177–180], proving the reliability of the setup.

An equally shaped but significantly less modulated curve has been measured in the case of the open-aperture z-scan (black dashed curve in Fig. 3.2). Since the aperture after the sample is removed, an antisymmetric characteristic relative to the origin of the z axis is not expected. This residual transmission modulation is attributed to a slight clipping of the spatial beam profile at lens L_2 which also acts as an aperture. In

both measurements of the fused silica plate (Fig. 3.2), the transmission change shows a symmetrical modulation for a variation of the focus position, indicating the absence of significant nonlinear absorption resulting in a negligible value of n_2''. This means the purely real value of n_2 can be calculated directly from the transmission modulation $\Delta T_{\text{p-v}}$ in the closed-aperture z-scan without initial division by the open-aperture z-scan data. Since the closed-aperture z-scan is not affected by the finite size of L_2, no corrections have to be taken into account.

3.3 Z-scan measurements of thin single-crystalline gold films

The z-scan method is now applied to a single-crystalline gold flake [181, 182]. Two criteria have to be met by the sample in order to make such measurements possible. On the one hand, its transmittance has to be high enough. On the other hand, the sample must be homogeneous over an area corresponding to the beam size at positions a few times the Rayleigh range away from the focus. Otherwise, the nonlinear transmission changes would be superimposed by aberrations from the sample inhomogeneity. The measured gold films had sufficient surface areas of about 100×100 μm^2 with a thickness in the range from $20 - 100$ nm, which was determined by transmission measurements at low powers. An increased heat dissipation for thicker gold layers leads to a higher damage threshold [183], at the cost of lower transmission. However, in terms of nonlinearity, thicker flakes have no advantage. Using the absorption coefficient $\alpha = 0.0770$ nm^{-1} from Johnson and Christy data [184] at the laser central wavelength of 797 nm, the gold flake with a thickness of 63 nm investigated in the following has an effective length of $L_{\text{eff,63 nm}} = 12.89$ nm according to Equ. 3.2, which is already close to the effective length $L_{\text{eff},\infty} = 12.99$ nm in the limit of infinitely thick layers. The gold flake was prepared on a fused silica glass (thickness 170 μm, same as above). Since the light is attenuated by the gold layer before entering the glass, no nonlinear contributions from the glass are expected for the utilized pulse energy of $E = 32$ nJ. An open-aperture z-scan showed linear behavior, i.e., no variation of transmission beyond the noise floor. From the obtained standard deviation of 1.04 % in this measurement an upper bound for the absolute value of n'' of single-crystalline gold can be deduced via Equ. 3.3, giving $|n_2''\,(\text{Au})| < 0.6 \cdot 10^{-16}$ m^2/W for $\Delta T\,(z = 0) = 1.04 \cdot 10^{-2}$.

The results of 30 consecutive closed-aperture z-scans are shown in Fig. 3.3(a). As one can see, no change in transmission for the first five scans is visible. Afterward, a z-position-dependent transmission modulation arises and increases with each scan. The shape of the selected curves from the scans 10, 20, and 30 in Fig. 3.3(b) could be interpreted as an antisymmetric modulation originating from a nonlinear refractive index, superimposed with an increase in transmission due to saturable absorption. The latter has been reported for thin coarse gold films [168]. However, this cannot explain the increasing modulation from scan to scan. The scanning electron microscopy (SEM) image taken at the middle of the flake after the z-scan measurements [Fig. 3.3(b), inset] reveals the damage of the gold layer with a diameter of about 4 μm. The missing gold film is the reason for the transmission increase in the z-scans, whereas the glass, now exposed to high peak powers, could cause the antisymmetric (with respect to $z = 0$)

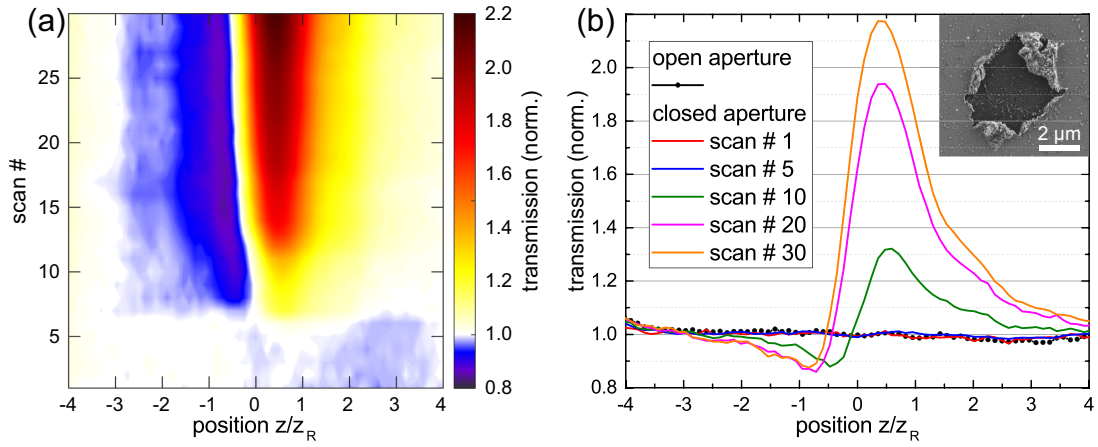

Figure 3.3 | Z-scan measurements on a single-crystalline gold layer of 63 nm thickness. (a) Transmission maps from 30 consecutively, identical closed-aperture z-scans. (b) The open-aperture z-scan (black line with dots) shows no z-dependent variation exceeding the measurements' standard deviation. From this, an upper bound for the absolute value of the imaginary part of the nonlinear refractive index $|n''|$ is calculated. The solid lines show five selected closed-aperture scans from (a). The curves for scan nos. 1 and 5 show no variations, the remaining curves show systematic z-position-dependent variation increasing from scan to scan. The variation is attributed to laser-induced damage of the gold layer, confirmed by SEM measurements (figure inset). Nevertheless, from the first two curves (scan nos. 1 and 5), an upper bound for the absolute value of the real part of the nonlinear refractive index $|n'|$ is calculated. Figure adapted and modified from Ref. [2].

nonlinear signal contribution. Diffraction at the gold film edge might also contribute to this modulation.

From the conducted z-scans, it was concluded that the damage threshold of the single-crystalline gold layer (63 nm thickness) is at the used peak intensity of 0.22 TW/cm^2, corresponding to a pulse energy per area of 0.029 J/cm^2. Since no deviations from the constant gold transmission could be detected within the measurement error (standard deviation for the closed-aperture z-scans of 0.97 %) during the first five closed-aperture z-scans, an upper bound for the absolute value of n_2' of single-crystalline gold was obtained, $|n_2'\,(\mathrm{Au})| < 1.2 \cdot 10^{-16}$ m^2/W. In this case of a thin layer, Equ. 3.1 is valid. $\Delta T_{\mathrm{pv}} = 9.7 \times 10^{-3}$ and $L_{\mathrm{eff}} = 12.89$ nm were used for the calculation.

For flat surfaces of gold, as in the demonstrated case, the interaction of the electromagnetic waves with the metal is hindered by the rather small penetration depth. The low effective length L_{eff} (see Equ. 3.2) of < 13 nm is an implication of the waves being expelled from the gold so that the major contribution to the nonlinear effect arises from the sample's surface region [185]. There are several processes that can contribute to the nonlinearity, e.g., the intraband contribution and the hot-electron contribution, which are described in detail in [167]. The contributions of relevance are determined (and therefore fixed) by their response time in comparison with the laser pulse length and the spectral regime used in the experiment. A way to further enhance the interaction is to use nanostructures. Due to confined and thereby resonantly enhanced optical near-fields that occur at such structures, an increased interaction with the metal can be achieved.

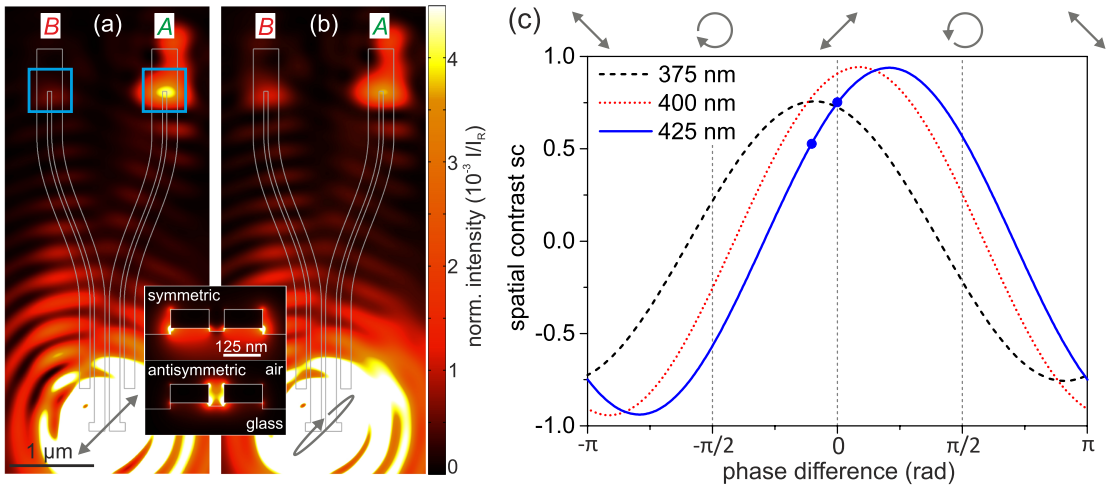

Figure 3.4 | Principle functionality of interferometry in a plasmonic nanostructure. (a) Simulated far field image of the phase-sensitive plasmonic nanointerferometer excited at the input antenna (overall length 425 nm) with a focused Gaussian beam polarized at 45° with respect to the antenna axis, as indicated by the gray arrow. The intensity scale is normalized to an unstructured gold surface reflection (IR). The structure's outline is superimposed as a guide to the eye. The blue squares indicate the regions used to evaluate the spatial contrast. (b) Simulated far field image of the identical structure assuming a change by $-\pi/10$ rad in phase difference between the two eigenmodes, i.e., increasing the ellipticity of the excitation polarization. (Inset) Simulated transverse modal profiles of symmetric (top) and antisymmetric (bottom) eigenmodes for the two-wire transmission line geometry, obtained using a mode solver (MODE Solutions, Lumerical Solutions Inc.). (c) Spatial contrast as a function of the introduced change in phase difference between the two eigenmodes for input antenna lengths of 375 (black dashed line), 400 (red dotted line), and 425 nm (blue solid line). The corresponding effective excitation polarization is depicted above. Figure adapted and modified from Ref. [2].

For this reason, a nanostructure that acts as a sensitive probe for nonlinear phase changes in plasmon excitations is introduced.

3.4 Intrinsic differential plasmon interferometry

Recent progress in the quantitative selective excitation of multiple eigenmodes [5] in plasmonic nanocircuits based on optical antennas [186, 187] and two-wire transmission lines [188, 189] have paved the way for the experimental demonstration of controlled plasmon propagation based on interference of well-defined modes in more complex nanocircuits [4]. This interference can be utilized to detect changes of the spectral phase difference between the modes. If one considers the propagation phase of a near-field mode that is subject to small changes when excited at different intensities, such changes can be monitored by sophisticated near-field probe methods (e.g., NSOM [190] and PEEM [191]) or spectral interferometry [80, 93, 94]. The latter reconstructs the complete plasmon propagation phase, but the extraction of small excitation-intensity-induced changes remains challenging. Therefore, the use of a phase-sensitive plasmonic nanointerferometer that intrinsically translates differences of the propagation phase into a far field intensity variation is proposed here. The latter can directly be measured by conventional optical

imaging techniques, significantly simplifying the observation. The outline of such a structure is shown in Fig. 3.4(a). The nanointerferometer is based on two-wire transmission lines supporting a symmetric eigenmode (Fig. 3.4(a,b) inset, top) and an antisymmetric eigenmode (Fig. 3.4(a,b) inset, bottom). A linear combination of these near-field modes can be excited at the input antenna, resulting in a beating pattern along the propagation direction due to different effective wavelengths of the eigenmodes ($\lambda_{\mathrm{eff}}^{\mathrm{sym}} = 483$ nm and $\lambda_{\mathrm{eff}}^{\mathrm{antisym}} = 439$ nm for 780-nm vacuum wavelength). After propagation along the nanostructure, the light is coupled back to the far field at the two output ports, labeled A and B. The nanointerferometer was designed using finite-difference time-domain (FDTD) simulations (FDTD Solutions, Lumerical Solutions Inc.) to direct a superposition of both modes preferentially to one of the output ports with variable contrast ratios. A simulated far field image is shown in Fig. 3.4(a), showing a structure where the required mode superposition is generated using a +45° linearly polarized Gaussian beam (NA = 1.4) positioned at the center of an input antenna with overall length of 425 nm. This leads to a predominant routing of the intensity to the right branch and emission from output port A.

A quantification of the branching ratio in the nanostructure is achieved by introducing the spatial contrast sc, which is defined as follows:

$$\mathrm{sc} = \frac{E\,(\mathrm{A}) - E\,(\mathrm{B})}{E\,(\mathrm{A}) + E\,(\mathrm{A})\,,} \tag{3.4}$$

where E(A) and E(B) are the energies emitted from the output ports A and B, respectively, as determined by integrating 0.5×0.5 μm^2 regions indicated with blue squares in Fig. 3.4(a). In the linear operation regime, a well-defined polarization of the incoming light results in a certain spatial contrast defined by the relative phase and amplitude of the two excited modes and the exact geometry of the branching region. Spatial contrast values of sc = 0.79 and sc = −0.88 were experimentally obtained in these nanostructures by linearly polarized excitation at +45° and −45° relative to the long wire axis, respectively. A nonlinear refractive index leads to a phase variation of the propagating plasmons. The process is expected to occur in the antenna region, where the local field is largest. If the nonlinear effect varies in magnitude between the two superimposed plasmon modes, e.g., because of different field localization and enhancement, a relative phase change is introduced. Due to the decaying intensities of the propagating modes, phase changes upon propagation caused by nonlinear effects likely only play a minor role. The potential benefit of this kind of structure for studies of nonlinear effects is due to the phase sensitivity of the spatial contrast sc between the output ports, as can be seen in the reduced spatial contrast in Fig. 3.4(b) obtained for a relative phase change of $-\pi/10$ rad. In the simulation shown in Fig. 3.4(b), the effect of a nonlinearity has been approximated by introducing a phase difference between horizontally and vertically aligned excitation components, corresponding to an effectively elliptical excitation. In the case considered here of a $-\pi/10$ relative phase change, the spatial contrast, as defined in Equ. 3.4, was decreased from 0.75 to 0.53 for the structure featuring an overall antenna length of 425 nm. To investigate this further, structures that are nominally identical except for the input antenna length that influences the amplitude of each excited mode are considered [5]. Consequently, the

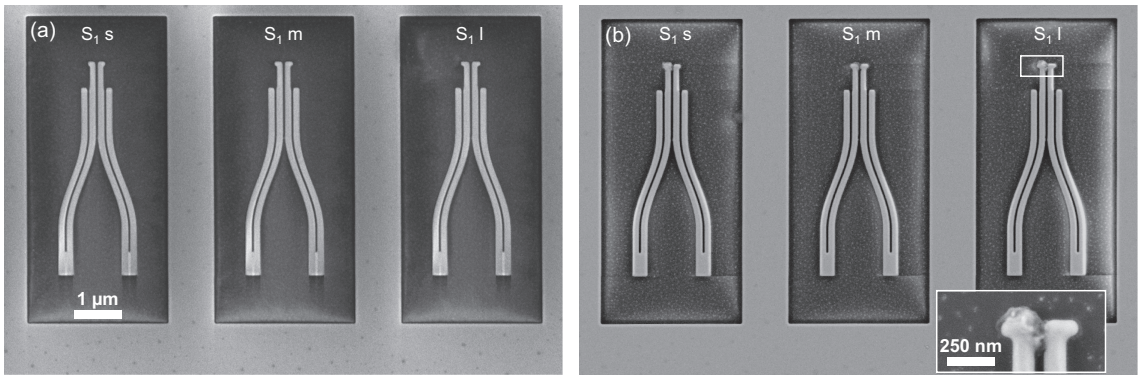

Figure 3.5 | SEM pictures of nanointerferometers before and after power-dependent excitation scans. (a) SEM picture of the three used structures of series S_1 right after fabrication. Antennas with the lengths 375, 400, and 425 nm (left to right) show no sign of damage. (b) SEM picture of the same structures after the power-dependent scans. All three antennas have clearly taken damage. The inset shows the partly melted 425 nm antenna of structure S_1 l. Figure adapted and modified from Ref. [2].

structures show varying spatial contrasts for the same +45° linearly polarized excitation in the simulations. The respective results for input antenna lengths of 375, 400, and 425 nm are presented in Fig. 3.4(c). A closer look at the spatial contrast as a function of the introduced relative phase change between the two eigenmodes reveals that the structure with overall antenna length of 400 nm shows the highest spatial contrast for +45° polarized excitation, whereas the other structures have slightly detuned antenna lengths leading to a reduced spatial contrast. Using +45° linear polarized excitation, the spatial contrast of the interferometer with 425 nm antenna length is expected to have the highest sensitivity for relative phase changes. In the following, the behavior of these structures for varying excitation intensity is investigated experimentally.

3.5 Intensity-dependent relative phase change in nanointerferometers

The experimental setup used for these studies consists of the Ti:Sapphire oscillator with subsequent LCD-based pulse shaper and high-NA microscope [3, 80] described in chapter 2. In combination with a pair of chirped mirrors, the dispersion from transmissive optics is pre-compensated in the pulse shaper by using the phase-resolved interferometric spectral modulation (PRISM) algorithm [90]. A pulse length of below 10 fs is reached at the sample position, measured by second-order autocorrelation. For power-dependent scans, a broadband half-wave plate in combination with a linear polarizer is utilized. Spatial maps are scanned and detected in reflection through the same objective by avalanche photodiodes. Instead of confocal detection, a two-dimensional image of the sample plane can be mapped onto a two-dimensional CCD chip (compare to Section 2.6).

For the experiments, the linear excitation polarization is kept fixed at +45°, resulting in an emission mainly from output A [Fig. 3.4(a)]. As described above, the spatial contrast is modulated if the relative phase between the two excited near-field modes varies.

Such variations would be expected to result from a nonuniform nonlinear refractive index. It is tested whether such a phase change occurs as a consequence of varying the power of the incident light. Two identical series of nanointerferometers, S_1 and S_2, were fabricated by focused ion-beam milling (FEI company, Helios NanoLab) from a single-crystalline gold flake deposited on a cover glass [181]. Within each series, the overall input antenna length is increased from structure to structure, resulting in slightly different relative amplitudes of the excited near-field modes. Apart from that, the geometry of the structures is identical. Four of these nanostructures were selected, three of them from series S_1 and one from series S_2. The former are shown in the SEM picture in Fig. 3.5(a). The antenna lengths for these structures are 375 nm for structure S_1 s (small), 400 nm for structure S_1 m (medium), and 425 nm for the identical structures S_1 l and S_2 l (large).

Figure 3.6 shows the spatial contrast between the output ports in power-dependent experiments for structures with different antenna lengths [425 nm in Fig. 3.6(a), 400 nm in Fig. 3.6(b), and 375 nm in Fig. 3.6(c)]. Subsequent series of measurements M_i on the same structure are labeled by the index i in chronological order. The error bars show the standard deviation of all measurements taken at the same power in a single series of measurements. Within each series of measurements, multiple up-and-down scans of the excitation power (called loops from now on) were performed. The intensity scan in a single loop is sketched in the inset of Fig. 3.6(c). Each loop consists of a scan with increasing intensity (labeled U) followed by a scan with decreasing intensity (labeled D). A series of measurements was stopped when the average spatial contrast within U differed by more than 10 % from the average spatial contrast within D in a single loop. Those irregularities can be an indicator for sample drift, because the spatial contrast is dependent on the exact incoupling position [5]. Since the contrast changes occurred mainly after a few loops close to the antenna damage threshold, it is attributed to sample degradation after an initial antenna deformation at the highest power within a loop. SEM pictures of the three structures of series S_1 taken after the intensity-dependent scans are shown in Fig. 3.5(b). The antennas have suffered visible damage and are deformed, which can be seen more clearly in the inset showing the 425 nm antenna of structure S_1 l. All three antennas were damaged at some point during the measurements, regardless if the highest used peak intensity was 52 or 127 GW/cm^2. Therefore, the damage threshold of the investigated phase-sensitive plasmonic nanointerferometers is determined to an upper bound of 52 GW/cm^2, corresponding to a threshold intensity having a factor of 0.23 relative to the threshold for homogenous gold layers determined above from the z-scan measurements. In terms of pulse energy per area, damage occurs at 0.48 J/cm^2. However, the observation that the gold film can withstand a given peak power for multiple seconds before taking visible damage was also made in the z-scan measurements in Sect. 3.3. The fact that the spatial contrast remained constant during a series of measurements until a rapid change at a certain point gives a hint that, until then, the nanointerferometers also withstood the incident laser pulses without taking damage. When a series of measurements was repeated afterward on the same wire, the spatial contrast again was constant for multiple loops. Nevertheless, the tendency that the absolute value of the spatial contrast gets smaller for repeated series of measurements on the same structure can be seen for all three antenna lengths. This tendency was also observed in simulations, where parts of one antenna arm were removed to mimic

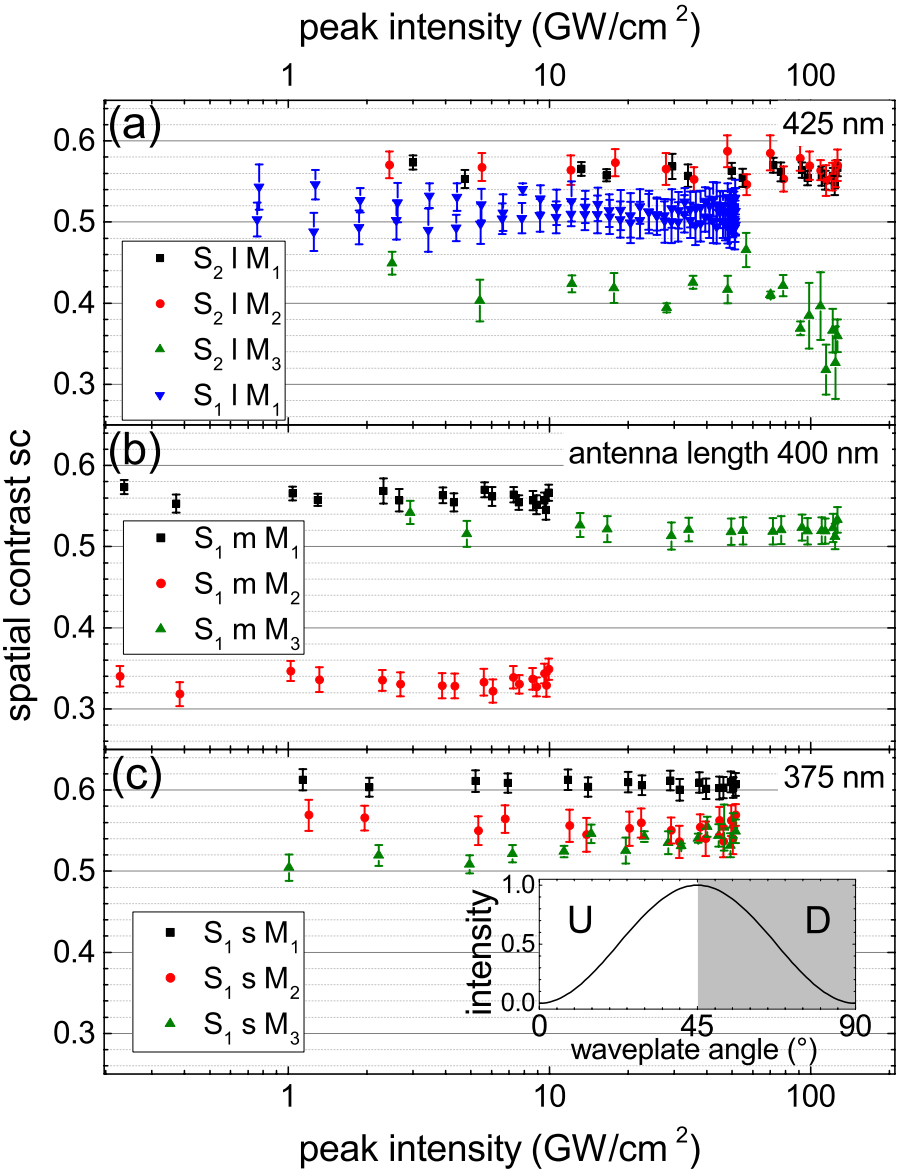

Figure 3.6 | Power-dependent scans of the spatial contrast in nanointerferometers. Each color shows a power-dependent series of measurements M_i on nanointerferometers with overall antenna lengths of (a) 425 nm, (b) 400 nm, and (c) 375 nm. Each series M_i consists of multiple up-and-down scans (loops) in excitation power. A single loop is depicted in the inset in (c). The average spatial contrast change between a pair of consecutive scans upwards (U) and downwards (D) is used as an indicator for sample drifts or laser-induced damage. The constant spatial contrast within each series of measurements is used to set an upper bound for the relative phase change of $\Delta\Phi < 0.07$ rad between the two excited plasmonic eigenmodes. Figure adapted and modified from Ref. [2].

the damage. Within one series of measurements, the power-dependent deviation of the spatial contrast is in the range of the error bars, i.e., no nonlinear effect is observable. Typical errors are in the order of 5 % of the spatial contrast value. To achieve experimentally detectable spatial contrast variations exceeding the measurement uncertainties using the most sensitive structures (S_1 l and S_2 l with an overall antenna length of 425 nm), according to the simulation model [Fig. 3.4(c)] a phase difference between the two eigenmodes of 0.07 rad or more would be required. Thus, it can be concluded that the experimentally achieved nonlinear relative phase change between the symmetric and the antisymmetric plasmonic eigenmode is below 0.07 rad.

To sum up, in the work described in this chapter, the nonlinear refractive index and the damage threshold of gold in thin films and plasmonic nanostructures was investigated. The z-scan method was implemented and verified on a fused silica film of 170 μm thickness. The obtained nonlinear refractive index, $n_2(SiO_2) = 2.9 \times 10^{-20}$ m^2/W, is in accordance with other reported values of z-scan measurements with near-infrared pulsed laser sources. Z-scan measurements of thin gold layers yielded a damage threshold of 0.22 TW/cm^2 and upper bounds of the real and imaginary parts of the nonlinear refractive index of $|n_2'(\mathrm{Au})| < 1.2 \times 10^{-16}$ m^2/W and $|n_2(\mathrm{Au})| < 0.6 \times 10^{-16}$ m^2/W, respectively, for a single-crystalline gold film with a thickness of 63 nm. A nanointerferometer was proposed as a sensitive probe for the relative phase change between two plasmonic eigenmodes of the nanostructures, leading to a change in spatial contrast between its two output ports. Nanointerferometers with different input antenna lengths and thereby different spatial contrasts of the emission signals in the linear regime have been investigated experimentally. The interferometers showed damage thresholds with a factor of 0.23 relative to homogeneous gold films. Furthermore, an upper bound for the introduced relative phase change of $\Delta\Phi < 0.07$ rad between the plasmonic modes was determined in the power-dependent measurements. The sensitivity of the demonstrated methods could further be enhanced by the use of shorter laser pulses and fine-tuning the design of the plasmonic nanointerferometers. With these improvements on z-scan and interferometric methods on single-crystalline gold, the determination of the nonlinear refractive index is in reach.

4 Coherent two-dimensional fluorescence micro-spectroscopy

In the last two chapters, the capability of the deployed experimental setup was described and demonstrated. With a spatial resolution down to the diffraction limit of a high-NA objective, temporally compressed laser pulses have shown powerful enough to excite plain surfaces and nanostructures up to (and beyond) their damage threshold. The additional possibility of arbitrary phase and amplitude pulse shaping, sophisticated femtosecond spectroscopy can be brought down to the sub-micron scale. This shall be demonstrated in this chapter by the introduction of a novel kind of two-dimensional fluorescence spectroscopy.

4.1 Two-dimensional spectroscopy at the diffraction limit

Ultrafast spectroscopy provides insight into molecular dynamics on the femtosecond timescale. Coherent two-dimensional (2D) spectroscopy [45] is a generalized version of transient absorption spectroscopy with frequency resolution for both the pump and the probe step. The method detects the third-order nonlinear response of the system under investigation and is often carried out on liquid-phase solutions, though it has been demonstrated also for other sample types. Examples for investigated systems are molecules [192, 193], quantum dots [194], nitrogen-vacancy centers [195], thin molecular films [196–198], nanodots [199–202], nanocrystals [203], or carbon nanotubes [204]. Most geometries detect a coherently emitted four-wave-mixing signal following three-pulse excitation, but incoherent population-based observables can also be used as has been demonstrated for fluorescence [58, 205–208], mass spectroscopy [209], or electron currents [98, 210–212]. The latter offers the possibility for nanometer spatial resolution when measured via photoemission electron microscopy (PEEM) [98, 211]. With all-optical methods, a spatial resolution of about half of the wavelength of the exciting electromagnetic field can be achieved according to the diffraction limit [82]. Ultrafast spectroscopy in the focus of microscope objectives has been successfully demonstrated [213–216], even down to the limit of single molecules in linear [70, 71, 217, 218] and in nonlinear studies [74, 219–221].

In general, 2D spectroscopy can be conducted in different geometries as reviewed recently [222, 223]. In box geometry, the three exciting laser pulses are overlapped on the sample from different directions and the nonlinear signal is collected in a fourth direction, given by the phase matching of the excitation wave vectors and allowing background-free detection. Especially for existing transient absorption experiments, a more convenient possibility is using the pump-probe geometry and splitting the pump pulse into two

collinear pulses via a pulse shaper [61]. Another option is a fully collinear geometry, where all excitation pulses share a common direction, often used in experiments where the response is probed by incoherent observables [58, 98, 205–212]. In collinear geometry, the different linear and nonlinear response contributions can no longer be separated spatially by phase matching because they are not emitted in distinguishable directions from the sample, and anyway, for incoherent observables phase matching does not exist. Instead, phase cycling can be utilized, where the difference phases between the individual laser pulses of a sequence are modulated [224] and the nonlinear contributions (e.g., the rephasing and the non-rephasing signal) are retrieved by linear superposition of differently phase-modulated raw data [205, 207–209]. Pulse shapers used for pulse sequence generation are inherently phase-stable, which is an advantage for these geometries.

In this work, fluorescence-detected two-dimensional (2D) spectroscopy [208] is combined with high-numerical-aperture (NA = 1.4) optical microscopy [3, 80] to establish the novel method of coherent 2D fluorescence micro-spectroscopy. A collinear pulse-shaper-generated pulse sequence is directed to chromophore systems and the resulting fluorescence is collected as a function of inter-pulse time delays and phases. With this all-optical approach, spatial variations of the nonlinear third-order response function can be detected. Such variations might be due to heterogeneities in the surface morphology or mixtures of different chromophores. This makes the method ideal for the investigation of material systems used in opto-electronic devices such as solar cells or light-emitting diodes.

4.2 Experimental realization

The experimental setup sketched in Fig. 2.1 and described in detail in Chapter 2 was initially developed for linear spectral-interference microscopy [3, 80] and was used for the investigation of propagation effects in nanoplasmonic systems [2, 4, 5], as demonstrated in Chapter 3. Modifications on the reported design (see Fig. 4.1) have been made for the present new application of nonlinear microscopy, in particular to deal with sample degradation in an optimal way and to implement fluorescence detection as discussed now.

The spectral bandwidth of the oscillator, ranging from 650 nm to 950 nm wavelength [Fig. 2.2(a)], is confined by hard apertures in the Fourier plane of the pulse shaper, in front of the liquid-crystal display. This way, the apertures act as a long-pass (LP) filter at 661 nm and a shortpass (SP) filter at 828 nm wavelength. In combination with a Schott KG5 color filter, this results in the spectrum of Fig. 4.2(a). A smooth shape ensures the absence of pronounced side peaks and other irregularities in the temporal pulse profile, which is crucial to avoid artifacts in spectroscopic measurements. By utilizing the PRISM algorithm [3, 90], the peak intensity measured by a two-photon photodiode (TPPD) placed in the focus of the microscope objective is maximized, leading to a transform-limited laser pulse. To measure the pulse duration, a pair of (compressed) pulses is created by the pulse shaper and the normalized signal from the TPPD is recorded in dependence on the inter-pulse delay τ. Figure 4.2(b) shows the resulting interferometric autocorrelation. From the Fourier-filtered trace, the pulse duration at the sample position can be determined to be 12.1 fs (FWHM) assuming the experimental

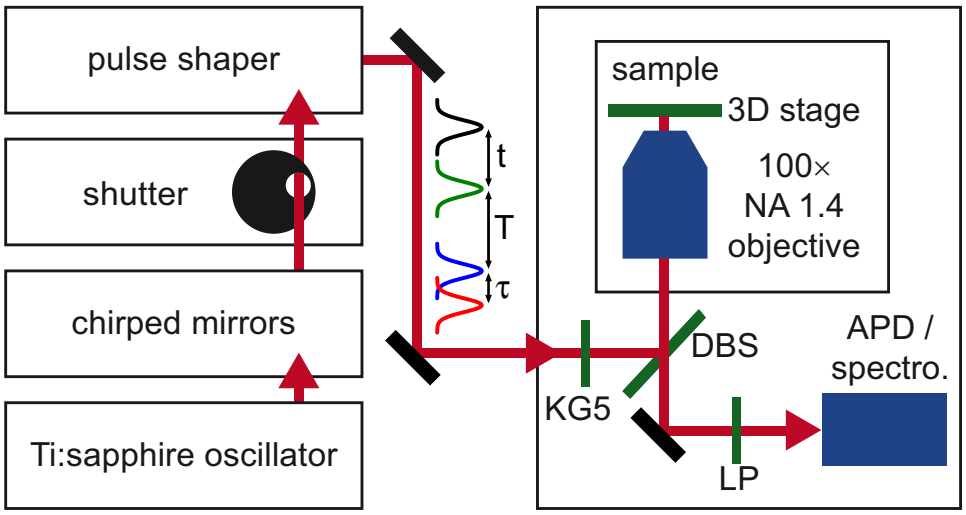

Figure 4.1 | Overview of setup for 2D fluorescence micro-spectroscopy. Chirped mirrors and a spatial light modulator are used for temporal pulse compression, the latter additionally for generation of pulse sequences. In the sketched four-pulse sequence, inter-pulse delays are defined by τ, T and t. Spectral confinement is faciliated by long-pass (LP) and short-pass (SP) apertures in the pulse shaper and by a Schott KG5 color filter in front of the dichroic beam splitter (DBS). Excitation of the sample and collection of the fluorescence is conducted by a high-numerical-aperture (NA) microscope objective. Separated from scattered light by an additional LP filter, the fluorescence is detected either by an avalanche photodiode (APD) or a spectrometer. Figure adapted from Ref. [1].

spectrum of Fig. 4.2(a). The measured result is close to the theoretical limit of 11.8 fs calculated using the experimental spectrum with a flat phase. The spectral confinement results in an increase of the pulse duration, both experimental and theoretical, compared to the values determined in Chapter 2. The spectrum in Fig. 4.2(a) is measured between the dichroic beam splitter (DBS, F48-810, AHF Analysentechnik) and the microscope objective plotted in Fig. 4.1.

All measurements using ultrafast laser pulses presented in this chapter were done with 12.1 fs pulse duration by applying the PRISM phase to the pulse shaper in addition to the mask pattern required for the pulse train. In the case of four-pulse sequences, the inter-pulse delays t, T and τ of the compressed pulses were controlled by the pulse shaper as well as the phases Φ_i ($i = 1, \ldots, 4$). The overall absolute carrier-envelope phase (CEP) of the pulses, i.e., the zero-order coefficient of the Taylor-expanded temporal phase, was not controlled. Manipulating the relative (CEP) inter-pulse phases Φ_i ($i = 1, \ldots, 4$) by the pulse shaper was sufficient.

Applying a phase mask to the LCD-based pulse shaper took about 1.2 s, mostly because of the physical rotation of the liquid crystal of the LCD array itself. On the other hand, acquisition times on an avalanche photodiode (APD) as used in this work could be set as short as 50 ms, still offering an acceptable signal-to-background ratio for samples with high fluorescence yield. This corresponded to a duty cycle of only 4 %, resulting in a high degree of sample photobleaching due to unnecessarily long exposure times. A circular step-motor-based shutter [Fig. 4.1(a)] with a response time below

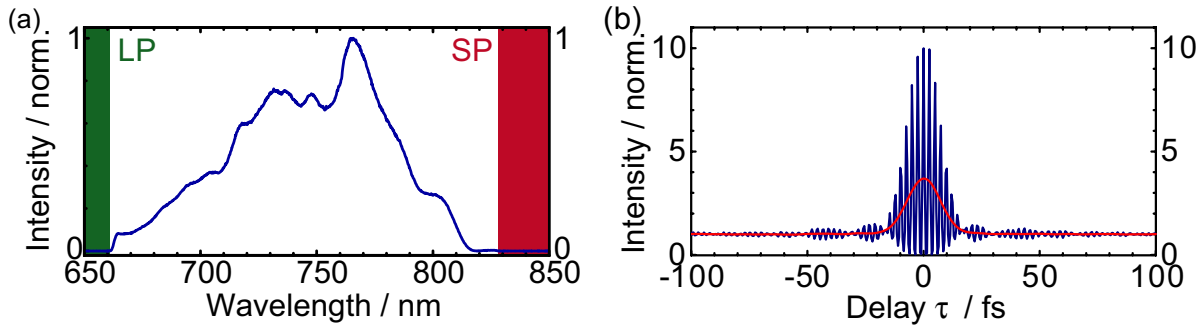

Figure 4.2 | (a) Laser spectrum measured after reflection from the dichroic beam splitter (DBS, blue). The spectrum is confined by long-pass (LP, green) and short-pass (SP, red) apertures and by a Schott KG5 color filter. (b) Collinear interferometric autocorrelation (blue) recorded by placing a two-photon photodiode at the sample position. From the Fourier-filtered curve (red), the duration of a single pulse is determined to be 12.1 fs (FWHM). Figure adapted from Ref. [1].

20 ms was therefore implemented, increasing the duty cycle by a factor of 7 in this example and thus greatly reducing the photobleaching for a fixed acquisition time.

The laser focus in the microscope was mapped by a piezo scanning stage (P-517.3CL, PI, Germany). The reflected light was collected by the same objective, transmitted through a dichroic beam splitter (DBS), and detected by either an APD (Perkin Elmer, SPCM-CD 2801) or a spectrometer [spectrograph (Acton SpectraPro 2500i, Princeton Instruments) and charge-coupled device (e2v, CCD42-10, Acton Pixis2kB, Princeton Instruments)]. The reflection intensity maps [Fig. 4.3(a)] provided a first optical characterization of the sample. By adding an additional emission filter (F76-832, AHF Analysentechnik), a map of the sample fluorescence was generated in the same manner [Fig. 4.3(b)]. By these scans of the sample plane, sub-micron-sized features of geometrical and material composition could be distinguished at a lateral resolution of 260 nm according to the Abbe diffraction limit (compare to Section 2.5). The absorption of the thin film samples was separately measured with a commercial spectrometer (V670, Jasco Deutschland GmbH).

4.3 Fluorinated zinc phthalocyanine thin films

As reference system, the fluorinated zinc phthalocyanine (F_{16}ZnPc) dye was chosen to demonstrate the capability of the newly developed method of 2D fluorescence micro-spectroscopy. The dye was directly evaporated on glass slides, resulting in a homogeneous layer growth of F_{16}ZnPc [225]. Previous nonlinear measurements of an approximately 300 nm thick F_{16}ZnPc layer (not shown) confirmed the onset of a nonlinear response at about 1 GW/cm^2 peak excitation intensity in the center of the focus during pulse duration (averaged over the temporal FWHM). Furthermore, the thin films have proven to be sufficiently photostable for measurements lasting up to 40 h at a peak excitation intensity on the order of 100 GW/cm^2, corresponding to an average intensity on the order of 100 kW/cm^2 at the center of the focus. While the nonlinear response of the sample scales with the peak intensity, i.e., the inverse pulse length, additional measure-

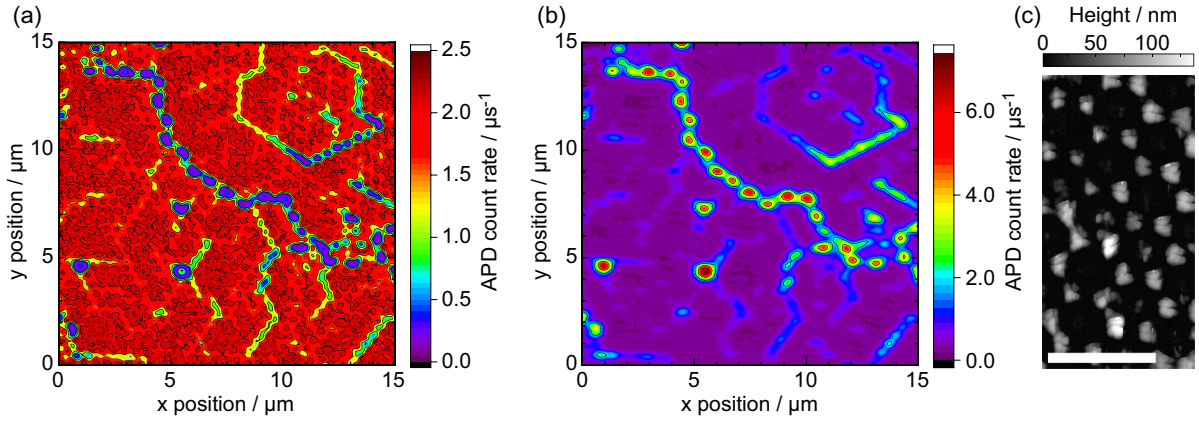

Figure 4.3 | Microscopic characterization of the in-plane structured F_{16}ZnPc pillar array. (a) Reflection intensity map, showing low reflectivity in regions where the regular hexagonal pattern is perturbed. (b) Fluorescence map of the same area as in (a). The regions of low reflectivity show the highest fluorescence yield due to the thick chromophore layer coverage. (c) AFM map from a structured region of the same sample (but not necessarily the same area), indicating the defects in the lateral pattern of chromophore pillars. Scalebar 1000 nm. Figure adapted from Ref. [1].

ments with uncompressed pulses have shown that photostability is mainly dependent on the average intensity. This indicated heating of the sample through absorption as the dominant bleaching mechanism rather than ultrafast photodamage.

As can be seen in the reflection image of Fig. 4.3(a), a regularly structured sample surface was obtained by evaporating the dye on a monolayer of spincoated polystyrene nanospheres of 500 nm diameter (Polysciences Europe GmbH) and subsequent lift-off of the spheres [226]. Thus, triangular pyramids of F_{16}ZnPc of an approximate size of 200 nm remained on the glass slide and formed a hexagonal ordered lattice indicating the positions initially not covered by the spheres. Defects in the sphere monolayer led to fissures in the regular F_{16}ZnPc nanopillar arrangement, recognized by the reduced reflection in this region.

Looking at the fluorescence of the same sample regions [Fig. 4.3(b)], the locally constricted dye coverage was verified by the existence of intensity hotspots. Thus, one can choose between a more confined dye pyramid inside the regular pattern or a brighter hotspot offering a better signal-to-background ratio. The latter makes it possible to conduct nonlinear measurements with lower excitation power, decreasing photobleaching. The surface structure was confirmed by AFM measurements [Fig. 4.3(c)]. More detailed information on the preparation and characterization of equivalent thin films is provided by Kolb et al. [226].

Figure 4.4(a) shows the laser spectrum (blue) in comparison to the absorption of plane and nanostructured F_{16}ZnPc films. The origin of the absorption features of a homogeneous film (black) has been reported before [225] as resulting from two coexisting crystalline phases at room temperature.

The laterally structured thin film of Fig. 4.3 shows a pronounced absorption around a wavelength of 600 nm [red in Fig. 4.4(a)]. However, this cannot directly be attributed to the crystalline structure of the microscopic pyramids since the absorption measurement

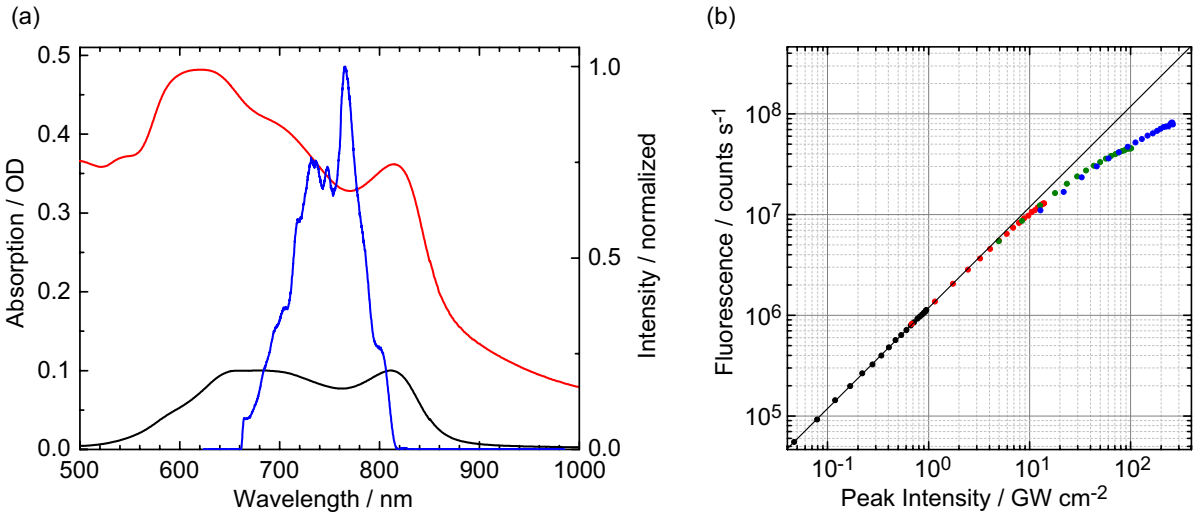

Figure 4.4 | (a) Absorption of a nanostructured (red) and a homogeneous (black) F_{16}ZnPc thin film in comparison to the laser spectrum (blue). (b) Excitation-power-dependent fluorescence of the F_{16}ZnPc nanopillar array, showing an onset of the non-linear response above approximately 1 GW/cm^2 peak excitation intensity, deviating from the linear trend (black line). Each color corresponds to an individual measurement with a different set of neutral density filters where a half-wave plate was rotated in front of a linear polarizer to scan the attenuation. Figure adapted from Ref. [1].

averages over several mm^2 consisting of several domains. The surface contained areas with homogeneously ordered dye pillars and areas still covered by nanospheres. The latter remained after the top layer was removed by liftoff in areas where a multilayer of spheres formed in the course of spincoating. The broadband contribution over the whole shown spectral range was attributed to absorption and scattering from these remaining nanospheres. The absorption of the dye itself showed only slight modulation in the range of the laser spectrum.

The nonlinear response needs to be above a certain level to allow reliable separation from the linear counterparts and the noise floor by phase cycling, since they are not geometrically separated when using a fully collinear measurement. To determine this level, a series of excitation power scans was conducted by rotating an achromatic half-wave plate (B. Halle Nachfl. GmbH) in front of a fixed linear polarizer. Figure 4.4(b) shows the resulting fluorescence response of a diffraction-limited hotspot on the previously described nanopatterned F_{16}ZnPc surface in dependence on the peak excitation intensity. A linear relation could be observed for peak intensities up to the order of 1 GW/cm^2, similar to the case of homogeneous layers. In such low-power measurements, one would expect to see no nonlinear signal contributions above the noise floor after phase cycling in 2D measurements. On the other hand, this means that if there are signals in the experimental data after phase cycling, they can possibly be identified as measurement artifacts, e.g., due to imperfections in the pulse-sequence generation. Such a procedure was used to remove artifacts from the nonlinear response maps in high-power measurements, as shown in Section 4.4.

The 2D measurements were performed by scanning coherence time τ and signal time t in 2 fs steps from 0 fs up to 60 fs, keeping the population time T fixed at 30 fs. Several

factors influenced the chosen total interval of the coherence time axes. The controllable time window with the Fourier-domain pulse shaper was proportional to the number of SLM pixels, ca. 2 ps in this case. The selected scan ranges of (60 fs, 30 fs, 60 fs) for the three time delays were set significantly below that limit. Longer time scans are possible, however, if the sample under investigation shows dynamics exceeding the chosen intervals or if a higher frequency resolution is desirable. For the system at hand, the parameters have been optimized to balance the requirements between frequency and time resolution, signal-to-noise ratio, and overall exposure time to reduce photobleaching.

The measurement was conducted in the partially rotating frame, where the observed frequencies $\omega^{\mathrm{rot}} = \omega^{\mathrm{lab}}$ - $\Delta\omega$ are downshifted from the frequencies in the laboratory frame ω^{lab} [45]. A shifting frequency of $\Delta\omega = 0.7\ \omega_0$ was used, where $\omega_0 = 2.59$ rad/fs is the fundamental frequency of the laser spectrum used for excitation. The frequency shift was introduced to avoid undersampling when using time steps of 2 fs. Measuring in the fully rotating frame ($\Delta\omega = \omega_0$) would in principle also be possible. In that case, however, the desired nonlinear signal would have appeared at an effective frequency of zero and would have overlapped with other, unwanted, contributions. Thus it was advantageous to choose a partially rotating frame. In the case at hand, a shifting frequency of $\Delta\omega = 0.7\ \omega_0$ was selected. This introduced a spectral offset large enough to separate the whole range of the excitation spectrum from stationary contributions avoiding artifacts. The spectral separation is crucial for both identification and isolation of the nonlinear part of the measured data.

A 27-step ($3 \times 3 \times 3$) phase-cycling scheme was used, allowing the extraction of the absorptive spectrum from the rephasing and non-rephasing nonlinear contributions [45, 224]. For each time step, the 27 different phase variations were measured as direct sequence with an averaging time of 1 s on the APD, followed by a reference measurement consisting of a single excitation pulse. This way, the advance of photobleaching was determined for each time step and accounted for by using the inverse intensity of the single pulse as a normalization factor for the 27 preceding four-pulse sequences. This correction is valid as long as a reasonable fraction of the chromophores in the center of the focus, i.e., in the region of the highest optical fields and therefore nonlinear response, is still intact. For further advance of the bleaching (approximately below 20 % of the initial fluorescence yield), the nonlinear response can no longer be reliably extracted.

According to the power scans in Fig. 4.4(b), the nonlinear scans should be measured above approximately 1 GW/cm^2 peak intensity. It would be desirable to use much higher powers, but the sample photostability sets an upper practical limit. For peak intensities on the order of 100 GW/cm^2, corresponding to roughly 100 kW/cm^2 average intensity when using a single laser pulse, a slow exponential decay of the fluorescence yield on the time scale of multiple hours was observed, which is accounted for in the nonlinear measurements by intensity correction according to the reference pulses. When nonlinear scans were conducted, a peak excitation intensity of 65 GW/cm^2 (251 kW/cm^2 average intensity was used, both values for temporally separated sub-pulses in a four-pulse measurement), offering a good compromise between nonlinear signal-to-noise ratio and photobleaching stability of the sample at hand.

4.4 Results and discussion

A four-pulse fluorescence measurement on a single diffraction-limited hotspot on the laterally structured F_{16}ZnPc film at a peak intensity of 65 GW/cm^2 (for temporally separated sub-pulses) was performed. The time-domain data was normalized to the recorded fluorescence intensity without pulse overlap, i.e., using regions from all 27 maps where both $\tau \geq 40$ fs and t ≥ 40 fs. The phase-cycled and Fourier-transformed 2D spectrum (absolute value) is shown for the rephasing [Fig. 4.5(a)] and the non-rephasing [Fig. 4.5(b)] contributions. The spectra are shown in the partially rotating frame as function of the observed frequency ω^{rot} downshifted by $\Delta\omega = 0.7\,\omega_0$. The major contribution is located along the anti-diagonal for the rephasing contribution [Fig. 4.5(a)] and along the diagonal for the non-rephasing contribution [Fig. 4.5(b)] spanning over the full laser spectrum. Additional features are seen along the diagonal lines and along a vertical line for $\omega_\tau^{\mathrm{rot}} \approx 0$. When repeating the measurement at a low peak excitation power of 3.5 GW/cm^2 in the dominantly linear regime, as described in Section 4.3, these features remain and can thus be identified as linear artifacts both in the rephasing [Fig. 4.5(c)] and the non-rephasing [Fig. 4.5(d)] map. The artifacts are primarily caused by pulse-shaper imperfections, both inherent to the LCD-type shaper design as well as the voltage-to-phase calibration of the LCD array. The artifacts are discussed in detail in Section 2.12 followed by correction methods with different levels of sophistication in Section 2.13.

In short, transparent gaps between the LCD pixels result in a fraction of the light transmitted through the pulse shaper without control over the applied phase. Furthermore, especially for neighboring pixels with large differences in the applied voltages, crosstalk shifts the actually applied phases for those pixels. The latter can be observed both for neighboring pixels in the same LCD layer (intra-layer) as well as for pixels in neighboring layers (inter-layer).

The voltage crosstalk can be reduced, but not fully avoided, by setting the working range to low voltages. Additionally, the design of the LCD array results in reflections at the interfaces between the glass, the transparent electrodes and the liquid crystal layers because of differences in the refractive indices. Since the exact optical pathlength of the resulting Fabry-Pérot cavity varies for every applied phase and thereby, for every single pixel depending on the applied pulse shape, the resulting deviations in shaped phase and amplitude cannot easily be compensated for by the pulse-shaper calibration. Therefore, the voltages of one LCD layer were scanned in intervals around the values for maximal and minimal transmission found by the initial phase calibration for different absolute phase values of the other LCD layer. Systematic deviations between expected and measured voltage-to-phase dependencies could thereby be individually corrected for each pixel by this constant voltage correction further described in Section 2.13.2, minimizing the average deviation. A full two-dimensional voltage correction as proposed in Section 2.13.3 includes iterative optimization for every possible phase combination and thereby pulse shape. Furthermore, the measurement of the complex electric fields instead of the intensity would further improve the pulse-shaper correction process.

Due to the immense time and computational resource consumption of a full correction and the absence of an experimental implementation for full phase-retrieval of shaped pulses, only the constant voltage correction from transmission measurements was applied

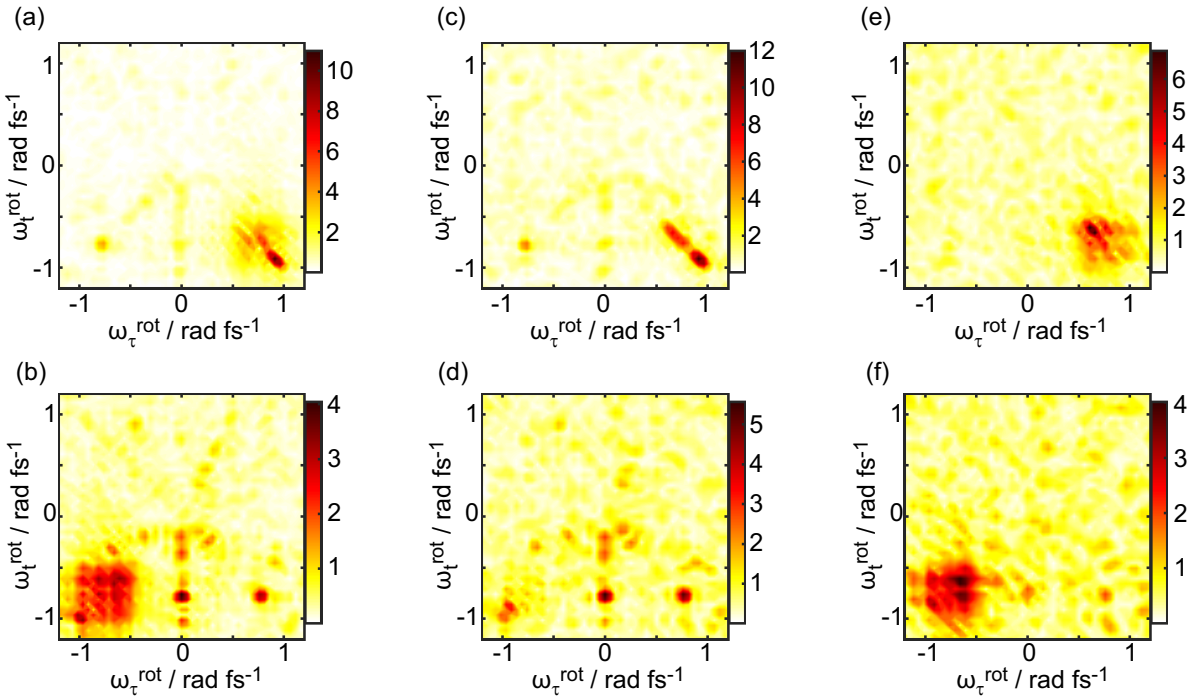

Figure 4.5 | Zero-padded rephasing (upper row) and non-rephasing (lower row) 2D spectra before the final processing step. The high-power measurements (a,b) contain the expected nonlinear signals in the lower right (a) and lower left (b) quadrants. Additional artifacts occur in other positions. For low-power measurements (c,d), only the linear artifacts remain, allowing for an artifact correction. The correction is done by subtracting the measured low-power from the high-power maps in the time domain (not shown). The corrected 2D maps are then retrieved by Fourier transformation, from which the absolute values are shown (e,f). Figure adapted from Ref. [1].

here. However, further improvements of the experimental setup will allow for a full voltage correction in the near future. To sum up, by using a low-voltage working range to reduce pixel crosstalk and an additional calibration step to minimize the average phase deviation individually for each LCD pixel, the pulse-shaper imperfections can be significantly reduced with reasonable effort.

Note that the described challenges are in principle present in many pulse-shaping applications. However, when dealing with conventional pump-probe-type or quantum control experiments, these artifacts are in general not so critical and thus often remain unnoticed because tiny deviations from the desired pulse shape will not have a significant influence on the observed dynamics. Here, on the other hand, the retrieval of the nonlinear signal component relies on its separation from a strong linear fluorescence background [compare Fig. 4.4(b)], and thus even small deviations from the target pulse shape must be suitably addressed. For the measurements shown in Fig. 4.5, the described pulse-shaper calibration procedure is already implemented, and the features seen in Fig. 4.5(c) and 4.5(d) are what remains.

Now the amplitude of the artifacts is low enough that the residual linear contributions can be removed. The measured time-domain maps have been normalized to the laser power, therefore linear contributions can be removed from the individual time-domain

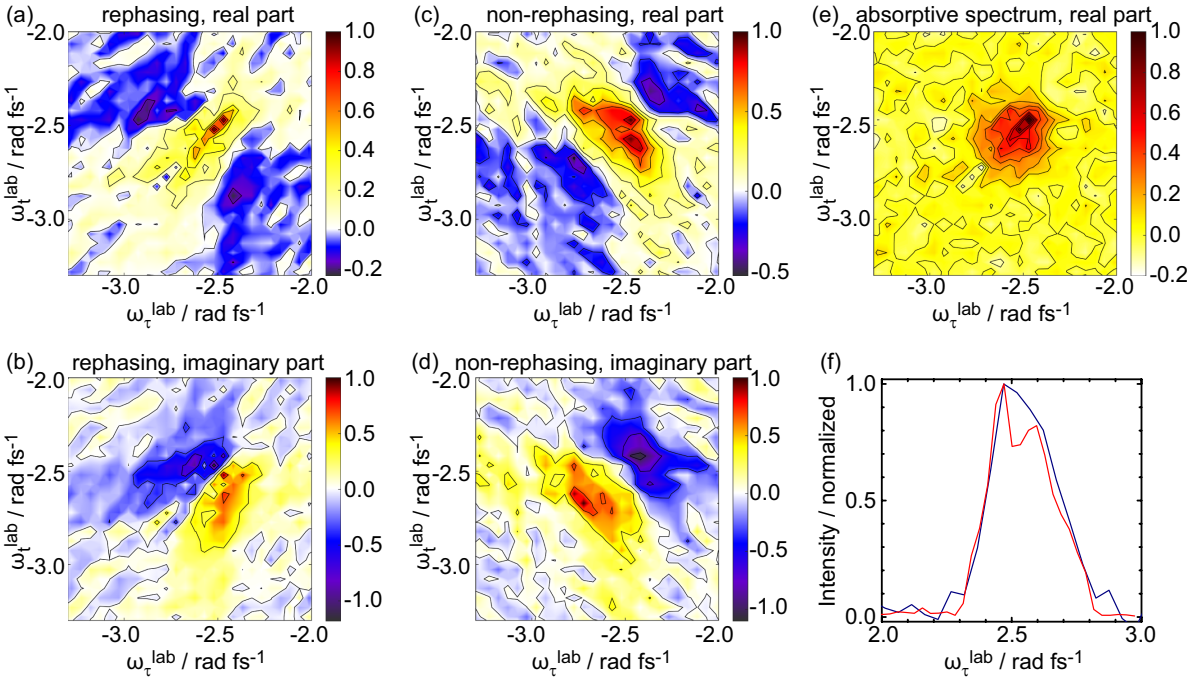

Figure 4.6 | Final 2D spectrum of a hotspot in the nanostructured F_{16}ZnPc pillar array. The complex-valued maps are shown for the rephasing (a) real and (b) imaginary part as well as the non-rephasing (d) real and (e) imaginary part. The real-valued maps are added to obtain (e) the absorptive spectrum. (f) Projection of the 2D absorptive spectrum onto the ω_t axis (black) compared to a separately measured Fourier-transformed linear two-pulse scan (red). Figure adapted from Ref. [1].

maps by subtraction of the low-excitation-power map from the corresponding high-power map.

Note that, as opposed to four-wave-mixing-detected 2D spectroscopy using a local oscillator for phase recovery, data analysis of spectral interferograms via a Fourier-transformation procedure is not required. Thus no Fourier windowing effects need to be considered. Instead, the full time-integrated and spectrally integrated fluorescence is used. After subsequent phase cycling of the 27 time maps and two-dimensional Fourier transformation, the corrected rephasing and non-rephasing 2D spectra shown in Fig. 4.5(e) and 4.5(f) are obtained.

Detailed views of the real parts of the relevant quadrants of the corrected 2D maps of Fig. 4.5(e) and 4.5(f) are shown in Fig. 4.6(a, rephasing) and 4.6(c, non-rephasing), respectively, and the corresponding imaginary parts are plotted in Fig. 4.6(b) and 4.6(d). The axes have been converted from the partially rotating frame frequencies ω^{rot} used above to the laboratory frame frequencies ω^{lab} by adding $\Delta\omega = 0.7\ \omega_0$. Adding up the rephasing and the non-rephasing real-valued contributions, the absorptive 2D spectrum is retrieved [Fig. 4.6(e)]. This spectrum allows for comparison with 2D measurements in non-collinear box or pump-probe geometry. However, the latter are lacking the spatial resolution needed for investigation of structures heterogeneous on the sub-micron scale. To verify the integrity of the obtained 2D spectra, the absorptive spectrum is integrated along the ω_τ axis [Fig. 4.6(f, black)]. For comparison, the linear fluorescence of the in-

plane structured F_{16}ZnPc pillar array is measured with a two-pulse delay scan (τ scanned from -100 fs to 100 fs in 1 fs steps) and subsequent Fourier transformation [Fig. 4.6(f, red)]. The two spectra show the same spectral bandwidth and ratio of the two distinct peaks, with the local minimum between the two peaks being more pronounced in the spectrum obtained by the two-pulse scan because of the better signal-to-noise ratio compared to the full 2D spectrum. The satisfactory agreement between the two curves is a validation of the new method.

To sum up, the novel method of coherent 2D fluorescence micro-spectroscopy was developed, which makes it possible to probe the nonlinear response of fluorescent laterally heterogeneous thin films with diffraction-limited spatial resolution (NA = 1.4, in our case corrsponding to a resolution of 260 nm). The method was exemplified on a nanostructured array of F_{16}ZnPc pillars. The rephasing, non-rephasing, and absorptive 2D spectra were extracted from the collinearly measured data by 27-step phase cycling.

This scheme can be expanded to probe molecular dynamics in more detail by additional scanning of the population time T. Ansiotropy measurements of crystalline domains with different orientation can be carried out by rotating the polarization of the exciting light pulses. With the help of a second microscope objective, light emitted from the sample in transmission direction can be collected, thus enabling additional capture of absorptive (rather than fluorescence-detected) 2D spectra. The rephasing, non-rephasing and absorptive contributions from both observables, incoherent fluorescence and coherent absorption, could even be collected simultaneously in a single measurement.

Most importantly, already with the toolkit presented here, spatial variations of the nonlinear response in chromophore systems and couplings to other systems in their vicinity can be measured all-optically with sub-micron resolution.

5 Summary

Aiming for optical investigations while simultaneously approaching the physical limits on the length and timescale, an experimental setup for probing ultrafast dynamics at the diffraction limit was developed, characterized and demonstrated in the scope of this thesis.

In Chapter 2, an overview of this experimental setup was given as well as the considerations that led to the selection of the individual components. Broadband laser pulses with a length of 9.3 fs, close to the transform limit of 7.6 fs, were focused in a NA = 1.4 immersion oil objective, to the diffraction limit of below 300 nm (FWHM). Dispersion, mainly introduced by the transmissive optics, was partially pre-compensated by chirped mirrors with the remaining dispersion being compensated by a $4f$ LCD pulse shaper. The latter utilized the PRISM algorithm with nonlinear feedback from a two-photon photo-diode in the microscope focus.

To ensure the full functionality of the experimental setup for arbitrary phase and amplitude shaped pulses, methods for probing and optimizing the temporal, spectral and spatial shape of the laser focus were developed. The spatial focus shape was characterized with off-resonance gold nanorod scatterers scanned through the focal volume. By incoupling optimization with the help of spectrally resolved amplitude and phase mapping, deviations of the wavelength-dependent focus position were reduced to less than 10 nm. Furthermore, spectral interference measurements allowed to narrow down the spectrally dependent pulse-arrival time variation to within 1 fs across the focal plane. The influence of the pulse shaper on the spatial and spectral shape of the focus was categorized as minor, confirming it did not perceptibly alter the outcome of the presented experiments.

For further insights into the functionality and limitations of the pulse shaper, its calibration procedure was reviewed. Crucial aspects in all calibration steps were emphasized, including data acquisition, wavelength calibration, reconstruction of the phase-to-voltage curves, and the selection of the used voltage range. The deviations between designed and experimental pulse shapes were attributed to pulse-shaper artifacts, including voltage-dependent inter-layer as well as intra-layer LCD-pixel crosstalk, Fabry-Pérot-type reflections in the LCD layers, and space-time coupling. The impact of these artifacts inherent to LCD-based pulse shapers, especially of pixel crosstalk and Fabry-Pérot-type reflections, could be significantly reduced by refinements of the calibration. For every pulse-shaper pixel, the actual experimental transmission extrema values were systematically mapped, including the influence of inter-layer crosstalk. A pixel-dependent correction was experimentally carried out, which can be seen as an extension of the initial calibration to all possible voltage combinations of the two LCD layers.

After characterization and optimization of the experimental setup, its capabilities were demonstrated in two types of experiments, targeting the nonlinearity of gold (Chapter 3) as well as two-dimensional spectroscopy at micro-structured surfaces (Chapter 4). The

experimental determination of the nonlinear refractive index n_2 of gold was pursued first by utilizing self-focusing due to the optical Kerr effect. An experimental z-scan setup was built for this purpose and its functionality was demonstrated by the determination of $\mathrm{Re}(n_2) = n_2' = 2.9 \cdot 10^{-20}$ m^2/W from a 170 μm thick fused silica layer, a result consistent with previous reports in literature. In z-scans on a 63-nm-thin single-crystalline gold film, no nonlinear behavior above the noise floor could be observed. Thereby, an upper bound for the absolute value for the imaginary part of the nonlinear refractive index could be set to $|n_2''\,(\mathrm{Au})| < 0.6 \cdot 10^{-16}$ m^2/W. The gold film was damaged after multiple measurements, the used peak intensity of 0.22 TW/cm^2 was therefore determined as the damage threshold. As a result, an upper bound for the absolute value of n_2' was set to $|n_2'\,(\mathrm{Au})| < 1.2 \cdot 10^{-16}$ m^2/W.

In addition to the nonlinear refractive index in thin films, the relative phase change of propagating plasmonic eigenmodes in nanointerferometers was experimentally investigated. Finite-difference time-domain simulations indicated the feasibility of active plasmonic nanocircuitry, but accurate predictions rely on the exact knowledge of the nonlinear properties of the materials involved. Top-down fabricated, y-shaped gold nanostructures were chosen since their nonlinear response would intrinsically resemble a logic switch. The spatial contrast between the two output ports was observed, where an intensity-dependent variation due to the relative phase change between the two eigenmodes is expected. Simulations indicated that a phase change of $\Delta\Phi \geq 0.07$ rad between the plasmonic modes would induce a sufficient change in spatial contrast to be visible in the experiment. As the latter could not be observed, this value of $\Delta\Phi$ was determined as the upper bound for the experimentally induced phase change. Successive, irreversible changes in the spatial contrast measurements could be explained by gradual degradation of the incoupling antennas confirmed by SEM measurements. For the damage threshold of the gold nanostructures, an upper bound of 52 GW/cm^2 was thereby found.

In the final Chapter 4, a novel method for nonlinear spectroscopy on surfaces was presented. Termed coherent two-dimensional fluorescence micro-spectroscopy, it is capable of exploring ultrafast dynamics in nanostructures and molecular systems at the diffraction limit. Two-dimensional spectra of spatially isolated hotspots in structured thin films were taken by scanning the temporal delays of a collinear four-pulse train in combination with a 27-step phase-cycling scheme. Fluorinated zinc phthalocyanine (F_{16}ZnPc) dye was chosen as reference system due to its high fluorescence yield and photostability. The reflection and fluorescence of the structured hexagonal-ordered lattice of F_{16}ZnPc nanopillars was mapped with diffraction-limited spatial resolution. The absorptive spectra could be retrieved from the 2D maps, which were acquired from a single hotspot at a peak intensity of 65 GW/cm^2. The 2D measurements were repeated in the linear regime on the same sample position, at a low peak excitation power of 3.5 GW/cm^2. By subtracting the linear maps from the high-power measurements, linear artifacts were separated from the nonlinear sample response. The artifacts were identified as a consequence from residual deviations between the desired and the experimental pulse shapes.

The optimization procedures described in Chapter 2 successfully suppressed the deviations to a level where the separation from the nonlinear sample response was feasible. Control measurements of a linear fluorescence spectrum by a two-pulse scan confirmed the validity of the result from the corrected nonlinear 2D map.

The newly developed method of spectroscopy supplements the available tools for observation of ultrafast dynamics of molecular and other microscopic systems. Hence, spatial variations of dynamics in the visible and near infrared spectral regime can be investigated with sub-micron resolution by all-optical methods. Comparison to 2D spectroscopy in the liquid phase yields additional information on the coupling of the chromophores to their local surroundings as well as the impact of the reduced degrees of freedom on their functionality.

The experimental setup and methods developed and presented in the scope of this thesis demonstrate its flexibility and capability to study microscopic systems on surfaces. The systems exemplarily shown are consisting of metal-organic dyes and metallic nanostructures, represent samples currently under research in the growing fields of organic semiconductors and plasmonics. Ongoing interest in the development of microstructures, nanostructures and two-dimensional surface systems consisting of a steadily rising amount of material classes are waiting to have their inner workings unraveled. The experimental tool kit presented here is a major contribution to explore dynamics approaching the physical limits both in the temporal and the spatial domain.

6 Zusammenfassung

Die hier vorgestellte Arbeit hatte zum Ziel, im Rahmen von optischen Beobachtungen gleichzeitig an die physikalischen Grenzen von Längen- und Zeitskalen zu gehen. Dafür wurde ein experimenteller Aufbau zur Untersuchung von ultraschnellen Dynamiken am Beugungslimit entwickelt, charakterisiert und demonstriert.

In Kapitel 2 wurde ein Überblick über den verwendeten experimentellen Aufbau gegeben, zusammen mit den Überlegungen, die zur Auswahl der einzelnen Komponenten geführt haben. Es wurde für die spektral breitbandigen Laserpulse eine Pulslänge von 9.3 fs gemessen, welche nahe an der transformlimitierten Dauer von 7.6 fs liegt. Im beugungslimitierten Fokus eines Immersionsölobjektivs mit einer numerischen Apertur von 1.4 konnte das Licht räumlich auf eine Halbwertsbreite von unter 300 nm komprimiert werden. Ein Teil der spektralen Dispersion wurde durch dispersive Spiegel vorkompensiert. Die verbleibende Dispersion wurde mit einem LCD-Pulsformer in $4f$-Geometrie unter Verwendung des PRISM Algorithmus ermittelt und ebenfalls kompensiert. Dabei wurde das nichtlineare Signal einer Zweiphotonenphotodiode direkt aus dem Fokus des Mikroskopobjektivs ausgelesen.

Um die volle Funktionalität des Aufbaus für beliebige phasen- und amplitudengeformte Laserpulse zu gewährleisten, wurden Methoden zur Untersuchung und Optimierung der zeitlichen, spektralen und räumlichen Struktur des Laserfokus entwickelt. Der Fokus des Mikroskopobjektivs wurde mit Hilfe der Streuung von nicht resonanten Nanopartikeln aus Gold ausgemessen, indem diese räumlich durch den Fokus gerastert wurden. Durch Messungen der spektralen Amplitude und Phase konnte die Einkopplung des Laserstrahls in das Objektiv optimiert werden. Die Messungen ergaben, dass die räumliche Schwankung der spektralen Anteile für die Bereiche relevanter spektraler Intensität unter 10 nm beträgt. Weiterhin wurde durch Messungen der spektralen Interferenz festgestellt, dass die Schwankungen der Pulsankunftszeit im Fokus über das gesamte Spektrum unter 1 fs liegen. Der Einfluss des Pulsformers auf die spektrale und räumliche Verteilung im Fokus konnte als minimal eingestuft werden. Somit wurde sichergestellt, dass die durchgeführten Experimente dadurch nicht merklich beeinflusst wurden.

Zur weiteren Untersuchung des Funktionsumfangs und der Grenzen des benutzten Pulsformers wurde dessen Eichprozedur geprüft. Der Schwerpunkt lag dabei auf den kritischen Aspekten aller Eichungsschritte: Von der Datenaufnahme über die Wellenlängenkalibrierung und die Rekonstruktion der spannungsabhängigen Phasenkurven zu der Auswahl des tatsächlich verwendeten Spannungsbereichs. Die Abweichungen zwischen gewünschten und tatsächlich angelegten Pulsformen wurden auf Artefakte des Pulsformers zurückgeführt. Diese Artefakte beinhalten eine spannungsabhängige Beeinflussung der LCD-Pixel sowohl zwischen benachbarten Pixeln einer Schicht, als auch zwischen Pixeln unterschiedlicher Schichten. Als weitere Einflussfaktoren wurden neben der raumzeitlichen Kopplung auch Fabry-Pérot-artige Reflektionen innerhalb der LCD-Schichten identifiziert. Die Auswirkungen dieser für LCD-Pulsformer inhärenten

Artefakte, speziell von der gegenseitigen Beeinflussung der Pixel und von Fabry-Pérot-typischen Reflektionen, konnten durch nachträgliche Verbesserungen der Kalibrierung deutlich reduziert werden. Für jedes Pixel des Pulsformers wurden die tatsächlichen Extremwerte der Transmission experimentell ermittelt, inklusive des Einflusses der Wechselwirkung zwischen den beiden LCD-Schichten. Eine pixelabhängige Korrektur wurde implementiert, die eine Erweiterung der ursprünglichen Kalibrierung auf alle möglichen Spannungskombinationen der LCD-Pixel darstellt.

Um die Möglichkeiten des charakterisierten und optimierten experimentellen Aufbaus zu demonstrieren, wurden zwei Arten von Experimenten durchgeführt: Messungen zur Bestimmung des nichtlinearen Brechungsindexes von Gold (Kapitel 3) sowie zweidimensionale Spektroskopie an mikrostrukturierten Oberflächen (Kapitel 4).

Die experimentelle Untersuchung des nichtlinearen Brechungsindexes n_2 von Gold erfolgte zunächst durch die Ausnutzung von Selbstfokussierung auf Basis des optischen Kerr-Effekts. Dafür wurde ein Aufbau zur Durchführung von z-Scans realisiert, dessen Funktionalität durch die Bestimmung von $\mathrm{Re}(n_2) = n_2' = 2.9 \cdot 10^{-20}$ m^2/W an einer 170 μm dicken Schicht aus Quarzglas demonstriert wurde. Dieser Wert ist mit früheren Messungen aus der Literatur vereinbar.

Durch z-Scans an einem Dünnfilm aus Gold mit der Dicke von 63 nm konnte kein nichtlineares Verhalten oberhalb des Rauschniveaus beobachtet werden. Dadurch konnte für den Imaginärteil des nichtlinearen Brechungsindexes von Gold eine obere Grenze von $|n_2''\,(\mathrm{Au})| < 0.6 \cdot 10^{-16}$ m^2/W festgesetzt werden. Nach mehreren Messreihen wurde eine Beschädigung des Goldfilms festgestellt. Die dabei verwendete Maximalintensität von 0.22 TW/cm^2 konnte deshalb als Zerstörschwelle ermittelt werden. Des Weiteren konnte der Betrag von n_2' auf eine obere Grenze von $|n_2'\,(\mathrm{Au})| < 1.2 \cdot 10^{-16}$ m^2/W festgesetzt werden.

Zusätzlich zur Untersuchung des nichtlinearen Brechungsindexes an Dünnschichten wurde die relative Phasenänderung zwischen zwei Eigenmoden eines plasmonischen Nanointerferometers untersucht. Simulationen mit der Finite-Differenzen-Methode deuteten darauf hin, dass plasmonische Nanoschaltkreise realisierbar sind. Präzise Aussagen können allerdings nur mit Kenntnis der nichtlinearen Eigenschaften zugrunde liegender Materialien gemacht werden. Zur Untersuchung der nichtlinearen Eigenschaften wurden im „top-down“-Verfahren hergestellte, Y-förmige Nanostrukturen aus Gold ausgewählt, da diese die Funktionalität eines logischen Schalters besitzen. Der Kontrast zwischen den Emissionen zweier räumlich separierten Ausgängen der Nanostrukturen wurde beobachtet. Dabei sind durch die relative Phasenänderung zweier plasmonischer Eigenmoden intensitätsabhängige Kontrastveränderungen zu erwarten. Simulationen zeigten, dass eine Phasenänderung von $\Delta\Phi \geq 0.07$ rad zwischen den plasmonischen Moden ausreichend für eine experimentell sichtbare Kontraständerung wäre. Da letztere nicht beobachtet werden konnte, wurde dieser Wert für $\Delta\Phi$ als obere Grenze für die experimentell eingeführte Phasenänderung festgesetzt. Sukzessive, irreversible Änderungen in den Messungen des räumlichen Kontrasts konnten durch schrittweise Degradierung der Einkoppelantennen erklärt werden, was durch SEM Messungen bestätigt werden konnte. Für die Zerstörschwelle der Gold-Nanostrukturen wurde damit eine obere Grenze von 52 GW/cm^2 gefunden.

Im letzten Kapitel der Arbeit, Kapitel 4, wurde eine neue Methode für nichtlineare Spektroskopie an Oberflächen vorgestellt. Sie trägt den Namen „Kohärente zweidimen-

sionale Fluoreszenz-Mikrospektroskopie“und eignet sich zur Untersuchung ultraschneller Dynamiken in Nanostrukturen und molekularen Systemen am Beugungslimit. Es wurden 2D-Spektren von räumlich isolierten Hotspots einer strukturierten Dünnschicht aufgenommen. Es erfolgte eine Variation der zeitlichen Abstände zwischen den Pulsen einer Vierpulssequenz in Kombination mit 27-fachem Phasecycling. Als Referenzsystem wurde Zink-Phthalocyanin (F_{16}ZnPc) ausgewählt, da es eine hohe Fluoreszenzquantenausbeute und Photostabilität besitzt. Die Messung der Reflektion und der Fluoreszenz eines hexagonal strukturierten Gitters aus F_{16}ZnPc Nanosäulen erfolgte mit beugungslimitierter Auflösung.

Aus den 2D-Karten, gemessen mit einer Maximalintensitäten von 65 GW/cm^2, konnten die absorptiven Spektren einzelner Hotspots ermittelt werden. Die 2D-Messungen wurden an der gleichen Position auf der Probe im linearen Regime bei einer geringen Maximalintensität von 3.5 GW/cm^2 wiederholt. Durch Subtraktion der linearen Karten von den bei hoher Intensität gemessenen Karten konnten lineare Artefakte von der nichtlinearen Antwort der Probe getrennt werden. Die verbleibenden Abweichungen zwischen gewünschten und experimentellen Pulsformen wurden als Grund für die Artefakte identifiziert. Durch die in Kapitel 2 vorgestellten Optimierungen konnten die Abweichungen allerdings so stark reduziert werden, dass deren Trennung von der nichtlinearen Antwort der Probe möglich wurde. Als Kontrollmessung wurde das lineare Fluoreszenzspektrum der Probe aus einem Zweipulsscan ermittelt. Der Vergleich mit dem Ergebnis der korrigierten nichtlinearen 2D-Karte bestätigt dessen Validität.

Die neu entwickelte Spektroskopiemethode ergänzt bestehende Möglichkeiten zur Beobachtung von ultraschnellen Dynamiken molekularer und anderer mikroskopischer Systeme. Die räumliche Abhängigkeit von Dynamiken im sichtbaren und nahinfraroten Spektralbereich kann damit, mit einer räumlicher Äuflösung von unter einem Mikrometer, mit rein optischen Mitteln untersucht werden. Durch den Vergleich mit 2D-Messungen in der flüssigen Phase können weitere Erkenntnisse über die Kopplung der Chromophoren mit ihrer lokalen Umgebung sowie den Einfluss der reduzierten Anzahl an Freiheitsgraden auf die Funktionalität gewonnen werden.

Die Flexibilität und der Funktionsumfang zur Analyse mikroskopischer Systeme der im Rahmen dieser Arbeit entwickelten experimentellen Aufbauten und Methoden wurde demonstriert. Repräsentativ für die wachsenden Forschungsfelder der organischen Halbleiter und der Plasmonik wurden exemplarisch Systeme bestehend aus metall-organischen Farbstoffen und metallischen Nanostrukturen untersucht.

Es besteht anhaltendes Interesse an der Entwicklung von Mikrostrukturen, Nanostrukturen und zwei-dimensionalen Oberflächensystemen, aufgebaut aus einer stetig wachsenden Anzahl an Materialklassen. Diese Systeme warten darauf, dass ihre innere Funktionsweise entschlüsselt wird. Die Entwickling der hier vorgestellten Werkzeuge liefert einen wesentlichen Beitrag zur Untersuchung von Dynamiken, die sich sowohl in der zeitlichen als auch in der räumlichen Domäne an die physikalischen Grenzen befinden.

List of Abbreviations

2D	two-dimensional
3D	three-dimensional
AFM	atomic force microscopy
AOM	acousto-optic modulator
APD	avalanche photodiode
AWG	acoustic wave generator
BBO	β-barium borate
BS	beamsplitter
CCD	charge-coupled device
CEP	carrier-envelope phase
CMOS	complementary metal-oxide-semiconductor
D	downwards
DBS	dichroic beamsplitter
DCM	double-chirped mirror
DG	diffraction grating
FDTD	finite-difference time-domain
FM	focusing mirror
FlM	flip mirror
FROG	frequency-resolved optical gating
FWHM	full width at half maximum
G	ground glass plate
HR	high-reflection
iAC	interferometric autocorrelation
ID	iris diaphragm
ITO	indium tin oxide
L	lens
LCD	liquid-crystal display
LP	long-pass
MIIPS	multiphoton intrapulse interference phase scan

NA	numerical aperture
ND	neutral density
NIR	near-infrared
NSOM	near-field scanning optical microscopy
OD	optical density
P	polarizer
PEEM	photoemission electron microscopy
PH	pinhole
PMT	photomultiplier tube
PRISM	phase-resolved interferometric spectral modulation
PSM	piezo scanning mirror
SC	spatial contrast
SEA TADPOLE	spatially encoded arrangement for temporal analysis by dispersing a pair of light E-fields
SEM	scanning electron microscopy
SHG	second harmonic generation
SLM	spatial light modulator
SP	short-pass
SPIDER	spectral phase interferometry for direct electric-field reconstruction
T	transmission
TPPD	two-photon photodiode
U	upwards
UV	ultraviolet
Vis	visible

Bibliography

[1] S. Goetz, D. Li, V. Kolb, J. Pflaum, and T. Brixner.
Coherent two-dimensional fluorescence micro-spectroscopy.
Opt. Express **26**, 3915–3925 (2018).

[2] S. Goetz, G. Razinskas, E. Krauss, C. Dreher, M. Wurdack, P. Geisler, M. Pawłowska, B. Hecht, and T. Brixner.
Investigation of the nonlinear refractive index of single-crystalline thin gold films and plasmonic nanostructures.
Appl. Phys. B **122**, 1–10 (2016).

[3] M. Pawłowska, S. Goetz, C. Dreher, M. Wurdack, E. Krauss, G. Razinskas, P. Geisler, B. Hecht, and T. Brixner.
Shaping and spatiotemporal characterization of sub-10-fs pulses focused by a high-NA objective.
Opt. Express **22**, 31496–31510 (2014).

[4] C. Rewitz, G. Razinskas, P. Geisler, E. Krauss, S. Goetz, M. Pawłowska, B. Hecht, and T. Brixner.
Coherent control of plasmon propagation in a nanocircuit.
Phys. Rev. Applied **1**, 014007 (2014).

[5] P. Geisler, G. Razinskas, E. Krauss, X.-F. Wu, C. Rewitz, P. Tuchscherer, S. Goetz, C.-B. Huang, T. Brixner, and B. Hecht.
Multimode plasmon excitation and insitu analysis in top-down fabricated nanocircuits.
Phys. Rev. Lett. **111**, 183901 (2013).

[6] R. Hooke.
Micrographia.
Royal Society of London (1665).

[7] W. J. Croft.
Under the microscope: A brief history of microscopy.
World Scientific Publishing Company (2006).

[8] S. Bradbury.
The evolution of the microscope.
First edition. Pergamon (1967).

[9] E. Abbe.
Beiträge zur Theorie des Mikroskops und der mikroskopischen Wahrnehmung: I. Die Construction von Mikroskopen auf Grund der Theorie.
Archiv für Mikroskopische Anatomie **9**, 413–418 (1873).

[10] G. Porter.
Flash photolysis and spectroscopy. A new method for the study of free radical reactions.
Proc. R. Soc. Lond., Ser. A **200**, 284–300 (1950).

[11] R. G. Gould.
The LASER, light amplification by stimulated emission of radiation.
The Ann Arbor Conference on Optical Pumping, the University of Michigan **15**, 128 (1959).

[12] T. H. Maiman.
Stimulated optical radiation in ruby.
Nature **187**, 493–494 (1960).

[13] M. Göppert-Mayer.
Über Elementarakte mit zwei Quantensprüngen.
Ann. Phys. **401**, 273–294 (1931).

[14] W. Kaiser and C. G. B. Garrett.
Two-photon excitation in CaF_2: Eu^{2+}.
Phys. Rev. Lett. **7**, 229–231 (1961).

[15] C. V. Shank.
Investigation of ultrafast phenomena in the femtosecond time domain.
Science **233**, 1276–1280 (1986).

[16] D. E. Spence, P. N. Kean, and W. Sibbett.
60-fsec pulse generation from a self-mode-locked Ti:sapphire laser.
Opt. Lett. **16**, 42–44 (1991).

[17] A. M. Weiner, J. P. Heritage, and E. M. Kirschner.
High-resolution femtosecond pulse shaping.
J. Opt. Soc. Am. B **5**, 1563–1572 (1988).

[18] A. M. Weiner.
Femtosecond optical pulse shaping and processing.
Prog. Quantum Electron. **19**, 161–237 (1995).

[19] A. H. Zewail.
Laser femtochemistry.
Science **242**, 1645–1653 (1988).

[20] A. H. Zewail.
Femtochemistry: Atomic-scale dynamics of the chemical bond.
J. Phys. Chem. A **104**, 5660–5694 (2000).

[21] W. Denk, J. H. Strickler, and W. W. Webb.
Two-photon laser scanning fluorescence microscopy.
Science **248**, 73–76 (1990).

[22] M. Minsky.
Memoir on inventing the confocal scanning microscope.
Scanning **10**, 128–138 (1988).

[23] W. J. Padilla, D. N. Basov, and D. R. Smith.
Negative refractive index metamaterials.
Mater. Today **9**, 28–35 (2006).

[24] F. J. McClung and R. W. Hellwarth.
Giant optical pulsations from ruby.
J. Appl. Phys. **33**, 828–829 (1962).

[25] L. E. Hargrove, R. L. Fork, and M. A. Pollack.
Locking of HeNe laser modes induced by synchronous intracavity modulation.
Appl. Phys. Lett. **5**, 4–5 (1964).

[26] M. T. Asaki, C.-P. Huang, D. Garvey, J. Zhou, H. C. Kapteyn, and M. M. Murnane.
Generation of 11-fs pulses from a self-mode-locked Ti:sapphire laser.
Opt. Lett. **18**, 977–979 (1993).

[27] J. Zhou, G. Taft, C.-P. Huang, M. M. Murnane, H. C. Kapteyn, and I. P. Christov.
Pulse evolution in a broad-bandwidth Ti:sapphire laser.
Opt. Lett. **19**, 1149–1151 (1994).

[28] A. Stingl, M. Lenzner, C. Spielmann, F. Krausz, and R. Szipöcs.
Sub-10-fs mirror-dispersion-controlled Ti:sapphire laser (1995).

[29] U. Morgner, F. X. Kärtner, S. H. Cho, Y. Chen, H. A. Haus, J. G. Fujimoto, E. P. Ippen, V. Scheuer, G. Angelow, and T. Tschudi.
Sub-two-cycle pulses from a Kerr-lens mode-locked Ti:sapphire laser.
Opt. Lett. **24**, 411–413 (1999).

[30] Y. Barad, H. Eisenberg, M. Horowitz, and Y. Silberberg.
Nonlinear scanning laser microscopy by third harmonic generation.
Appl. Phys. Lett. **70**, 922–924 (1997).

[31] A. Zumbusch, G. R. Holtom, and X. S. Xie.
Three-dimensional vibrational imaging by coherent anti-Stokes Raman scattering.
Phys. Rev. Lett. **82**, 4142–4145 (1999).

[32] N. Dudovich, D. Oron, and Y. Silberberg.
Single-pulse coherently controlled nonlinear Raman spectroscopy and microscopy.
Nature **418**, 512–514 (2002).

[33] W. R. Zipfel, R. M. Williams, and W. W. Webb.
Nonlinear magic: multiphoton microscopy in the biosciences.
Nat Biotechnol **21**, 1369–1377 (2003).

[34] J. Mertz.
Nonlinear microscopy: new techniques and applications.
Curr Opin Neurobiol **14**, 610–616 (2004).

[35] F. Helmchen and W. Denk.
Deep tissue two-photon microscopy.
Nat. Meth. **2**, 932–940 (2005).

[36] J. B. Pawley (Ed.).
Handbook of biological confocal microscopy.
Springer US, Boston, MA (2006).

[37] R. Berera, R. v. Grondelle, and J. T. M. Kennis.
Ultrafast transient absorption spectroscopy: principles and application to photosynthetic systems.
Photosynth. Res. **101**, 105–118 (2009).

[38] S. Woutersen and P. Hamm.
Nonlinear two-dimensional vibrational spectroscopy of peptides.
J. Phys.: Condens. Matter **14**, R1035 (2002).

[39] L. W. Barbour, M. Hegadorn, and J. B. Asbury.
Watching electrons move in real time: ultrafast infrared spectroscopy of a polymer blend photovoltaic material.
JACS **129**, 15884–15894 (2007).

[40] W. Xiong, J. E. Laaser, R. D. Mehlenbacher, and M. T. Zanni.
Adding a dimension to the infrared spectra of interfaces using heterodyne detected 2D sum-frequency generation (HD 2D SFG) spectroscopy.
PNAS **108**, 20902–20907 (2011).

[41] J. E. Laaser and M. T. Zanni.
Extracting structural information from the polarization dependence of one- and two-dimensional sum frequency generation spectra.
J. Phys. Chem. A **117**, 5875–5890 (2013).

[42] J. E. Laaser, D. R. Skoff, J.-J. Ho, Y. Joo, A. L. Serrano, J. D. Steinkruger, P. Gopalan, S. H. Gellman, and M. T. Zanni.
Two-dimensional sum-frequency generation reveals structure and dynamics of a surface-bound peptide.
JACS **136**, 956–962 (2014).

[43] P. C. Chen.
An introduction to coherent multidimensional spectroscopy.
Appl. Spectrosc. **70**, 1937–1951 (2016).

[44] J. P. Ogilvie and K. J. Kubarych.
Multidimensional electronic and vibrational spectroscopy: An ultrafast probe of molecular relaxation and reaction dynamics.
Adv. At. Mol. Opt. Phys. **57**, 249–321 (2009).

[45] P. Hamm and M. Zanni.
Concepts and methods of 2D infrared spectroscopy.
First edition. Cambridge University Press, New York (2011).

[46] A. Assion, M. Geisler, J. Helbing, V. Seyfried, and T. Baumert.
Femtosecond pump-probe photoelectron spectroscopy: mapping of vibrational wave-packet motion.
Phys. Rev. A **54**, R4605–R4608 (1996).

[47] S. Ruetzel, M. Diekmann, P. Nuernberger, C. Walter, B. Engels, and T. Brixner.
Multidimensional spectroscopy of photoreactivity.
PNAS **111**, 4764–4769 (2014).

[48] A. Assion, T. Baumert, M. Bergt, T. Brixner, B. Kiefer, V. Seyfried, M. Strehle, and G. Gerber.
Control of chemical reactions by feedback-optimized phase-shaped femtosecond laser pulses.
Science **282**, 919–922 (1998).

[49] P. Nuernberger, G. Vogt, T. Brixner, and G. Gerber.
Femtosecond quantum control of molecular dynamics in the condensed phase.
Phys. Chem. Chem. Phys. **9**, 2470–2497 (2007).

[50] M. Aeschlimann, M. Bauer, D. Bayer, T. Brixner, F. J. Garca de Abajo, W. Pfeiffer, M. Rohmer, C. Spindler, and F. Steeb.
Adaptive subwavelength control of nano-optical fields.
Nature **446**, 301–304 (2007).

[51] Y. Silberberg.
Quantum coherent control for nonlinear spectroscopy and microscopy.
Annu. Rev. Phys. Chem. **60**, 277–292 (2009).

[52] H. Kawashima, M. M. Wefers, and K. A. Nelson.
Femtosecond pulse shaping, multiple-pulse spectroscopy, and optical control.
Annu. Rev. Phys. Chem. **46**, 627–656 (1995).

[53] A. M. Weiner.
Femtosecond pulse shaping using spatial light modulators.
Rev. Sci. Instrum. **71**, 1929–1960 (2000).

[54] A. M. Weiner.
Ultrafast optical pulse shaping: a tutorial review.
Opt. Commun. **284**, 3669–3692 (2011).

[55] I. Pastirk, J. Dela Cruz, K. Walowicz, V. Lozovoy, and M. Dantus.
Selective two-photon microscopy with shaped femtosecond pulses.
Opt. Express **11**, 1695–1701 (2003).

[56] N. Accanto, L. Piatkowski, J. Renger, and N. F. van Hulst.
Capturing the optical phase response of nanoantennas by coherent second-harmonic microscopy.
Nano Lett. **14**, 4078–4082 (2014).

[57] N. Accanto, J. B. Nieder, L. Piatkowski, M. Castro-Lopez, F. Pastorelli, D. Brinks, and N. F. van Hulst.
Phase control of femtosecond pulses on the nanoscale using second harmonic nanoparticles.
Light Sci. Appl. **3**, e143 (2014).

[58] P. Tian, D. Keusters, Y. Suzaki, and W. S. Warren.
Femtosecond phase-coherent two-dimensional spectroscopy.
Science **300**, 1553–1555 (2003).

[59] J. A. Myers, K. L. Lewis, P. F. Tekavec, and J. P. Ogilvie.
Two-color two-dimensional Fourier transform electronic spectroscopy with a pulse-shaper.
Opt. Express **16**, 17420–17428 (2008).

[60] Y.-C. Cheng and G. R. Fleming.
Coherence quantum beats in two-dimensional electronic spectroscopy.
J. Phys. Chem. A **112**, 4254–4260 (2008).

[61] S.-H. Shim and M. T. Zanni.
How to turn your pumpprobe instrument into a multidimensional spectrometer: 2D IR and VIS spectroscopies via pulse shaping.
PCCP **11**, 748–761 (2009).

[62] H. Ohkita, S. Cook, Y. Astuti, W. Duffy, S. Tierney, W. Zhang, M. Heeney, I. McCulloch, J. Nelson, D. D. C. Bradley, and J. R. Durrant.
Charge carrier formation in polythiophene/fullerene blend films studied by transient absorption spectroscopy.
JACS **130**, 3030–3042 (2008).

[63] G. Grancini, D. Polli, D. Fazzi, J. Cabanillas-Gonzalez, G. Cerullo, and G. Lanzani.
Transient absorption imaging of P3HT:PCBM photovoltaic blend: evidence for interfacial charge transfer state.
J. Phys. Chem. Lett. **2**, 1099–1105 (2011).

[64] M. C. Fischer, J. W. Wilson, F. E. Robles, and W. S. Warren.
Invited review article: pump-probe microscopy.
Rev. Sci. Instrum. **87**, 031101 (2016).

[65] X. S. Xie.
Single-molecule spectroscopy and dynamics at room temperature.
Acc. Chem. Res. **29**, 598–606 (1996).

[66] R. M. Dickson, A. B. Cubitt, R. Y. Tsien, and W. E. Moerner.
On/off blinking and switching behaviour of single molecules of green fluorescent protein.
Nature **388**, 355 (1997).

[67] W. E. Moerner and M. Orrit.
Illuminating single molecules in condensed matter.
Science **283**, 1670–1676 (1999).

[68] P. Tamarat, A. Maali, B. Lounis, and M. Orrit.
Ten years of single-molecule spectroscopy.
J. Phys. Chem. A **104**, 1–16 (2000).

[69] E. M. H. P. van Dijk, J. Hernando, J.-J. Garca-López, M. Crego-Calama, D. N. Reinhoudt, L. Kuipers, M. F. Garca-Parajó, and N. F. van Hulst.
Single-molecule pump-probe detection resolves ultrafast pathways in individual and coupled quantum systems.
Phys. Rev. Lett. **94**, 078302 (2005).

[70] D. Brinks, F. D. Stefani, F. Kulzer, R. Hildner, T. H. Taminiau, Y. Avlasevich, K. Mullen, and N. F. van Hulst.
Visualizing and controlling vibrational wave packets of single molecules.
Nature **465**, 905–908 (2010).

[71] R. Hildner, D. Brinks, J. B. Nieder, R. J. Cogdell, and N. F. v. Hulst.
Quantum Coherent Energy Transfer over Varying Pathways in Single Light-Harvesting Complexes.
Science **340**, 1448–1451 (2013).

[72] D. Brinks, R. Hildner, E. M. H. P. v. Dijk, F. D. Stefani, J. B. Nieder, J. Hernando, and N. F. v. Hulst.
Ultrafast dynamics of single molecules.
Chem. Soc. Rev. **43**, 2476–2491 (2014).

[73] L. Piatkowski, N. Accanto, and N. F. van Hulst.
Ultrafast meets ultrasmall: controlling nanoantennas and molecules.
ACS Photonics **3**, 1401–1414 (2016).

[74] C. R. Baiz, D. Schach, and A. Tokmakoff.
Ultrafast 2D IR microscopy.
Opt. Express **22**, 18724–18735 (2014).

[75] A. L. Serrano, A. Ghosh, J. S. Ostrander, and M. T. Zanni.
Wide-field FTIR microscopy using mid-IR pulse shaping.
Opt. Express **23**, 17815–17827 (2015).

[76] J. S. Ostrander, A. L. Serrano, A. Ghosh, and M. T. Zanni.
Spatially resolved two-dimensional infrared spectroscopy via wide-field microscopy.
ACS Photonics **3**, 1315–1323 (2016).

[77] T. A. A. Oliver.
Recent advances in multidimensional ultrafast spectroscopy.
R. Soc. Open Sci. **5**, 171425 (2018).

[78] S. Voll.
Aufbau und Theorie eines Festkörper-Femtosekundenlasers.
Diploma thesis, Universität Würzburg (1997).

[79] S. Goetz.
Spektrale Interferometrie an plasmonischen Wellenleitern.
Master's thesis, Universität Würzburg (2012).

[80] C. Rewitz, T. Keitzl, P. Tuchscherer, S. Goetz, P. Geisler, G. Razinskas, B. Hecht, and T. Brixner.
Spectral-interference microscopy for characterization of functional plasmonic elements.
Opt. Express **20**, 14632–14647 (2012).

[81] M. Kempe, U. Stamm, B. Wilhelmi, and W. Rudolph.
Spatial and temporal transformation of femtosecond laser pulses by lenses and lens systems.
J. Opt. Soc. Am. B **9**, 1158–1165 (1992).

[82] L. Novotny and B. Hecht.
Principles of nano-optics.
First edition. Cambridge University Press, Cambridge (2006).

[83] M. W. Davidson.
MicroscopyU (2018).
http://www.microscopyu.com/microscopy-basics/numerical-aperture.

[84] S. W. Hell, E. H. K. Stelzer, S. Lindek, and C. Cremer.
Confocal microscopy with an increased detection aperture: type-B 4Pi confocal microscopy.
Opt. Lett. **19**, 222–224 (1994).

[85] W. H. Steel.
The design of reflecting microscope objectives.
Aust. J. Sci. Res. Ser. A **4**, 1 (1951).

[86] R. Kingslake and R. B. Johnson.
Lens design fundamentals - 2nd edition.
Second edition. Burlington, MA: Academic Press (2009).

[87] S. Kedenburg, M. Vieweg, T. Gissibl, and H. Giessen.
Linear refractive index and absorption measurements of nonlinear optical liquids in the visible and near-infrared spectral region.
Opt. Mater. Express **2**, 1588–1611 (2012).

[88] U. Fuchs, U. D. Zeitner, and A. Tünnermann.
Ultra-short pulse propagation in complex optical systems.
Opt. Express **13**, 3852–3861 (2005).

[89] F. C. Strong.
How the Fourier transform infrared spectrophotometer works.
J. Chem. Educ. **56**, 681 (1979).

[90] T.-W. Wu, J. Tang, B. Hajj, and M. Cui.
Phase resolved interferometric spectral modulation (PRISM) for ultrafast pulse measurement and compression.
Opt. Express **19**, 12961–12968 (2011).

[91] M. Planck.
Zur Theorie des Gesetzes der Energieverteilung im Normalspektrum.
Verh. Dtsch. Phys. Ges. **2**, 237 (1900).

[92] C. Rewitz.
Analytische und adaptive kohärente Kontrolle optischer Nahfelder durch Formung ultrakurzer Laserpulse.
Diploma thesis, Universität Würzburg (2009).

[93] C. Rewitz, T. Keitzl, P. Tuchscherer, J.-S. Huang, P. Geisler, G. Razinskas, B. Hecht, and T. Brixner.
Ultrafast plasmon propagation in nanowires characterized by far-field spectral interferometry.
Nano Lett. **12**, 45–49 (2012).

[94] L. Lepetit, G. Chériaux, and M. Joffre.
Linear techniques of phase measurement by femtosecond spectral interferometry for applications in spectroscopy.
J. Opt. Soc. Am. B **12**, 2467–2474 (1995).

[95] T. Keitzl.
Plasmonenpropagation an Nanostrukturen.
Diploma thesis, Universität Würzburg (2011).

[96] M. H. Brenner, D. Cai, J. A. Swanson, and J. P. Ogilvie.
Two-photon imaging of multiple fluorescent proteins by phase-shaping and linear unmixing with a single broadband laser.
Opt. Express **21**, 17256–17264 (2013).

[97] M. I. Stockman.
Ultrafast nanoplasmonics under coherent control.
New J. Phys. **10**, 025031 (2008).

[98] M. Aeschlimann, T. Brixner, A. Fischer, C. Kramer, P. Melchior, W. Pfeiffer, C. Schneider, C. Strüber, P. Tuchscherer, and D. V. Voronine.
Coherent two-dimensional nanoscopy.
Science **333**, 1723–1726 (2011).

[99] M. Aeschlimann, M. Bauer, D. Bayer, T. Brixner, S. Cunovic, A. Fischer, P. Melchior, W. Pfeiffer, M. Rohmer, C. Schneider, C. Strüber, P. Tuchscherer, and D. V. Voronine.
Optimal open-loop near-field control of plasmonic nanostructures.
New J. Phys. **14**, 033030 (2012).

[100] P. Biagioni, D. Brida, J.-S. Huang, J. Kern, L. Du, B. Hecht, M. Finazzi, and G. Cerullo.
Dynamics of four-photon photoluminescence in gold nanoantennas.
Nano Lett. **12**, 2941–2947 (2012).

[101] M. Wollenhaupt, A. Assion, and T. Baumert.
Femtosecond laser pulses: linear properties, manipulation, generation and measurement.
In *Springer handbook of lasers and optics*, pp. 937–983. Springer Science+Business Media, New York (2007).

[102] A. Monmayrant, S. Weber, and B. Chatel.
A newcomer's guide to ultrashort pulse shaping and characterization.
J. Phys. B: At. Mol. Opt. Phys. **43**, 103001 (2010).

[103] L. Polachek, D. Oron, and Y. Silberberg.
Full control of the spectral polarization of ultrashort pulses.
Opt. Lett. **31**, 631–633 (2006).

[104] M. Plewicki, S. Weber, F. Weise, and A. Lindinger.
Independent control over the amplitude, phase, and polarization of femtosecond pulses.
Appl. Phys. B **86**, 259–263 (2006).

[105] F. Weise and A. Lindinger.
Full control over the electric field using four liquid crystal arrays.
Opt. Lett. **34**, 1258–1260 (2009).

[106] Y. Esumi, M. D. Kabir, and F. Kannari.
Spatiotemporal vector pulse shaping of femtosecond laser pulses with a multi-pass two-dimensional spatial light modulator.
Opt. Express **17**, 19153–19159 (2009).

[107] C. Schwarz, O. Hüter, and T. Brixner.
Full vector-field control of ultrashort laser pulses utilizing a single dual-layer spatial light modulator in a common-path setup.
J. Opt. Soc. Am. B **32**, 933–945 (2015).

[108] S. Roeding.
Coherent multidimensional spectroscopy in molecular beams and liquids using incoherent observables.
Dissertation, Universität Würzburg (2017).

[109] Fastlite.
Dazzler system operating manual.
Technical report, Fastlite (2005).

[110] N. M. Kearns, R. D. Mehlenbacher, A. C. Jones, and M. T. Zanni.
Broadband 2D electronic spectrometer using white light and pulse shaping: noise and signal evaluation at 1 and 100 kHz.
Opt. Express **25**, 7869–7883 (2017).

[111] C. Froehly, B. Colombeau, and M. Vampouille.
Shaping and analysis of picosecond light pulses.
Progress in optics **20**, 63–153 (1983).

[112] A. M. Weiner, D. E. Leaird, J. S. Patel, and J. R. Wullert.
Programmable femtosecond pulse shaping by use of a multielement liquid-crystal phase modulator.
Opt. Lett. **15**, 326–328 (1990).

[113] M. M. Wefers and K. A. Nelson.
Generation of high-fidelity programmable ultrafast optical waveforms.
Opt. Lett. **20**, 1047–1049 (1995).

[114] T. Binhammer, E. Rittweger, R. Ell, F. Kartner, and U. Morgner.
Prism-based pulse shaper for octave spanning spectra.
IEEE J. Quantum Electron. **41**, 1552 – 1557 (2005).

[115] B. Xu, Y. Coello, V. V. Lozovoy, D. A. Harris, and M. Dantus.
Pulse shaping of octave spanning femtosecond laser pulses.
Opt. Express **14**, 10939–10944 (2006).

[116] T. Brixner.
Kohärente Kontrolle von Photodissoziationsreaktionen mit optimal geformten ultrakurzen Laserpulsen.
Diploma thesis, Universität Würzburg (1998).

[117] E. A. Gibson, D. M. Gaudiosi, H. C. Kapteyn, R. Jimenez, S. Kane, R. Huff, C. Durfee, and J. Squier.
Efficient reflection grisms for pulse compression and dispersion compensation of femtosecond pulses.
Opt. Lett. **31**, 3363–3365 (2006).

[118] J. K. Ranka, A. L. Gaeta, A. Baltuska, M. S. Pshenichnikov, and D. A. Wiersma.
Autocorrelation measurement of 6-fs pulses based on the two-photon-induced photocurrent in a GaAsP photodiode.
Opt. Lett. **22**, 1344–1346 (1997).

[119] S. Lochbrunner, P. Huppmann, and E. Riedle.
Crosscorrelation measurements of ultrashort visible pulses: comparison between nonlinear crystals and SiC photodiodes.
Opt. Commun. **184**, 321–328 (2000).

[120] I. Amat-Roldán, I. Cormack, P. Loza-Alvarez, E. Gualda, and D. Artigas.
Ultrashort pulse characterisation with SHG collinear-FROG.
Opt. Express **12**, 1169–1178 (2004).

[121] G. Stibenz and G. Steinmeyer.
Interferometric frequency-resolved optical gating.
Opt. Express **13**, 2617–2626 (2005).

[122] A. Galler and T. Feurer.
Pulse shaper assisted short laser pulse characterization.
Appl. Phys. B **90**, 427–430 (2008).

[123] C. Iaconis and I. Walmsley.
Spectral phase interferometry for direct electric-field reconstruction of ultrashort optical pulses.
Opt. Lett. **23**, 792–794 (1998).

[124] L. Gallmann, D. H. Sutter, N. Matuschek, G. Steinmeyer, U. Keller, C. Iaconis, and I. A. Walmsley.
Characterization of sub-6-fs optical pulses with spectral phase interferometry for direct electric-field reconstruction.
Opt. Lett. **24**, 1314–1316 (1999).

[125] C. Iaconis and I. Walmsley.
Self-referencing spectral interferometry for measuring ultrashort optical pulses.
IEEE J. Quantum Electron. **35**, 501–509 (1999).

[126] L. Gallmann, G. Steinmeyer, D. H. Sutter, T. Rupp, C. Iaconis, I. A. Walmsley, and U. Keller.
Spatially resolved amplitude and phase characterization of femtosecond optical pulses.
Opt. Lett. **26**, 96–98 (2001).

[127] D. Yelin, D. Meshulach, and Y. Silberberg.
Adaptive femtosecond pulse compression.
Opt. Lett. **22**, 1793–1795 (1997).

[128] T. Baumert, T. Brixner, V. Seyfried, M. Strehle, and G. Gerber.
Femtosecond pulse shaping by an evolutionary algorithm with feedback.
Appl. Phys. B **65**, 779–782 (1997).

[129] T. Brixner, M. Strehle, and G. Gerber.
Feedback-controlled optimization of amplified femtosecond laser pulses.
Appl. Phys. B **68**, 281–284 (1999).

[130] Y. Coello, V. V. Lozovoy, T. C. Gunaratne, B. Xu, I. Borukhovich, C.-H. Tseng, T. Weinacht, and M. Dantus.
Interference without an interferometer: a different approach to measuring, compressing, and shaping ultrashort laser pulses.
J. Opt. Soc. Am. B **25**, A140–A150 (2008).

[131] A. Comin, R. Ciesielski, N. Coca-López, and A. Hartschuh.
Phase retrieval of ultrashort laser pulses using a MIIPS algorithm.
Opt. Express **24**, 2505–2512 (2016).

[132] J. Extermann, L. Bonacina, F. Courvoisier, D. Kiselev, Y. Mugnier, R. Le Dantec, C. Galez, and J.-P. Wolf.
Nano-FROG: frequency resolved optical gating by a nanometric object.
Opt. Express **16**, 10405–10411 (2008).

[133] P. Wnuk, L. L. Xuan, A. Slablab, C. Tard, S. Perruchas, T. Gacoin, J.-F. Roch, D. Chauvat, and C. Radzewicz.
Coherent nonlinear emission from a single KTP nanoparticle with broadband femtosecond pulses.
Opt. Express **17**, 4652–4658 (2009).

[134] M. Wurdack.
Simulation von PRISM, einer phasenaufgelösten interferometrischen spektralen Modulation zur Kompression ultrakurzer Pulse.
Bachelor thesis, Universität Würzburg (2013).

[135] M. Wurdack.
Durchführung von PRISM, einer phasenaufgelösten interferometrischen spektralen Modulation zur Kompression ultrakurzer Pulse.
Bachelor thesis, Universität Würzburg (2014).

[136] C. Radzewicz, M. la Grone, and J. Krasinski.
Interferometric measurement of femtosecond pulse distortion by lenses.
Opt. Commun. **126**, 185–190 (1996).

[137] R. Netz, T. Feurer, R. Wolleschensky, and R. Sauerbrey.
Measurement of the pulse-front distortion in high-numerical-aperture optics.
Appl. Phys. B **70**, 833–837 (2000).

[138] P. Bowlan, P. Gabolde, and R. Trebino.
Directly measuring the spatio-temporal electric field of focusing ultrashort pulses.
Opt. Express **15**, 10219–10230 (2007).

[139] P. Bowlan, P. Gabolde, M. A. Coughlan, R. Trebino, and R. J. Levis.
Measuring the spatiotemporal electric field of ultrashort pulses with high spatial and spectral resolution.
J. Opt. Soc. Am. B **25**, A81–A92 (2008).

[140] D. Brinks, R. Hildner, F. D. Stefani, and N. F. van Hulst.
Beating spatio-temporal coupling: implications for pulse shaping and coherent control experiments.
Opt. Express **19**, 26486–26499 (2011).

[141] B. J. Sussman, R. Lausten, and A. Stolow.
Focusing of light following a 4-f pulse shaper: considerations for quantum control.
Phys. Rev. A **77**, 043416 (2008).

[142] M. Wefers and K. Nelson.
Space-time profiles of shaped ultrafast optical waveforms.
IEEE J. Quantum Electron. **32**, 161–172 (1996).

[143] F. Frei, R. Bloch, and T. Feurer.
Influence of finite spatial resolution on single- and double-pass femtosecond pulse shapers.
Opt. Lett. **35**, 4072–4074 (2010).

[144] F. Frei, A. Galler, and T. Feurer.
Space-time coupling in femtosecond pulse shaping and its effects on coherent control.
J. Chem. Phys. **130**, 034302 (2009).

[145] N. Krebs, R. A. Probst, and E. Riedle.
Sub-20 fs pulses shaped directly in the UV by an acousto-optic programmable dispersive filter.
Opt. Express **18**, 6164–6171 (2010).

[146] E. Candès, J. Romberg, and T. Tao.
Robust uncertainty principles: exact signal reconstruction from highly incomplete frequency information.
IEEE Trans. Inf. Theory **52**, 489–509 (2006).

[147] S. Roeding, N. Klimovich, and T. Brixner.
Optimizing sparse sampling for 2D electronic spectroscopy.
The Journal of Chemical Physics **146**, 084201 (2017).

[148] Jenoptik.
SLM-S640d / SLM-S320d technical documentation (2012).

[149] C. Dorrer and F. Salin.
Phase amplitude coupling in spectral phase modulation.
IEEE J. Sel. Top. Quantum Electron. **4**, 342–345 (1998).

[150] J. Vaughan, T. Feurer, K. Stone, and K. Nelson.
Analysis of replica pulses in femtosecond pulse shaping with pixelated devices.
Opt. Express **14**, 1314–1328 (2006).

[151] M. A. Coughlan, M. Plewicki, and R. J. Levis.
Spatio-temporal and -spectral coupling of shaped laser pulses in a focusing geometry.
Opt. Express **18**, 23973–23986 (2010).

[152] S. A. Maier.
Plasmonics: fundamentals and applications.
First edition. Springer, Berlin (2007).

[153] W. L. Barnes, A. Dereux, and T. W. Ebbesen.
Surface plasmon subwavelength optics.
Nature **424**, 824–830 (2003).

[154] M. I. Stockman.
Nanoplasmonics: past, present, and glimpse into future.
Opt. Express **19**, 22029–22106 (2011).

[155] L. Novotny and N. van Hulst.
Antennas for light.
Nat. Photonics **5**, 83–90 (2011).

[156] P. Biagioni, J.-S. Huang, and B. Hecht.
Nanoantennas for visible and infrared radiation.
Rep. Prog. Phys. **75**, 024402 (2012).

[157] Y. Fang, Z. Li, Y. Huang, S. Zhang, P. Nordlander, N. J. Halas, and H. Xu.
Branched silver nanowires as controllable plasmon routers.
Nano Lett. **10**, 1950–1954 (2010).

[158] H. Wei, Z. Wang, X. Tian, M. Kall, and H. Xu.
Cascaded logic gates in nanophotonic plasmon networks.
Nat. Commun. **2**, 387 (2011).

[159] G. Lenz, J. Zimmermann, T. Katsufuji, M. E. Lines, H. Y. Hwang, S. Spälter, R. E. Slusher, S.-W. Cheong, J. Sanghera, and I. D. Aggarwal.
Large Kerr effect in bulk Se-based chalcogenide glasses.
Opt. Lett. **25**, 254–256 (2000).

[160] A. A. Reiserer, J.-S. Huang, B. Hecht, and T. Brixner.
Subwavelength broadband splitters and switches for femtosecond plasmonic signals.
Opt. Express **18**, 11810–11820 (2010).

[161] P. Ginzburg, A. Hayat, N. Berkovitch, and M. Orenstein.
Nonlocal ponderomotive nonlinearity in plasmonics.
Opt. Lett. **35**, 1551–1553 (2010).

[162] S. Palomba and L. Novotny.
Nonlinear excitation of surface plasmon polaritons by four-wave mixing.
Phys. Rev. Lett. **101**, 056802 (2008).

[163] J. Renger, R. Quidant, N. van Hulst, and L. Novotny.
Surface-enhanced nonlinear four-wave mixing.
Phys. Rev. Lett. **104**, 046803 (2010).

[164] M. Lippitz, M. A. van Dijk, and M. Orrit.
Third-harmonic generation from single gold nanoparticles.
Nano Lett. **5**, 799–802 (2005).

[165] T. Hanke, G. Krauss, D. Träutlein, B. Wild, R. Bratschitsch, and A. Leitenstorfer.
Efficient nonlinear light emission of single gold optical antennas driven by few-cycle near-infrared pulses.
Phys. Rev. Lett. **103**, 257404 (2009).

[166] M. Hentschel, T. Utikal, H. Giessen, and M. Lippitz.
Quantitative modeling of the third harmonic emission spectrum of plasmonic nanoantennas.
Nano Lett. **12**, 3778–3782 (2012).

[167] R. W. Boyd, Z. Shi, and I. De Leon.
The third-order nonlinear optical susceptibility of gold.
Opt. Commun. **326**, 74–79 (2014).

[168] D. D. Smith, Y. Yoon, R. W. Boyd, J. K. Campbell, L. A. Baker, R. M. Crooks, and M. George.
Z-scan measurement of the nonlinear absorption of a thin gold film.
J. Appl. Phys. **86**, 6200 (1999).

[169] P. Wang, Y. Lu, L. Tang, J. Zhang, H. Ming, J. Xie, F.-H. Ho, H.-H. Chang, H.-Y. Lin, and D.-P. Tsai.
Surface-enhanced optical nonlinearity of a gold film.
Opt. Commun. **229**, 425–429 (2004).

[170] N. Rotenberg, A. D. Bristow, M. Pfeiffer, M. Betz, and H. M. van Driel.
Nonlinear absorption in Au films: role of thermal effects.
Phys. Rev. B **75**, 155426 (2007).

[171] E. Xenogiannopoulou, P. Aloukos, S. Couris, E. Kaminska, A. Piotrowska, and E. Dynowska.
Third-order nonlinear optical properties of thin sputtered gold films.
Opt. Commun. **275**, 217–222 (2007).

[172] M. Sheik-Bahae, A. A. Said, and E. W. V. Stryland.
High-sensitivity, single-beam N_2 measurements.
Opt. Lett. **14**, 955–957 (1989).

[173] M. Sheik-Bahae, A. Said, T.-H. Wei, D. Hagan, and E. W. Van Stryland.
Sensitive measurement of optical nonlinearities using a single beam.
IEEE J. Quantum Electron. **26**, 760–769 (1990).

[174] R. L. Sutherland.
Handbook of nonlinear optics.
Second edition. CRC Press, Ohio (2003).

[175] P. B. Chappie, J. Staromlynska, and R. G. McDuff.
Z-scan studies in the thin- and the thick-sample limits.
J. Opt. Soc. Am. B **11**, 975–982 (1994).

[176] R. Trebino, K. W. DeLong, D. N. Fittinghoff, J. N. Sweetser, M. A. Krumbügel, and B. A. Richman.
Measuring ultrashort laser pulses in the time-frequency domain using frequency-resolved optical gating.
Rev. Sci. Instrum. **68**, 3277–3295 (1997).

[177] D. Milam.
Review and assessment of measured values of the nonlinear refractive-index coefficient of fused silica.
Appl. Opt. **37**, 546–550 (1998).

[178] H. I. Elim, W. Ji, and F. Zhu.
Carrier concentration dependence of optical Kerr nonlinearity in indium tin oxide films.
Appl. Phys. B **82**, 439–442 (2006).

[179] R. DeSalvo, A. A. Said, D. J. Hagan, E. W. V. Stryland, and M. Sheik-Bahae.
Infrared to ultraviolet measurements of two-photon absorption and N_2 in wide bandgap solids.
IEEE Journal of Quantum Electronics **32**, 1324–1333 (1996).

[180] T. Olivier, F. Billard, and H. Akhouayri.
Nanosecond z-scan measurements of the nonlinear refractive index of fused silica.
Opt. Express **12**, 1377–1382 (2004).

[181] J.-S. Huang, V. Callegari, P. Geisler, C. Brüning, J. Kern, J. C. Prangsma, X. Wu, T. Feichtner, J. Ziegler, P. Weinmann, M. Kamp, A. Forchel, P. Biagioni, U. Sennhauser, and B. Hecht.
Atomically flat single-crystalline gold nanostructures for plasmonic nanocircuitry.
Nat. Commun. **1**, 150 (2010).

[182] X. Wu, R. Kullock, E. Krauss, and B. Hecht.
Single-crystalline gold microplates grown on substrates by solution-phase synthesis.
Cryst. Res. Technol. **50**, 595–602 (2015).

[183] C. Kern, M. Zürch, J. Petschulat, T. Pertsch, B. Kley, T. Käsebier, U. Hübner, and C. Spielmann.
Comparison of femtosecond laser-induced damage on unstructured vs. nano-structured Au-targets.
Appl. Phys. A **104**, 15 (2011).

[184] P. B. Johnson and R. W. Christy.
Optical constants of the noble metals.
Phys. Rev. B **6**, 4370–4379 (1972).

[185] R. d. Nalda, R. d. Coso, J. Requejo-Isidro, J. Olivares, A. Suarez-Garcia, J. Solis, and C. N. Afonso.
Limits to the determination of the nonlinear refractive index by the z-scan method.
J. Opt. Soc. Am. B, JOSAB **19**, 289–296 (2002).

[186] P. Mühlschlegel, H.-J. Eisler, O. J. F. Martin, B. Hecht, and D. W. Pohl.
Resonant optical antennas.
Science **308**, 1607–1609 (2005).

[187] J.-S. Huang, T. Feichtner, P. Biagioni, and B. Hecht.
Impedance matching and emission properties of nanoantennas in an optical nanocircuit.
Nano Lett. **9**, 1897–1902 (2009).

[188] M. Schnell, P. Alonso-Gonzalez, L. Arzubiaga, F. Casanova, L. E. Hueso, A. Chuvilin, and R. Hillenbrand.
Nanofocusing of mid-infrared energy with tapered transmission lines.
Nat. Photonics **5**, 283–287 (2011).

[189] P. M. Krenz, R. L. Olmon, B. A. Lail, M. B. Raschke, and G. D. Boreman.
Near-field measurement of infrared coplanar strip transmission line attenuation and propagation constants.
Opt. Express **18**, 21678–21686 (2010).

[190] E. Verhagen, M. Spasenovicacute, A. Polman, and L. K. Kuipers.
Nanowire plasmon excitation by adiabatic mode transformation.
Phys. Rev. Lett. **102**, 203904 (2009).

[191] M. Cinchetti, A. Gloskovskii, S. A. Nepjiko, G. Schönhense, H. Rochholz, and M. Kreiter.
Photoemission electron microscopy as a tool for the investigation of optical near fields.
Phys. Rev. Lett. **95**, 047601 (2005).

[192] T. Brixner, J. Stenger, H. M. Vaswani, M. Cho, R. E. Blankenship, and G. R. Fleming.
Two-dimensional spectroscopy of electronic couplings in photosynthesis.
Nature **434**, 625–628 (2005).

[193] G. S. Engel, T. R. Calhoun, E. L. Read, T.-K. Ahn, T. Manal, Y.-C. Cheng, R. E. Blankenship, and G. R. Fleming.
Evidence for wavelike energy transfer through quantum coherence in photosynthetic systems.
Nature **446**, 782–786 (2007).

[194] G. Nardin, T. M. Autry, G. Moody, R. Singh, H. Li, and S. T. Cundiff.
Multi-dimensional coherent optical spectroscopy of semiconductor nanostructures: collinear and non-collinear approaches.
J. Appl. Phys. **117**, 112804 (2015).

[195] V. M. Huxter, T. A. A. Oliver, D. Budker, and G. R. Fleming.
Vibrational and electronic dynamics of nitrogen-vacancy centres in diamond revealed by two-dimensional ultrafast spectroscopy.
Nat. Phys. **9**, 744–749 (2013).

[196] T. A. Oudenhoven, Y. Joo, J. E. Laaser, P. Gopalan, and M. T. Zanni.
Dye aggregation identified by vibrational coupling using 2D IR spectroscopy.
J. Chem. Phys. **142**, 212449 (2015).

[197] A. D. Sio, F. Troiani, M. Maiuri, J. Réhault, E. Sommer, J. Lim, S. F. Huelga, M. B. Plenio, C. A. Rozzi, G. Cerullo, E. Molinari, and C. Lienau.
Tracking the coherent generation of polaron pairs in conjugated polymers.
Nat. Commun. **7**, 13742 (2016).

[198] J. S. Ostrander, R. Knepper, A. S. Tappan, J. J. Kay, M. T. Zanni, and D. A. Farrow.
Energy transfer between coherently delocalized states in thin films of the explosive pentaerythritol tetranitrate (PETN) revealed by two-dimensional infrared spectroscopy.
J. Phys. Chem. B **121**, 1352–1361 (2017).

[199] K. W. Stone, K. Gundogdu, D. B. Turner, X. Li, S. T. Cundiff, and K. A. Nelson.
Two-quantum 2D FT electronic spectroscopy of biexcitons in GaAs quantum wells.
Science **324**, 1169–1173 (2009).

[200] G. Moody, M. E. Siemens, A. D. Bristow, X. Dai, D. Karaiskaj, A. S. Bracker, D. Gammon, and S. T. Cundiff.
Exciton-exciton and exciton-phonon interactions in an interfacial GaAs quantum dot ensemble.
Phys. Rev. B **83**, 115324 (2011).

[201] J. Bylsma, P. Dey, J. Paul, S. Hoogland, E. H. Sargent, J. M. Luther, M. C. Beard, and D. Karaiskaj.
Quantum beats due to excitonic ground-state splitting in colloidal quantum dots.
Phys. Rev. B **86**, 125322 (2012).

[202] G. Moody, R. Singh, H. Li, I. A. Akimov, M. Bayer, D. Reuter, A. D. Wieck, and S. T. Cundiff.
Fifth-order nonlinear optical response of excitonic states in an InAs quantum dot ensemble measured with two-dimensional spectroscopy.
Phys. Rev. B **87**, 045313 (2013).

[203] C. Y. Wong and G. D. Scholes.
Biexcitonic fine structure of CdSe nanocrystals probed by polarization-dependent two-dimensional photon echo spectroscopy.
J. Phys. Chem. A **115**, 3797–3806 (2011).

[204] R. D. Mehlenbacher, T. J. McDonough, M. Grechko, M.-Y. Wu, M. S. Arnold, and M. T. Zanni.
Energy transfer pathways in semiconducting carbon nanotubes revealed using two-dimensional white-light spectroscopy.
Nat. Commun. **6**, 6732 (2015).

[205] W. Wagner, C. Li, J. Semmlow, and W. Warren.
Rapid phase-cycled two-dimensional optical spectroscopy in fluorescence and transmission mode.
Opt. Express **13**, 3697–3706 (2005).

[206] P. F. Tekavec, G. A. Lott, and A. H. Marcus.
Fluorescence-detected two-dimensional electronic coherence spectroscopy by acousto-optic phase modulation.
J. Chem. Phys. **127**, 214307 (2007).

[207] A. K. De, D. Monahan, J. M. Dawlaty, and G. R. Fleming.
Two-dimensional fluorescence-detected coherent spectroscopy with absolute phasing by confocal imaging of a dynamic grating and 27-step phase-cycling.
J. Chem. Phys. **140**, 194201 (2014).

[208] S. Draeger, S. Roeding, and T. Brixner.
Rapid-scan coherent 2D fluorescence spectroscopy.
Opt. Express **25**, 3259–3267 (2017).

[209] S. Roeding and T. Brixner.
Multidimensional electronic spectroscopy in molecular beams with mass-resolved ion detection.
In *International Conference on Ultrafast Phenomena XX*, p. UM3A.2. Optical Society of America (2016).

[210] K. J. Karki, J. R. Widom, J. Seibt, I. Moody, M. C. Lonergan, T. Pullerits, and A. H. Marcus.
Coherent two-dimensional photocurrent spectroscopy in a PbS quantum dot photocell.
Nat. Commun. **5**, 5869 (2014).

[211] M. Aeschlimann, T. Brixner, D. Differt, U. Heinzmann, M. Hensen, C. Kramer, F. Lükermann, P. Melchior, W. Pfeiffer, M. Piecuch, C. Schneider, H. Stiebig, C. Strüber, and P. Thielen.
Perfect absorption in nanotextured thin films via Anderson-localized photon modes.
Nat. Photonics **9**, 663–668 (2015).

[212] E. Vella, H. Li, P. Grégoire, S. M. Tuladhar, M. S. Vezie, S. Few, C. M. Bazán, J. Nelson, C. Silva-Acuña, and E. R. Bittner.
Ultrafast decoherence dynamics govern photocarrier generation efficiencies in polymer solar cells.
Sci. Rep. **6**, 29437 (2016).

[213] J. Cabanillas-Gonzalez, G. Grancini, and G. Lanzani.
Pump-probe spectroscopy in organic semiconductors: monitoring fundamental processes of relevance in optoelectronics.
Adv. Mater. **23**, 5468–5485 (2011).

[214] M. M. Gabriel, E. M. Grumstrup, J. R. Kirschbrown, C. W. Pinion, J. D. Christesen, D. F. Zigler, E. E. M. Cating, J. F. Cahoon, and J. M. Papanikolas.
Imaging charge separation and carrier recombination in nanowire p-i-n junctions using ultrafast microscopy.
Nano Lett. **14**, 3079–3087 (2014).

[215] C. Y. Wong, B. L. Cotts, H. Wu, and N. S. Ginsberg.
Exciton dynamics reveal aggregates with intermolecular order at hidden interfaces in solution-cast organic semiconducting films.
Nat. Commun. **6**, 6946 (2015).

[216] Z. Guo, Y. Wan, M. Yang, J. Snaider, K. Zhu, and L. Huang.
Long-range hot-carrier transport in hybrid perovskites visualized by ultrafast microscopy.
Science **356**, 59–62 (2017).

[217] R. Hildner, D. Brinks, and N. F. v. Hulst.
Femtosecond coherence and quantum control of single molecules at room temperature.
Nat. Phys. **7**, 172–177 (2011).

[218] E. Wientjes, J. Renger, A. G. Curto, R. Cogdell, and N. F. v. Hulst.
Strong antenna-enhanced fluorescence of a single light-harvesting complex shows photon antibunching.
Nat. Commun. **5**, 4236 (2014).

[219] W. Langbein and B. Patton.
Transient coherent nonlinear spectroscopy of single quantum dots.
J. Phys.: Condens. Matter **19**, 295203 (2007).

[220] J. Kasprzak, B. Patton, V. Savona, and W. Langbein.
Coherent coupling between distant excitons revealed by two-dimensional nonlinear hyperspectral imaging.
Nat. Photon. **5**, 57–63 (2011).

[221] R. Ciesielski, A. Comin, M. Handloser, K. Donkers, G. Piredda, A. Lombardo, A. C. Ferrari, and A. Hartschuh.
Graphene near-degenerate four-wave mixing for phase characterization of broadband pulses in ultrafast microscopy.
Nano Lett. **15**, 4968–4972 (2015).

[222] F. D. Fuller and J. P. Ogilvie.
Experimental implementations of two-dimensional Fourier transform electronic spectroscopy.
Annu. Rev. Phys. Chem. **66**, 667–690 (2015).

[223] G. Moody and S. T. Cundiff.
Advances in multi-dimensional coherent spectroscopy of semiconductor nanostructures.
Adv. Phys. X **2**, 641–674 (2017).

[224] H.-S. Tan.
Theory and phase-cycling scheme selection principles of collinear phase coherent multi-dimensional optical spectroscopy.
J. Chem. Phys. **129**, 124501 (2008).

[225] M. Brendel, S. Krause, A. Steindamm, A. K. Topczak, S. Sundarraj, P. Erk, S. Höhla, N. Fruehauf, N. Koch, and J. Pflaum.
The effect of gradual fluorination on the properties of F_nZnPc thin films and F_nZnPc/C60 bilayer photovoltaic cells.
Adv. Funct. Mater. **25**, 1565–1573 (2015).

[226] V. Kolb and J. Pflaum.
Hybrid metal-organic nanocavity arrays for efficient light out-coupling.
Opt. Express **25**, 6678–6689 (2017).

Acknowledgements

A project like the creation of this thesis does largely depend on the guidance and support from a variety people involved professionally, administratively and socially. I am more than grateful for those who helped me throughout this time. In particular, I want to thank the following people:

- my supervisor **Prof. Dr. Tobias Brixner** for the confidence in my capabilities, giving me the possibility to work on several interesting topics in a well-equipped laboratory. I want to thank him for providing financial and advisory support, and for sharing his systematic approach to scientific projects. Furthermore, I would like to thank him for giving me the possibility to visit national and international summer schools and conferences.

- my predecessor **Dr. Christian Rewitz** for passing a carefully thought-trough experimental setup on to me, together with many hints and concepts to keep it running and extending it.

- the fellow scientists working with me in Lab 3: **Christian Dreher, Dr. Christian Rewitz, Dr. Donghai Li, Matthias Wurdack, Dr. Monika Pawłowska,** and **a rolling pin** for motivation and many fruitful discussions, as well as productive and amusing days in the lab.

- **Dr. Donghai Li** and **Matthias Nuss** for taking over the work in Lab 3, maintaining the experimental setup and extending based on their new creative ideas. Make pulse shapers great again!

- **Prof. Dr. Bert Hecht, Enno Krauss, Gary Razinskas, Prof. Dr. Jens Pflaum, Teresa Schmeiler** and **Verena Kolb** for their valuable input and teamwork in various collaborations. Thanks for supping me with carefully prepared samples and simulations.

- the members of the mechanics (**Wolfgang Liebler, Ralf Kohrmann, Katharina Schreckling**, and **Peter Lang**) and electronic workshop (**Jürgen Zimmermann** and **Reiner Eck**) for giving me insights into their expertise and providing me with individual solutions for the challenges I faced and created in the laboratory.

- our technical staff **Belinda Böhm** and **Sabine Fuchs** for maintaining our laboratory equipment and laser systems.

- our secretaries **Andrea Gehring, Anna Rosenfeldt, Sandra Stoudek**, and **Susanne Pfarr** for managing administrative tasks, always with a smile on their faces.

- **Dr. Roland Colditz** and **Dr. Hans-Christian Schmitt** for organizing the practical courses in physical chemistry.

- the actors **Lea Ress, Stefan Müller** and **Prof. Dr. Tobias Brixner** for the collective production of the ambitious short film "Femto Stars".

- the IPTC running enthusiasts, **Dr. Andreas Steinbacher, Dr. Federico Koch, Hans-Peter Solowan, Dr. Johannes Knorr, Dr. Sebastian Röding**, and **Dr. Stefan Rützel** for regular training session in the morning and motivating competitions.

- **Dr. Donghai Li, Lea Ress, Dr. Matthias Hensen, Sebastian Pres, Dr. Sebastian Röding** for proof-reading and discussing parts of this thesis.

- all current and past members of the **Lehrstuhl für Physikalische und Theoretische Chemie I (PC1)**, namely **Dr. Andreas Steinbacher, Bernhard Huber, Christian Dreher, Dr. Christian Kramer, Dr. Christian Rewitz, Dr. Christoph Schwarz, Dr. Cristina Consani, Daniel Fersch, Dr. Donghai Li, Fabian Ebert, Dr. Federico Koch, Dr. Florian Kanal, Dr. Francesc Molins Hans-Peter Solowan, Heiko Hildenbrand, Dr. Jakub Dostál Dr. Johannes Buback, Dr. Johannes Knorr, Julia Heitmüller, Lea Ress, Lysanne Dietrich, Marco Schmid, Dr. Martin Kullmann, Dr. Matthias Hensen, Matthias Nuss, Meike Diekmann, Michel Keller, Dr. Monika Pawłowska, Prof. Dr. Patrick Nürnberger, Dr. Philip Tuchscherer, Dr. Philipp Rudolf, Dr. Pramod Kumar Verma, Sebastian Pres, Dr. Sebastian Röding, Dr. Sebastian Schott, Simon Draeger, Stefan Müller, Dr. Stefan Rützel, Dr. Tatjana Quast, Dr. Tom Bolze, Tristan Ford, Dr. Ulrike Selig-Parthey**, and **Dr. Xiaonan Ma**. for formal and informal discussions. I especially enjoyed the coffee and banana breaks, breakfast and barbecue sessions and informal after-work meetings. Without the friendly atmosphere and many colleges willingly helping out past their own projects from my first day in the group, I would not even have considered starting this thesis.

- **Tamara Ehmann** and **Isabell Post** for cheerful lunch breaks.

- **Bernd Ernstberger** for relaxed evening discussions and casual gaming.

- my family **Sieglinde Götz**, **Bodo Götz**, **Amelie Schuseil** and **Sophie Heser** for their general support, always having an open ear and reminding me to focus on the things that matter.

- my partner **Sophie Hische** for her affection, her daily support and for showing me that all work is only worth the effort if you have someone to share it with.